PROBABILISTIC SEISMIC SLOPE STABILITY DESIGN

by

Jesse Burgess

Submitted in partial fulfillment of the requirements
for the degree of Master of Science

at

Dalhousie University
Halifax, Nova Scotia
April 2016

TABLE OF CONTENTS

LIST OF TABLES

LIST OF FIGURES

ABSTRACT

Deterministic slope stability design charts for cohesive-frictional ($c-\phi$) soils have been used by geotechnical engineers to examine the effects of earthquakes on slopes by identifying the critical seismic loading which brings the slope to a state of limit equilibrium. However, seismic slope stability design charts have yet to be extended to probabilistic analysis. In this study, the seismic stability of slopes, modeled using a two-dimensional spatially random $c-\phi$ soil, is studied using finite element analysis. Probabilistic analyses of seismically loaded slopes are performed by Monte Carlo simulations using the Random Finite Element Method (RFEM). A series of new slope stability design charts are provided that consider the influence of the spatial variability of soil for seismically loaded slopes with $\mu_\phi = 20°$. The charts may be used in the safe design of slopes subject to seismic loading, providing estimates of the probability of slope failure without requiring computer simulations.

LIST OF ABBREVIATIONS AND SYMBOLS USED

BPT	Becker penetration test for in-situ soil testing
CPT	Cone penetration test for in-situ soil testing
CRR	Cyclic resistance ratio
CSR	Cyclic stress ratio
GM	Ground motion
LAS	Local average subdivisions
LL	Liquid limit
PGA	Peak ground acceleration
PGV	Peak ground velocity
PI	Plasticity index
PSHA	Probabilistic seismiic hazard analysis
MRD	Mean rate density
MSF	Magnitude scaling factor
RFEM	Random finite element method
SPT	Standard penetration test for in-situ soil testing
SRV	Single random variable approach
a	area of a slice
a_i	regression coefficients in PSHA, i = 1, 2, 3, 4, 5, 6, 7, 8, 9, 10
a_{max}	maximum recorded horizontal acceleration
a_{yield}	yield acceleration

A_i	curve fitting parameters in V_S liquefaction analysis, i = 1, 2
b_i	fines content (f_c) dependent coefficients used in the clean-sands approximation for SPT analysis, i = 1, 2
B_i	regression coefficients for probabilistic liquefaction analysis, i = 1, 2
c	cohesion
c_F	factored cohesion
C_Q	normalizing factor used in CPT analysis
$CRR_{7.5}$	cyclic resistance ratio for an earthquake magnitude, M, of 7.5
$CSR_{7.5}$	cyclic stress ratio for an earthquake magnitude, M, of 7.5
CSR_{eq}	uncorrected cyclic stress ratio for an earthquake magnitude, M, of 7.5
d	sliding-block displacement in PSHA
D	depth factor
DH	depth to hard layer
E	Young's modulus
f_c	fines content
f_i	functions used in the evaluation of log-spiral failure surfaces, i=1,2,3,4
f_r	friction ratio
f_s	sleeve resistance in CPT field tests
F	static factor of safety
F_s	seismic factor of safety
F_L	factor of safety against liquefaction
F_L^*	set safety level for F_L in probabilistic analysis
g	gravity

GM	a placeholder for a ground motion variable in scalar PSHA
GM_1	a placeholder for a ground motion variable invector PSHA
GM_2	a placeholder for a ground motion variable in vector PSHA
H	height of the slope
I_c	soil behaviour type index
k	seismic coefficient
k_c	critical seismic coefficient
k_{lim}	theoretical limiting seismic coefficient
K_c	CPT clean sands correction factor
LL	liquid limit
M	earthquake magnitude
M_w	moment magnitude
MRD	mean rate density of the ground motion used in PSHA
MSF	earthquake magnitude scaling factor used in liquefaction analysis
n	size of a random field
n'	soil behaviour parameter in liquefaction analysis
N	static stability number
N_m	pseudo-static stability number
N_{BC}	blow count number
$(N_1)_{60}$	normalization of SPT blow count for an overburden stress of 100 kPa and a hammer efficiency of 60%
$(N_1)_{60,cs}$	clean sands normalization of SPT blow count for an overburden stress of 100 kPa and a hammer efficiency of 60%
p_f	probability of failure
P [.]	probability operator

P_a	atmospheric pressure
P_L	probability of liquefaction
PGA	peak ground acceleration
PGV	peak ground velocity
PI	plasticity index
q_c	field test result for cone penetration tip resistance
(q_{c1N})	dimensionless normalized penetration tip resistance
$(q_{c1N})_{cs}$	dimensionless normalized clean sands cone penetration tip resistance
Q	normalized cone tip resistance
r	radius of a log-spiral surface
r_0	inital radius of a log-spiral surface
r_0'	radial factor
r_d	stress reduction coefficient
r_u	pore water pressure coefficient; a rough estimate commonly used when groundwater is considered in slope analysis
s	actual shear strength
t_i	spatial positions in a random field. $i = 1, 2, ..., a, b, n$
u_0	initial pore-water pressure
u_d	dynamic pore-water pressure
Δu	change in pore-water pressure
v	coeficient of variation
v_c	coeficient of variation for cohesion, c
v_x	coeficient of variation for a variable/parameter 'x'

v_γ	coeficient of variation for the unit weight, γ
v_ϕ	coeficient of variation for the internal friction angle, ϕ
$v_{\tan\phi}$	coeficient of variation for the tangent of the ϕ
V_s	shear wave velocity
V_{s_1}	over-burden stress corrected shear wave velocity
$V_{s_1}^*$	limiting upper value of V_{s_1} for liquefaction occurance
$V_{s_1,cs}$	clean sands over-burden stress corrected shear wave velocity
w_c	water content of the soil
W	weight of the soil mass
x	a displacement level to which the estimated displacement is compared in PSHA to determine failure
$X(t)$	a Gaussian random field
X_i	random variable at postion t_i
y	a given level of ground motion, used in PHSA
$Y(t)$	a lognormal random field
z	a given level of ground motion, used in PSHA
z_d	soil depth in liquefaction analysis
α	inclination angle of pseudo-static force
β	slope angle
γ	unit weight
Δ_d	annual rate of displacement exceedance in PSHA
θ	correlation length
θ_i	correlation length in direction i
$\theta_{\ln c}$	log-space correlation length for cohesion

$\theta_{\ln \tan \phi}$	log-space correlation length for $\tan \phi$
$\theta_{\ln x}$	log-space correlation length for a variable/parameter 'x'
λ	stability factor
μ_c	mean cohesion
$\mu_{\ln x}$	mean value of a lognormal variable/parameter 'x'
$\mu_{\tan \phi}$	mean of $\tan \phi$
μ_{ϕ}	mean friction angle
ν	Poisson's ratio
$\rho(\tau)$	correlation structure
σ_c	standard deviation of cohesion
σ_d	total normal stress
$\sigma_{\tan \phi}$	standard deviation of $\tan \phi$
σ_{vo}	total vertical over-burden stress
σ'_{vo}	effective vertical over-burden stress
$\sigma_{\ln x}$	standard deviation of a lognormal variable/parameter 'x'
$\sigma_{\ln CRR_{7.5}}$	standard deviation in the error of the natural logarithm of $CRR_{7.5}$
σ_ε	model standard deviation in the performance based liquefaction assessment
τ	spacing between positions
τ_d	shear stress
τ_e	equilibrium shear stress
τ_i	spacing between positions in direction i
ϕ	friction angle
ϕ_m	pseudo-static factored friction angle

ϕ_F	static factored friction angle
ϕ'	effective friction angle
ω	angle of the radius of a log-spiral surface
ω_0	initial angle of the radius of a log-spiral surface
ω_H	angle of the radius of a log-spiral surface for a slope height H

ACKNOWLEDGEMENTS

I would like express my thanks to my supervisor, Dr. Gordon A. Fenton, for extending to me this opportunity to learn beyond my element, and to explore how to apply that which I've learned over my academic career. I am particularly thankful for his guidance, constructive criticism, and patience, which have helped me considerably throughout the learning process of this thesis. His mentoring has been a truly invaluable experience.

This work was made possible by the generous support provided by a Special Research Project Grant from the Ministry of Transportation of Ontario (Canada), for which I am grateful.

I am grateful to my committee members, Dr. Guy Kember, Dr. Craig Lake, and Dr. Farzaneh Naghibi, for sharing their insights in the development of this work.

I also wish to extend my gratitude to my colleagues within the Engineering Mathematics department for providing a friendly and constructive work environment. Special thanks belong to the department secretary, Claire Chisholm, who continues to go above and beyond for both faculty and students. Additionally, I am sincerely thankful to the department head, Dr. William Phillips, as well as Dr. Wendy Gentleman and Dr. Farzaneh Naghibi, for their invaluable advice throughout the thesis process.

Finally, I am beyond grateful to my family for their constant support throughout the entirety of my academic career.

CHAPTER 1

INTRODUCTION

1.1 GENERAL

Earthen slopes and embankments are commonly occurring geotechnical structures, be they naturally formed, cut, or constructed. Slopes can often be found near or as part of a larger geotechnical system, such as roadways, bridges, and dams. As such, earthen slopes are routinely analyzed for their stability so as to prevent collapse, and potential damage, from occurring. Traditionally, evaluation of slopes, such as the one shown in Figure 1.1, was simplified by determining the average shear strength of the soils through sampling, and consulting existing design chart for the slopes' particular geometries. For situations based upon static loading, where only the gravitational load is considered, such design charts have been extensively researched for a broad range of geometries and soil conditions both deterministically and, to a lesser extent, probabilistically. It is often the case, however, that the serviceability of a slope is in part reliant upon its response to extreme events such as earthquakes, which may cause significant slope deformation due to a rapid reduction in the strength of the soil mass.

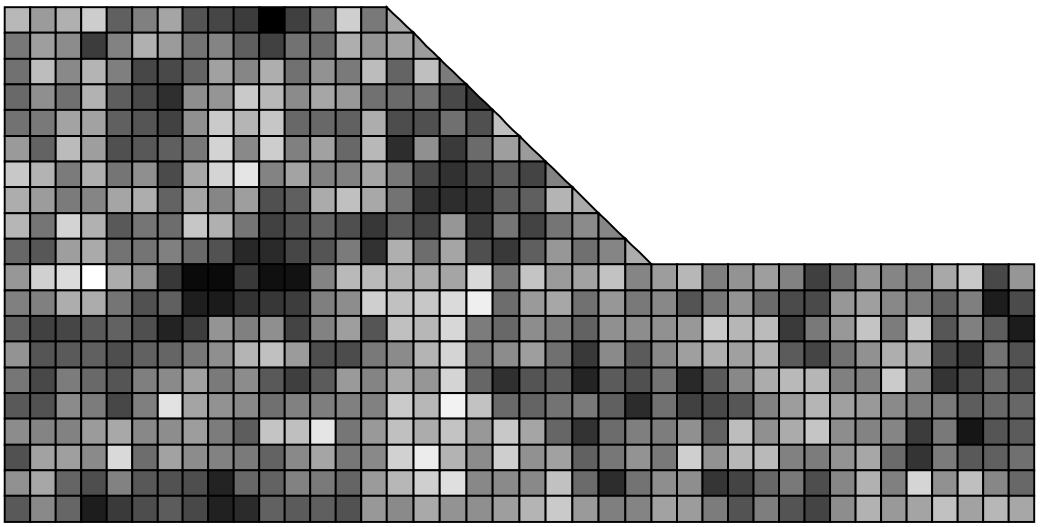

Figure 1.1 Sample diagram used in slope analysis

Despite difficulties in predicting the dynamic response of slopes due to earthquakes, analysis of slope stability subject to seismic loading has been given considerable attention (see, e.g. Mostyn and Small, 1987). Geotechnical researchers have developed methodologies to overcome computational limitations and generate rough estimates of slope stability through application of static-forcing which is equivalent to the dynamic load. Use of such methods has allowed for the generation of several sets of deterministic design charts (e.g. Loukidis et al., 2003) which roughly estimate the maximum amount of seismic excitation a slope can withstand before failing. For simple slopes, use of such charts allows geotechnical engineers a means to quickly estimate the seismic stability of a slope without having to determine anything more than the soil strength parameters and slope geometries already used in static slope analysis. However, the design charts currently used in seismic slope analysis lack the means to account for the spatial variability of soils, which may result in weakened portions of soil being overlooked. As such, the risk of slope failure from those weakened sections excited by seismic motion may be masked by deterministic evaluations.

1.1.1 Thesis Objective

The objective of this work is the development of a design procedure for slopes subject to seismic loading. To provide a procedure that quantifies the margin of safety of a slope, the analysis within this work seeks to link the traditional factor of safety approaches common in seismic analysis with probabilities of failure which capture the influence of variability in soil strength parameters. By incorporating the results of this work into seismic design charts, styled similarly to existing charts commonly used in practice, a procedure may be developed to assist geotechnical engineers in the safe design of slopes when earthquake loading is considered.

1.2 DETERMINISTIC SLOPE DESIGN METHODOLOGIES

Static slope stability analysis has been extensively developed in the past, with several alternative approaches being described in geotechnical textbooks such as Coduto et al. (2011). A typical slope problem, such as the one displayed in Figure 1.2, relies upon a variety of slope parameters. Of particular importance in slope stability analyses are the cohesion, c, and the internal friction angle, ϕ, which jointly determine the shear strength of soils. Other key parameters identified in Figure 1.2 are the height of the slope, H, the depth factor, D, the slope angle, β, and the unit weight of soil, γ. Numerous evaluation procedures use the parameters indicated in Figure 1.2 to determine the static stability of the slope. Typically, Young's modulus, E, and Poisson's ratio, ν, are not of key importance in the evaluation of slope stability (although they are used to evaluate deformation), and are often left as nominal values (s and Lane, 1999).

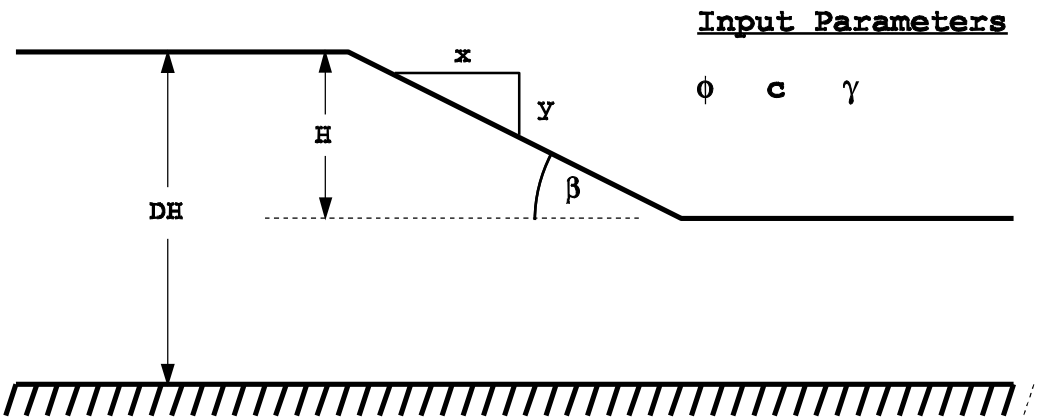

Figure 1.2 The static slope stability problem

1.2.1 Limit Equilibrium Approaches

Many approaches to the static slope stability problem are based on the concept of limit equilibrium, which seeks to determine if the soil mass will slide (fail) under gravitational loading along a planar or circular failure surface. The determination of equilibrium is assessed through the static factor of safety, F, defined as the ratio of stress caused by gravitational loading upon a slope to the stress at which the slope mass will fail. The factor of safety is evaluated using the expression (Coduto et al., 2011):

$$F = \frac{s}{\tau_e} \tag{1.1}$$

where s is the actual shear strength determined from the Mohr-Coulomb failure criterion for elasto-plastic materials, and τ_e is the equilibrium shear stress (the required shear strength to maintain equilibrium) determined from the shear force acting along the failure surface. The factor of safety is assumed to be constant along the entire failure surface (Coduto et al., 2011). Theoretically, a value of $F > 1$ indicates that the slope remains stable, however practical design criteria tend to require a higher value, typically $F \geq 1.5$ to account for

uncertainty. Lower values, for example $1.2 \leq F \leq 1.3$, may be acceptable in non-essential and temporary slope analyses (Coduto et al., 2011; NZ Transport Agency, 2013). Duncan (1996) summarized a large number of limit equilibrium methodologies, such as the ordinary method of slices (Fellenius, 1936), Bishop's Modified method (Bishop 1955), and Spencer's method (Spencer, 1967), which account for varying shear strength along the failure surface by discretizing the failure surface into smaller components, or 'slices'.

1.2.2 Log-Spiral Failure Surfaces

Another approach to the evaluation of slope stability is through a kinematical limit analysis. Chen (1975) described the most efficient kinematical approach to slope stability problems as one which follows a rotational failure mode, and possesses a log-spiral failure surface defined by:

$$r = r_0 \exp\Big((\omega - \omega_0)\tan\phi)\Big) \tag{1.2}$$

where r is the radius of the log-spiral at the angle ω, and r_0 and ω_0 are the initial values of these two parameters. For a static stability number, N, defined as $N = (c/\gamma H)(1/F)$, the critical height of the slope (the maximum height a slope, with a particular combination of slope angle and soil strength parameters, can be before failure occurs, i.e. $F = 1$) is determined by the expression:

$$H = \frac{2r_0 \tan\phi(f_1 - f_2 - f_3 - f_4)}{N\,(\exp[2(\omega_H - \omega_0)\tan\phi] - 1)} \tag{1.3}$$

where ω_H is the angle of the log-spiral failure surface at the critical height, and the functions f_1 to f_4 are dependent upon ω_0, ω_H, and β, and are defined by Chen (1975). Alternatively, if H, c and γ are known, the formula may be solved for the factor of safety, F, for c-ϕ soils as follows:

$$F = \frac{2(\omega_H - \omega_0)\tan\phi}{\ln\left[1 + \frac{2\gamma H}{c} r_0' \tan\phi(f_1 - f_2 - f_3 - f_4)\right]} \tag{1.4}$$

which, for purely cohesive soils ($\phi = 0$), reduces to:

$$F = \frac{1}{r_0'} \frac{c(\omega_H - \omega_0)}{\gamma H(f_1 - f_2 - f_3 - f_4)} \tag{1.5}$$

where $r_0' = r_0/H$ and r_o/H is deemed to be a radial factor which depends upon angles of rotation, w_0, w_H, and the slope angle β.

This approach to slope stability analysis generally assumes homogeneous soil masses and no influence from pore water pressure, yielding results which are roughly equivalent to Bishop's simplified method. Interested readers are directed to the work of Chen (1975) for the basis of this approach, and the work of Michalowski (1995) which compares this approach to limit equilibrium methodologies based upon slices and translational failure mechanisms.

1.2.3 Chart Solutions

Stability charts are traditional geotechnical design tools used to estimate the factor of safety for simple slopes (homogeneous slopes with geometry such as illustrated in Figure 1.2). Development of stability design charts for slopes relies upon fundamental assumptions regarding the soil strength parameters and the failure surface. For example, Taylor (1937) developed stability charts for purely cohesive ($\phi = 0$) slopes with a circular failure surface; Cousins (1978) produced stability charts for homogeneous cohesive-frictional (c-ϕ) slopes with a critical failure surface (the failure surface with which possesses the lowest F value) that must pass through the toe of the slope; Michalowski (2002) used a kinematic equilibrium approach with a log-spiral failure mechanism; Baker (2003) extended Taylor's (1937) charts to include ϕ; and Steward et al. (2011) used limit equilibrium and circular slip analysis to produce a single-iteration chart for c-ϕ soils.

1.2.4 Finite Element Modeling of Slopes

A major advantage of finite element analysis of slopes is that it does not require assumptions regarding the shape or location of the failure surface. The finite element method discretizes the slope into a number of finite elements called a mesh. Smith and Griffiths (1988, 1998), describe a finite element program which models a slope, consisting of an elasto-plastic soil (Mohr-Coulomb material), subjected to gravity loading. The program utilizes eight-node quadrilateral elements to discretize a two-dimensional, planar slope such as the one displayed in Figure 1.2. Factor of safety values of the slope are determined using an incremental loop based upon the shear strength reduction technique, which defines F as the factor by which both c and $\tan\phi$ must be reduced in order to cause failure to occur in the elastic-plastic analysis. Failure occurs when the numerical solution is unable to converge within a set amount of iterations (Griffiths and Lane, 1999). The reduced, or 'factored', soil strength parameters that just lead to slope failure are:

$$\phi_F = \tan^{-1}(\tan\phi/F) \tag{1.6a}$$

$$c_F = c/F \tag{1.6b}$$

The program developed by Smith and Griffiths (1988, 1998) was extended by the work of Griffiths and Lane (1999) to model more general slope/embankment geometries and soil properties (such as pore water pressure). Within their work, Griffiths and Lane (1999) showed the ability of the finite element method to examine complex problems which do not adhere to the fundamental assumptions used in many conventional limit equilibrium approaches, such as slopes containing secondary layers or thin weak layers, and partially submerged embankments. Furthermore, Smith and Griffiths' (1988, 1998) program has been combined with random field modeling to examine the stability of slopes in terms of the probability of failure, as discussed in Griffiths and Fenton (2000, 2004) and Fenton and Griffiths (2008).

1.3 PROBABILISTIC SLOPE STABILITY ANALYSIS

1.3.1 Random Fields

When examining the geotechnical failure mechanisms of slopes, realistic spatial variability in soil properties may be accounted for using random fields. Random fields represent collections of interdependent random variables, each associated with a spatial location, t. For example, a random field, denoted by $X(t)$, would consist of the random variables $X(t_1) = X_1$, $X(t_2) = X_2$, ..., $X(t_n) = X_n$ at positions t_1, t_2, ..., t_n, where n is the number of random variables used to represent the field. The values of the random field exhibit both variability and dependence between pairs of random variables, $X(t_a)$ and $X(t_b)$, separated by distance $\tau = t_a - t_b$. The set of random variables X_1, X_2, ..., X_n will, in general, have an n-dimensional probability density function, which is usually simplified (as is the case in this research) by assuming that $X(t)$ is a stationary, isotropic, Gaussian process. Interested readers are directed to VanMarcke (1984), and Fenton and Griffiths (2008) for more details. The resulting random field is fully described by its mean, standard deviation, and correlation structure, $\rho(\tau)$. To simplify calculations, this study defines $\rho(\tau)$ as the Markov correlation function:

$$\rho(\tau) = \exp\left(\frac{-2|\tau|}{\theta}\right) \tag{1.7}$$

where θ, known as the correlation length, represents the separation distance within which two points will be significantly correlated, and is defined to be:

$$\theta = \int_{-\infty}^{\infty} \rho(\tau)d\tau = 2\int_{0}^{\infty} \rho(\tau)d\tau \tag{1.8}$$

For a two-dimensional, isotropic process, $\rho(\tau)$ becomes:

$$\rho(\tau) = \exp\left(-\sqrt{\left(\frac{2|\tau_x|}{\theta_x}\right)^2 + \left(\frac{2|\tau_y|}{\theta_y}\right)^2}\right) = \exp\left(\frac{-2|\tau|}{\theta}\right) \tag{1.9}$$

where the subscripts 'x' and 'y' on τ and θ denote their respective directional components, and the correlation structure is assumed to be isotropic so that $\theta = \theta_x = \theta_y$, and $|\tau| = \sqrt{\tau_x^2 + \tau_y^2}$.

1.3.2 Random Field Modeling of Soils

As noted previously, the two most important soil strength parameters in slope stability analysis are the cohesion, c, and the internal friction angle, ϕ. Both c and $\tan\phi$ are assumed to be lognormally distributed with means μ_c and $\mu_{\tan\phi}$, and standard deviations σ_c and $\sigma_{\tan\phi}$, respectively. Lognormal fields may be derived from Gaussian fields using a simple transformation. If $X(t)$ is a Gaussian field, the lognormally distributed random field $Y(t)$ is obtained through:

$$Y(t) = e^{X(t)} \tag{1.10}$$

which possesses a correlation structure, defined by (Fenton and Griffiths, 2008) as:

$$\rho_Y(\tau) = \frac{\exp\left\{\sigma_X^2 \rho_X(\tau)\right\} - 1}{\exp\left\{\sigma_X^2\right\} - 1} \tag{1.11}$$

For both soil strength parameters, the associated lognormal parameters $\mu_{\ln x}$ and $\sigma_{\ln x}$, where '$\ln x$' denotes a lognormally distributed parameter (such as c or $\tan\phi$), are derived from μ_x and σ_x through the transformations:

$$\sigma_{\ln x}^2 = \ln(1 + v_x^2) \tag{1.12}$$

$$\mu_{\ln x} = \ln(\mu_x) - \frac{1}{2}\sigma^2_{\ln x} \tag{1.13}$$

where v_x is the coefficient of variation of the parameter x, defined by

$$v_x = \frac{\sigma_x}{\mu_x} \tag{1.14}$$

Phoon and Kulhawy (1999) present ranges of the coefficient of variation for the soil strength parameters c, ϕ, and γ. The recommended range of values for cohesion was given to be $0.1 \leq v_c \leq 0.5$, and for internal friction angle was $0.1 \leq v_\phi \leq 0.2$. The coefficient of variation for the unit weight of soil, γ, found to be $v_\gamma \leq 0.1$, is typically neglected (i.e. $v_\gamma = 0$) in probabilistic studies, as is done here.

These soil properties also possess associated correlation lengths, $\theta_{\ln c}$ and $\theta_{\ln \tan \phi}$. Low values of θ indicate rapid variability within the soil mass, while large values of θ will result in gradual variation, as illustrated in Figure 1.3. To further simplify the random field model, it may be assumed that the correlation lengths of the two soil parameters are equal so that $\theta_{\ln c} = \theta_{\ln \tan \phi} = \theta_{\ln x}$. In practice the log-space correlation length, $\theta_{\ln x}$, is not very different from its real-space counterpart θ_x (see Appendix A). As such the two measures can be used interchangeably, for most purposes, due in part to the inherent uncertainty in the measures.

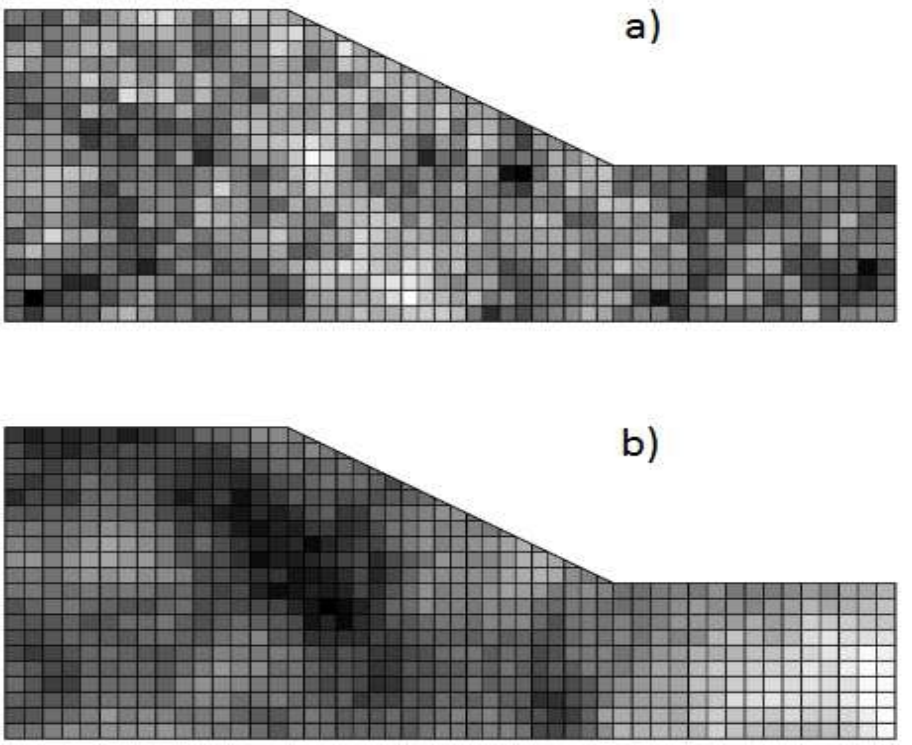

Figure 1.3 Sample random field realizations for slopes with correlation length a) $\theta = 0.2H$, and b) $\theta = 5H$

1.3.3 Single Random Variable Approach

Many geotechnical engineers have been slow to adopt the use of random fields in their probabilistic studies of slopes. A common alternative makes use of the Single Random Variable (SRV) approach (e.g. Harr, 1987; Duncan, 2000; Javankhoshdel and Bathurst, 2014), which is equivalent to setting θ to ∞ in a random field. An infinite correlation length yields a homogeneous field, meaning that the soil strength parameters are constant throughout the soil mass, but random from realization to realization. Probabilistic analysis then typically consists of a combination of limit-equilibrium circular slip surface analysis (e.g. Bishop's simplified method), and Monte Carlo simulations. The soil strength parameters vary randomly from one realization of the homogeneous soil to the next, and the probability

of failure is determined by the ratio of failed realizations to the total number of realizations performed. Javankhoshdel and Bathurst (2014) conducted an extensive study using the SRV approach to extend the simplified deterministic slope stability design charts described in section 1.2.3 into the realm of probabilistic analysis. In their study, Javankhoshdel and Bathurst (2014) examined a wide range of slope angles (β = 10° to 90°), various internal friction angles (μ_ϕ = 20°, 25°, 30°, 35°, 40°, and 45°), and several combinations of coefficients of variation for c and ϕ based upon recommendations by Phoon and Kulhawy (1999) to produce probabilistic static slope design charts. The traditional factor of safety, found through deterministic analysis, was shown to be an imperfect measure of the margin of safety of slopes, as some slopes with $F >> 1$ still exhibited considerable probabilities of failure. This behaviour is the result of the factor of safety being evaluated at the mean values of the random variables associated with c and ϕ, thereby neglecting the spatial variability of the soil observered from one realization to the next. As homogeneous slope masses are unlikely to occur in real-world slope problems, the SRV approach provides geotechnical engineers with a conservative estimate of slope stability failure probabilities. To account for realistic spatial variability in the soil strength parameters, the correlation length should be set to a non-infinite value, as is the case in the Random Finite Element Method (RFEM), discussed next.

1.3.4 Random Finite Element Method

Application of random fields to the slope stability problem has been implemented and extensively investigated by Griffiths and Fenton (2000, 2004). These authors developed a computer program, RSLOPE2D, which combines the eight-nodal finite element model of Smith and Griffiths (1988, 1998), with random field theory (e.g., VanMarcke, 1984) to realistically account for spatial variability in the soil strength parameters and to allow the failure mechanism to naturally seek out the weakest failure path. Two random fields, one

for each of cohesion and internal friction angle, are mapped to a finite-element mesh used to discretize a slope, such as the one illustrated in Figure 1.4, so that each element within the mesh has assoicated random variables for c and ϕ. The size of the elements the random variables are associated with is accounted for by means of the local average subdivision (LAS) algorithm developed by Fenton and VanMarcke (1990).

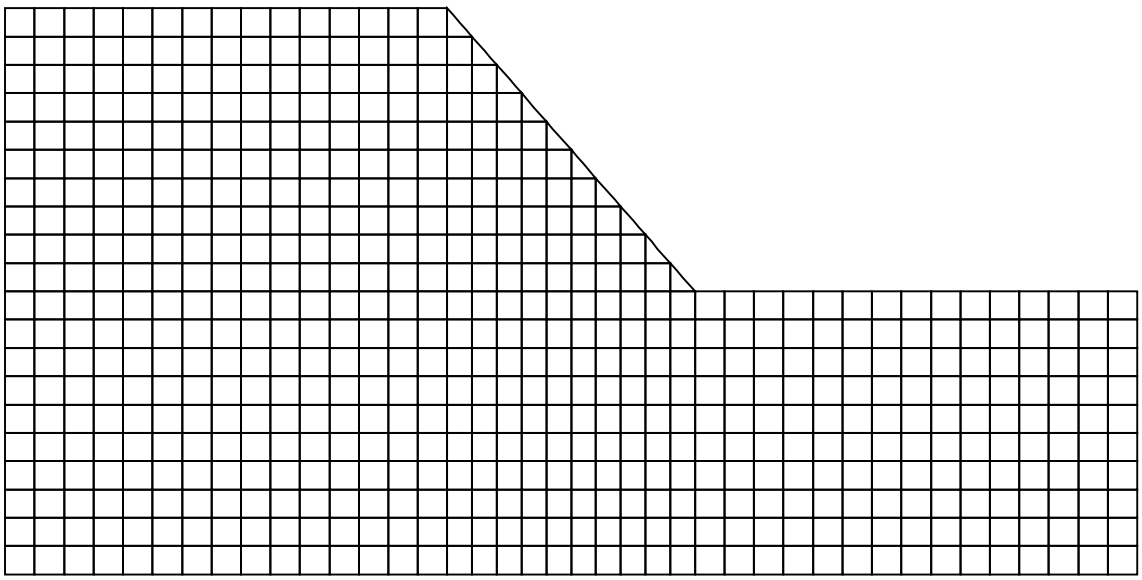

Figure 1.4 Mesh used in slope stability analysis

The random variables are correlated with one another according to the spatial correlation length θ, in accordance with equation (1.9), as discussed previously. From Figure 1.3, it may be observed that the homogeneous portions of the soil mass continue to grow as $\theta \rightarrow \infty$, and, as such, the SRV approach may be considered to be a special case of the RFEM. In Griffiths and Fenton (2000), the influence of the correlation length was studied in depth using RFEM and compared to the SRV approach for cohesive soils. It was found that for $0 < v_c < 0.5$ the probability of slope failure increased as the ratio $\theta_{\ln c}/H$ increased, indicating that the SRV approach is more conservative than the RFEM approach for this range. Considering the design recommendations of Phoon and Kulhawy (1999), the spatial

variability typically used in practice will always indicate that the SRV approach is more conservative. However, Griffiths and Fenton (2000), also noted that there are instances in which RFEM is more conservative than SRV when $F > 1.4$ for static slopes. Where the interest is in the effects of realistic spatial-variability of soil strength parameters and non-linear failure mechanisms, the RFEM should be considered for analysis.

1.4 SEISMIC DESIGN OF SLOPES

1.4.1 Dynamic Analysis

Evaluation of the response of earthen slopes to earthquakes is a dynamic geotechnical problem in which both the input loading caused by the seismic event and the deformation behavior of the soil mass change over time. Peak acceleration- and velocity-time curves are often used to represent seismic motion acting upon a slope, and require the effective stress-strain behavior of the soil material to undergo constant re-evaluation as a function of time. Rigorous evaluation of the response of slopes to seismic events requires a numerical solution derived from the boundary value problem defined by the slope geometry, and typically assuming elasto-plastic materials. Such an approach is capable of accounting for a variety of soil conditions, such as weakening soil strength due to cyclic loading, liquefaction potential, and the effects of groundwater, allowing dynamic modeling of the seismic slope problem to examine any failure mechanism the slope may undergo. However, as noted by Baker et al. (2006), dynamic approaches are limited by the need for reliable characterization of the site material, including spatial variability, and the inability to predict the exact ground motion (acceleration, velocity) that will occur. Application of techniques such as the RFEM may allow for the simulation of soil strength parameters in the soil mass through the use of random variables for each finite element, however, the addition

of random ground motion acting upon each element over time and consideration of each possible failure mechanism (sliding, liquefaction, etc.) creates a complex, computationally demanding problem. For example, since the seismic input is random, a dynamic model would need to simulate a variety of ground motion inputs (based upon statistical estimates of motion for the particular region) for each realization of the random soil properties, thereby compounding the computational demand. With regards to the complexity of the dynamic approach, many design procedures, specifications and guidelines (USACE, 1989; Eurocode 8, 1993; IITK-GSDMA, 2005; NZ Transport, 2013; and others) use a simpler pseudo-static (sometimes referred to as "equivalent-static") approach to assess most conventional slopes. Only those slopes deemed important, inherently complex, or those which fail under the pseudo-static approach, would undergo further dynamic analysis. To keep the computational requirements reasonable, this study will adopt only a pseudo-static approach. Readers interested in fully dynamic seismic slope analysis are referred to the summary of dynamic methods by Mostyn and Small (1987) as a starting point.

1.4.2 Pseudo-static Analysis

The pseudo-static analysis is a simple way to account for seismic effects upon a slope. The pseudo-static approach applies a constant horizontal acceleration (known as the pseudo static acceleration; vertical motion is not considered in this study) to a mass to account for earthquake effects (Mostyn and Small, 1987). The horizontal acceleration is considered to continue for a period of time necessary to result in slope failure, if it is going to fail, and thus acts in a direction which destabilizes the slope as a static force (Coduto et al., 2011). Computations proceed similar to typical limit equilibrium analysis with the added influence of this horizontal force, which lowers the factor of safety as the seismic loading increases (Coduto et al., 2011). For $c - \phi$ soils, Sarma (1973) describes the pseudo-static factor of safety as:

$$F_s = \frac{(\sigma_d - u_d)\tan\phi'}{\tau_d} \tag{1.15}$$

where σ_d is the total normal stress, τ_d is the shear stress, u_d is the dynamic pore water pressure, all of which are induced under seismic loading, and ϕ' is the effective friction angle of the soil. Sarma (1973) further defines σ_d, τ_d, and u_d to be as follows:

$$\sigma_d = \frac{W}{a}[\cos\beta - k\sin(\beta - \alpha)] \tag{1.16}$$

$$\tau_d = \frac{W}{a}[\cos\beta + k\sin(\beta - \alpha)] \tag{1.17}$$

$$u_d = u_0 + \Delta u \tag{1.18}$$

where W denotes the weight of the sliding block, a is the base area of the block, β represents the inclination angle of the slope, measured from the horizontal, α represents the inclination of the pseudo-static force acting upon the slope, measured from the horizontal, k is the seismic coefficient, an acceleration measured as a fraction of gravity, g, and u_0 and Δu represent the static and induced pore water pressures, respectively. This work will only consider the case of a purely horizontal pseudo-static force ($\alpha = 0°$).

1.4.2.1 Pseudo-Static Stability Charts

For seismic slope design, pseudo-static stability charts have been developed in numerous studies (Leschinsky and San, 1994; Michalowski 2002, Loukidis et al. 2003, Baker et al. 2006) to aid in the determination of whether a homogeneous slope will fail under a certain seismic acceleration. The charts vary in what parameters are included. For instance, Leschinsky and San (1994) provide charts for a slope angles, β, (expressed as height to length ratios) that plot the pseudo-static stability number, N_m, against a factored friction angle, ϕ_m, as a function of the seismic coefficient, k, and a stability factor, λ. N_m, ϕ_m, and λ are defined by:

$$N_m = \frac{1}{F_s}\frac{c}{\gamma H} \tag{1.19}$$

$$\phi_m = \tan^{-1}\left(\frac{\tan\phi}{F_s}\right) \tag{1.20}$$

$$\lambda = \frac{c}{\gamma H \tan\phi} \tag{1.21}$$

where F_s is the target pseudo-static factor of safety, c is the cohesion of the soil, γ is the unit weight of the soil mass, H is the height of the slope, and ϕ is the internal friction angle of the soil. Similarly, Michalowski (2002) plots $F_s/\tan\phi$ against λ for particular k values; Loukidis et al. (2003) plot λ against k_c for a particular slope angle, with separate curves for ϕ values that correspond to the critical condition that $F_s = 1$ for both finite element analysis and log-spiral failure surfaces; Baker et al. (2006) plot k_c against N_m with $F_s = 1$ for a set of slope angles, with curves for ϕ values.

1.4.2.2 Limitations of the Pseudo-Static Approach

While the application of a static force to represent the horizontal seismic loading during an earthquake allows for a simplification of the model (as opposed to a fully dynamic model), the simplification provides only an approximation of the response of a real earth slope (Coduto et al., 2011). The pseudo-static approach fails to account for the cyclic nature of the seismic motion (in that real-world seismic acceleration first occurs in one direction, then the other), thereby neglecting the overall dynamic response of the slope to the ground motion (Loukidis et al., 2003). Furthermore, the wavelengths of seismic waves are generally smaller than the dimension (in the direction of the crest) of most slopes, resulting in portions of the slope acting opposite each other (Coduto et al., 2011). Due to these differences from reality, the pseudo-static analysis should not be based upon historical peak ground accelerations (often greater than $0.7g$) since it is likely that use of recorded peak ground acceleration would always indicate failure (Coduto et al., 2011). The pseudo-static approach should instead be based upon observed behavior, resulting in the analysis

being akin to an empirical index, and commonly one which is overly conservative (Coduto et al., 2011). It should also be noted that the pseudo-static approach is not accurate for saturated soils with high liquefaction potential, or soils which rapidly lose strength when loaded cyclically (Loukidis et al., 2003). Furthermore, since the pseudo-static approach is an approximation of the seismic effects, combinations of other simplified concepts (such as use of the distribution of pore water pressure coefficient, r_u) with the seismic coefficient, k, may not appropriately capture the true safety margin of slopes (Michalowski, 2002). Most pseudo-static stability charts are based upon circular failure surfaces, log-spiral failure surfaces, or set failure path restrictions which are not usually representative of actual slope failures. Nevertheless, the pseudo-static approach is still commonly used as a means to determine whether failure is likely to occur. In practice, pseudo-static analysis is typically reserved for use when a slope has minimal liquefaction potential and a static factor of safety below 1.7; Hynes-Griffin and Franklin (1984) note that slopes with a static factor of safety in excess of 1.7 have never been observed to fail from seismic loading. Existing pseudo-static slope stability design charts allow for the assessment of a slope having a particular slope angle over a range of friction angles. However it may be more effective for design purposes to have stability charts which allow for a direct selection of β by comparing a range of slope angles for known values of the soil strength parameters, c and ϕ. While pseudo-static stability charts provide a means for designers to obtain reasonable estimates of whether a slope may fail during a seismic event, they do not express the extent of the damage should the critical acceleration be exceeded. When the interest is in identifying the displacement that will occur, rather than whether it will occur or not, the method developed by Newmark (1965), discussed next, is used.

1.4.3 Newmark's Method

Newmark (1965) developed an approach to predict permanent seismic slope displacements during an earthquake by building upon the pseudo-static approach. Newmark first estimated a critical seismic coefficient, k_c (the ratio of the critical acceleration causing slope failure, and the acceleration due to gravity), which corresponds to when equation (1.15) is equal to unity ($F_s = 1$). Next, an acceleration versus time plot for the design earthquake is considered and the time intervals when the earthquake acceleration surpasses the yield acceleration, $a_{yield} = k_c g$, are noted. Landslide displacement is then estimated by double integrating (with respect to time) the acceleration curve within the noted intervals.

While Newmark's method is an extension of pseudo-static analysis, it is still a highly simplified approach, especially when considering the sensitivity of the method to the selected critical acceleration. Bray (2007) suggested that Newmark's model is able to capture the part of the seismically induced permanent displacement caused by deviatoric shear deformation, but fails to account for ground motion due to volumetric compression. The simplified nature of Newmark's approach comes in part from the few ground-motion records available at the time of Newmark's publication (Jibson, 2007). Nonetheless, Newmark's Method is considered a landmark within the field of seismic slope modeling, and Newmarkian models have been developed extensively to build upon it (Bray, 2007).

1.4.3.1 Expansion Upon Newmark's Method

Many researchers expanded upon Newmark's method (1965) when data and computers became more accessible; Sarma (1973) developed a method to determine the critical seismic coefficient, k_c, directly; Makdisi and Seed (1978) developed a modification of Newmark's Method which was found to be better suited for deep-seated failure surfaces (Rathje and Saygili, 2011); and Chugh (1983) used the Method of Slices to develop a dynamic model based upon Newmark's Method. The above are but a few among many that expanded upon

Newmark's work. A suggested starting point for further information regarding Newmarkian models is the work of Bray (2007) which reviews Newmark's method and other approaches.

1.4.3.2 Probabilistic Seismic Hazard Analysis

One example of probabilistic expansion of Newmark's method is the work of Rathje and Saygili (2008, 2009, and 2011). Rathje and Saygili (2008) describe a methodology for producing displacement hazard curves. These curves provide the annual rate of exceedance, Λ_d, of a sliding-block displacement, d, exceeding given displacement levels, x, for a given ground motion parameter (such as peak ground acceleration, PGA, or peak ground velocity, PGV), using a probabilistic framework. There are two approaches in the development of their hazard curves, a scalar approach based upon a single ground motion parameter (typically PGA) and a vector approach based upon two or more ground motion parameters (typically PGA and PGV). The scalar approach was defined as:

$$\Lambda_d(x) = \int \mathrm{P}[d > x | GM = z] * \mathrm{MRD}(z) * dz \tag{1.22}$$

and the vector approach was defined as:

$$\Lambda_d(x) = \int \int \mathrm{P}[d > x | GM1 = z, GM2 = y] * \mathrm{MRD}_{GM1,GM2}(z, y) * dz * dy \tag{1.23}$$

where GM represents a placeholder variable for the ground motion variables PGA and/or PGV, and z and y are given levels of ground motion. The first term in the integrals represents the probability of the displacement exceeding a particular hazard level, x, given certain ground motion levels, y and z; the second term in the integrals, MRD, is the mean rate density of the ground motion, which is analogous to a probability density function.

The pseudo-probabilistic approach in Rathje and Saygili (2011) is directly adapted from their 2009 paper. Rathje and Saygili (2009) modified the equations from their 2008 paper to define a predictive model for displacement based upon probabilistic seismic hazard

analysis (PSHA) derived ground motion levels. The PSHA-derived ground motion predicts the displacement by using the critical acceleration, k_c, of the slope based upon Newmarkian sliding block analysis. The modified model for both scalar and vector approaches and the equations for their associated standard deviations are, for the scalar case:

$$\ln d = a_1 + a_2\left(\frac{k_c}{\text{PGA}}\right) + a_3\left(\frac{k_c}{\text{PGA}}\right)^2 + a_4\left(\frac{k_c}{\text{PGA}}\right)^3 + a_5\left(\frac{k_c}{\text{PGA}}\right)^4 + a_6\ln(\text{PGA}) + a_7(M_w - 6) \tag{1.24a}$$

$$\sigma_{\ln d} = a_8 + a_9\left(\frac{k_c}{\text{PGA}}\right) + a_{10}\left(\frac{k_c}{\text{PGA}}\right)^2 \tag{1.24b}$$

and for the vector case:

$$\ln d = a_1 + a_2\left(\frac{k_c}{\text{PGA}}\right) + a_3\left(\frac{k_c}{\text{PGA}}\right)^2 + a_4\left(\frac{k_c}{\text{PGA}}\right)^3 + a_5\left(\frac{k_c}{\text{PGA}}\right)^4 + a_6\ln(\text{PGA}) + a_7\ln(\text{PGV}) \tag{1.25a}$$

$$\sigma_{\ln d} = a_8 + a_9\left(\frac{k_c}{\text{PGA}}\right) \tag{1.25b}$$

where d is the sliding-block displacement of the soil mass, measured in centimeters; k_c and PGA are defined in units of gravity (g); M_w is moment magnitude; PGV is in cm/s, and a_1 to a_{10} are regression coefficients provided in Rathje and Saygili (2011). Rathje and Saygili (2011) go on to state that the vector approach is preferable to the scalar approach due its better ability to include frequency content, as well as having a significantly smaller standard deviation. As with equations (1.24) and (1.25), the fully probabilistic approach of Rathje and Saygili (2011) is defined for both a scalar and a vector case. For the scalar case the rate of exceedance is defined by:

$$\Lambda_d(x) \cong \sum_i \sum_j \text{P}[d > x | PGA_i, M_{w_j}] * \text{P}[M_{w_j} | PGA_i] * \text{P}[PGA_i] \tag{1.26a}$$

and for the vector case:

$$\Lambda_d(x) \cong \sum_i \sum_k \text{P}[d > x | PGA_i, PGV_k] * \text{P}[PGA_i, | PGV_k] \tag{1.26b}$$

where the double summations approximate numerical integration with respect to moment magnitude and/or the ground motion parameters PGA and PGV.

1.5 LIQUEFACTION

Liquefaction refers to the transformation of granular material from a solid to liquefied state due to an increase in pore-water pressure and reduced effective strength. During a seismic event, increased pore-water pressure is induced by cyclic shear deformations generated by ground motion, resulting in compaction of the soil framework. Increased pore-water pressure can be especially dangerous if it results in flow failure occurring beneath a foundation or sloping ground, the likelihood of which is dependent upon the behavior of the soil material. In loose materials (such as silts and sands), softening is accompanied by a loss of shear strength and a tendency to contract. Contraction occurs when the volume of fluid-filled spaces between soil particles is reduced as a result of the soil particles moving closer together. The combination of such contractive behaviour with shear strength loss may lead to large shear deformations, or potential flow failure under moderate to high shear stresses (Youd et al., 2001). Comparatively, denser materials undergoing liquefaction experience short-term softening and increased cyclic shear strain, but have a tendency to dilate. Dilation refers to an increase in the volume of the space between soil particles as the particles move further apart. Dilation of dense soil particles during shear inhibits major strength loss and large ground deformations (Youd et al., 2001).

Dramatic and destructive earthquake-induced slides are typically the result of liquefaction (Coduto, 2011). Considering that dense, dilative soils allow for the application of the analysis techniques described in section 1.4, whereas loose, contractive soils result in the additional complexities of liquefaction, a common approach in seismic analysis is to first assess the liquefaction potential of the soil. Various in-situ tests are available to estimate the liquefaction potential of slopes. These in-situ techniques have been continuously updated (Youd et al., 2001; Idriss and Boulanger, 2006) while probabilistic methods for assessing liquefaction likelihood are under development (Cetin et al., 2004; Juang et al., 2002; Boulanger and Idriss, 2012; Franke and Wright, 2013).

1.5.1 Empirical/In-situ Approach

Seed and Idriss (1971) developed a "simple procedure" which defines the factor of safety against liquefaction, F_L, as:

$$F_L = \left(\frac{CRR_{7.5}}{CSR}\right) MSF \tag{1.27}$$

where CSR is the cyclic stress ratio, which expresses the seismic demand upon a soil layer; $CRR_{7.5}$ is the cyclic resistance ratio that defines the capacity of a soil to resist liquefaction (the critical CSR at which liquefaction will occur) at an earthquake magnitude of 7.5; and MSF is called the magnitude scaling factor for the evaluation of F_L at magnitudes other than 7.5. The CSR at a particular depth, z_d, is calculated from:

$$CSR = 0.65\left(\frac{a_{\max}}{g}\right)\left(\frac{\sigma_{vo}}{\sigma'_{vo}}\right) r_d \tag{1.28}$$

where $a_{\max}$ is the peak horizontal acceleration at the ground surface generated by the earthquake; g is the acceleration due to gravity; σ_{vo} and σ'_{vo} are total and effective vertical over-burden stresses at depth, z_d, respectively; and r_d = stress reduction coefficient which defines the flexibility of the soil profile at depth, z_d:

$$r_d = \frac{1.000 - 0.4113 z_d^{0.5} + 0.04052 z_d + 0.001753 z_d^{1.5}}{1.000 - 0.4177 z_d^{0.5} + 0.05729 z_d - 0.006205 z_d^{1.5} + 0.001210 z_d^{2}} \tag{1.29}$$

MSF values are available from multiple sources, as outlined in Youd et al. (2001), and are constantly being updated. $CRR_{7.5}$ values are calculated based upon the in-situ index tests used to estimate the soil characteristics of a site. The most common tests used to estimate liquefaction potential are the standard penetration test (SPT) and cone penetration test (CPT), although liquefaction potential is also being assessed using shear wave velocity (V_S) and the Becker penetration test (BPT) (Youd et al., 2001; Idriss and Boulanger, 2006). Due to uncertainty in the in-situ tests, a variety of correction factors may need to be applied and additional tests may need to be run to be certain of results (Youd et al., 2001). The in-situ tests and their correction factors are constantly being improved (Idriss and Boulanger,

2006; Bray and Sancio, 2006). In the following subsections, only the calculation of $CRR_{7.5}$ for each of the above noted in-situ tests will be discussed; the use and performance of the in-situ tests in the field is not described.

1.5.1.1 SPT Approach

The standard penetration index-test uses the value $(N_1)_{60}$, described as a normalization of the in-situ SPT test blow count for an overburden stress of 100 kPa and a hammer efficiency of 60%. Youd et al. (2001) suggested that $CRR_{7.5}$ could be defined by the following relationship assuming clean sands (the sample consists of sand with little to no clay content) for $(N_1)_{60} < 30$:

$$CRR_{7.5} = \frac{1}{34 - (N_1)_{60}} + \frac{(N_1)_{60}}{135} + \frac{50}{[10 \cdot (N_1)_{60} + 45]^2} - \frac{1}{200} \tag{1.30}$$

In the case where $(N_1)_{60} \geq 30$ the soil composition is thought to consist of clean granular soils, which are considered to be too dense to liquefy, and are classified as non-liquefiable. The clean sands approximation is based upon the fines content (f_c) within the soil, such that $(N_1)_{60,cs} = b_1 + b_2(N_1)_{60}$, where b_1 and b_2 vary based upon f_c. Additional correction factors exist to account for several equipment conditions and sampling methods as noted by Youd et al (2001).

1.5.1.2 CPT Approach

The cone penetration index-test uses the value $(q_{c1N})_{cs}$, the clean sands cone penetration tip resistance normalized to approximately 100 kPa (1 atm), to assess $CRR_{7.5}$. Similar to the SPT test, the CPT assessment of $CRR_{7.5}$ is broken up into ranges: For $(q_{c1N})_{cs} < 50$:

$$CRR_{7.5} = 0.833\left[\frac{(q_{c1N})_{cs}}{1000}\right] + 0.05 \tag{1.31}$$

For $50 \leq (q_{c1N})_{cs} < 160$:

$$CRR_{7.5} = 93\left[\frac{(q_{c1N})_{cs}}{1000}\right]^3 + 0.08 \tag{1.32}$$

The clean-sand cone penetration resistance, $(q_{c1N})_{cs}$, is derived from the dimensionless normalized cone penetration resistance by applying a coefficient K_c, which is a correction factor for grain characteristics, such that $(q_{c1N})_{cs} = K_c q_{c1N}$. To solve for the value of the clean-sand cone penetration resistance we must first evaluate the dimensionless, normalized cone penetration resistance, q_{c1N}, from:

$$q_{c1N} = C_Q(q_c/P_a) \tag{1.33}$$

where q_c is the field test result for the cone penetration tip resistance at depth, z_d; P_a is one unit of atmospheric pressure (1 atm) in the same units as σ'_{vo}; and C_Q is a normalizing factor defined by:

$$C_Q = (P_a/\sigma'_{vo})^{n'} \tag{1.34}$$

where the value of n' is 1 for clays, 0.5 for sands and between 0.5 and 1 (typically 0.7) for silts. The CPT test also relies upon a soil behaviour type index, I_c, defined by:

$$I_c = [(3.47 - \log Q)^2 + (1.22 + \log f_r)^2]^{0.5} \tag{1.35}$$

where Q represents the normalized cone resistance and uses the same value n' as C_Q:

$$Q = [(q_c - \sigma_{vo})/P_a][P_a/\sigma'_{vo}]^{n'} \tag{1.36}$$

and f_r represents the normalized friction ratio:

$$f_r = [f_s/(q_c - \sigma_{vo})] \cdot 100\% \tag{1.37}$$

with f_s being the sleeve resistance recorded in the field CPT results.

Youd et al. (2001) procedurally evaluates the soil behavior type index, I_c, as follows:

1) Assume that the soil acts as a clay ($n' = 1$) and compute the values of Q and f_r.
2) Evaluate I_c. If $I_c > 2.6$ then the soil is considered to be too clay-ish to liquefy and the analysis of liquefaction potential is complete. If, however, $I_c < 2.6$ then proceed to the next step.

3) Re-evaluate Q assuming the soil behaves as a sand ($n' = 0.5$) and evaluate a new I_c. If the new value of $I_c < 2.6$, then the soil is now considered to be non-plastic and granular, and analysis of liquefaction potential is complete. In the case where the new $I_c > 2.6$, the soil sample is very likely a silt, and analysis proceeds to the next step.

4) Re-evaluate Q with a value of $n' = 0.7$ and evaluate the corresponding I_c value.

For all soils with a value of $I_c > 2.4$, it is recommended to consult other soil type determining tests for a second opinion. Once the value of I_c has been found, the coefficient K_c may be evaluated to relate $(q_{c1N})_{cs}$ and q_{c1N} based upon the following relationship:

For $I_c \leq 1.64$, $\quad K_c = 1.0$

For $I_c > 1.64$, $\quad K_c = -0.403I_c^4 + 5.581I_c^3 - 21.63I_c^2 + 33.75I_c - 17.88$

1.5.1.3 V_S Approach

The shear-wave velocity approach is a newer test for liquefaction potential and less widely used than the SPT and CPT tests. One factor of note is that both V_S and $CRR_{7.5}$ are influenced by the void ratio, effective confining stress (stress induced by the weight of the overlying material), stress history, and geological age of a site (Youd et al., 2001). However, V_S readings have an advantage in their capability of capturing information at sites where the SPT and CPT tests are unable to penetrate the soil profile. Evaluation of $CRR_{7.5}$ using the shear-wave velocity approach is based upon the relationship:

$$CRR_{7.5} = 0.022\left(\frac{V_{S_1}}{100}\right)^2 + 2.8\left(\frac{1}{V_{S_1}^* - V_{S_1}} - \frac{1}{V_{S_1}^*}\right) \tag{1.38}$$

where V_{S_1} is the overburden-stress corrected shear wave velocity defined by:

$$V_{S_1} = V_S\left(\frac{P_a}{\sigma'_{vo}}\right)^{0.25} \tag{1.39}$$

and $V_{S_1}^*$ is the limiting upper value of for liquefaction occurrence, assumed linearly dependent on fines content (200 at $f_c = 35\%$, 215 at $f_c \leq 5\%$). At an earthquake magnitude of 7.5 and $V_{S_1} = 100$, this approach is found to be consistent with the CPT and SPT curves for evaluating $CRR_{7.5}$.

1.5.1.4 BPT Approach

Despite the widespread use of the SPT and CPT, both have limitations. The Becker penetration test (BPT) was designed to surmount the limitation caused by large diameter soil and rock particles (Youd et al. 2001). According to the discussion within the liquefaction workshops presented by Youd et al. (2001), evaluation of liquefaction through the BPT approach was based upon the blow count to drive a casing 300 mm into the ground, N_{BC}, and then related to an equivalent $(N_1)_{60}$ value based upon a figure presented in Youd et al. (2001). The equivalent $(N_1)_{60}$ value is then evaluated for the SPT index test as per equation (1.30).

1.5.1.5 Correction Factors

Numerous correction factors exist in the evaluation of $CRR_{7.5}$ based upon the test used, the methodology of the test, the equipment features (diameter, rod length, etc.), and the soil profiles. Correction factors are constantly undergoing development as more efficient sampling and analyzing techniques become available. As such, it is recommended that the reader seek out the most recently developed correction factors. Youd et al. (2001) lists numerous researchers who have worked upon these factors, and the work of Idriss and Boulanger (2006) and Boulanger and Idriss (2012) express one such set for the SPT index tests.

1.5.1.6 Additional Tests

As noted previously, there are times when evaluating a soil that the behavior is unclear, such as identifying the liquefaction potential of a silty soil. In such cases additional tests should be consulted (Youd et al., 2001). Traditionally, this consultation was done through examination of the soil properties via the so-called "Chinese criteria" presented by Seed and Idriss (1982), which was derived from the work of Wang (1979). Although the Chinese

criteria and its derivatives were heavily employed in liquefaction analysis, recent studies (Bray and Sancio, 2006; Idriss and Boulanger, 2006) have strongly urged for discontinued use of the Chinese criteria, instead preferring to identify liquefaction potential based upon the plasticity index (the difference in moisture/water content between when a soil acts like a liquid and when a soil acts as a plastic). Bray and Sancio (2006) performed a re-evaluation of the work of Wang (1979) and came to the following conclusions based upon the water content, w_c, liquid limit (the moisture content at which a soil behaves as a liquid), LL, and plasticity index, PI:

- A soil may be susceptible to liquefaction if $w_c/LL > 0.85$ and $PI < 12$
- Soils that do not meet these conditions but have $PI < 18$ and $w_c/LL > 0.8$ may be moderately susceptible to liquefaction; further laboratory tests should be performed
- Soils with $PI > 18$ will not liquefy at low effective stresses. However, structures founded on these soils may undergo significant deformations if the dynamic strength of the soil is exceeded by cyclic loading during a seismic event

1.5.2 Probabilistic Approaches

Probabilistic approaches to liquefaction analysis are a newer development. Juang et al. (2002) developed a probabilistic analysis using both logistic regression and Bayesian mapping. Logistic regression is an established statistical method used in the analysis of datasets, whereas Bayesian mapping applies Bayes' Theorem to evaluate the probability of an event occurring. Later, the work of Cetin et al. (2004) and Boulanger and Idriss (2012) led to the development of a performance based model for assessing liquefaction potential, outlined in GeoCongress 2013 by Franke and Wright (2013). The following sections briefly outline the work of Juang et al. (2002) and the research that led to Franke and Wright's performance based model.

1.5.2.1 *Logistic Regression and Bayesian Mapping Approaches*

Juang et al. (2002) developed two approaches for the generation of probabilistic liquefaction assessment curves. The developed curves are akin to those of the empirical approaches (plotting CSR against the relevant index statistic), are applicable to the SPT, CPT, and V_S approaches, and rely on the clean sands approximation. The logistic regression curve for the SPT approach is defined by:

$$\ln[P_L/(1-P_L)] = 10.1129 - 0.2572 \cdot (N_1)_{60,cs} + 3.4825 \cdot \ln(CSR_{7.5}) \tag{1.40}$$

furthermore the CPT curve is defined by:

$$\ln[P_L/(1-P_L)] = 12.4259 - 0.0498 \cdot (q_{c1N})_{cs} + 3.9887 \cdot \ln(CSR_{7.5}) \tag{1.41}$$

and the shear-wave velocity curve is defined by:

$$\ln[P_L/(1-P_L)] = 14.8967 - 0.0611 \cdot V_{S_1,cs} + 2.6418 \cdot \ln(CSR_{7.5}) \tag{1.42}$$

where P_L is the probability of liquefaction. Based upon this approach, selecting a given P_L value allows for the generation of a curve.

Alternatively, the Bayesian mapping approach solves for P_L as a function of the deterministic factor of safety in the form:

$$P_L = 1/[1 + (F/B_1)^{B_2}] \tag{1.43}$$

where F is the static deterministic factor of safety, and B_1 and B_2 are regression coefficients. The regression coefficients in equation (1.43) vary depending upon the in-situ test being examined; for the SPT approach, $B_1 = 0.8$ and $B_2 = 3.5$; for the CPT approach, $B_1 = 1.0$ and $B_2 = 3.3$; for the shear-wave approach, $B_1 = 0.73$ and $B_2 = 3.4$. Comparison of the Bayesian mapping to logistic regression performed by Juang et al. (2002) showed that the Bayesian mapping curves are more conservative than the logistic regression curves. A qualitative table which classifies the probability of liquefaction based upon the likelihood of the event triggering is presented by Juang et al. (2002).

1.5.2.2 *The Performance Based Model*

The performance based model is largely based upon an expansion of the SPT test mentioned in the previous section. Cetin et al. (2004) defined the probability of liquefaction, P_L, as:

$$P_L = \Phi\left(\frac{\left((N_1)_{60}\cdot(1+0.004\cdot f_c)-13.32\ln(CSR_{eq})-29.53\cdot\ln(M)-3.70\cdot\left(\frac{\sigma'_{vo}}{P_a}\right)+0.05\cdot f_c+16.85\right)}{-2.70}\right) \quad (1.44)$$

where CSR_{eq} is the uncorrected cyclic stress ratio (correction occurs in equation 1.44); M is the earthquake magnitude; and f_c is the fines content.

Cetin et al. (2004) also calculated the CRR value for a given probability of liquefaction, P_L, and earthquake magnitude, M, by inverting equation (1.44):

$$CRR = \exp\left(\frac{\left((N_1)_{60}\cdot(1+0.004\cdot f_c)-29.53\cdot\ln(M)-3.70\cdot\left(\frac{\sigma'_{vo}}{P_a}\right)+0.05\cdot f_c+16.85+2.7\cdot\Phi^{-1}(P_L)\right)}{13.32}\right) \quad (1.45)$$

However, the accuracy of the model developed by Cetin et al. (2004) has come under question after inconsistencies were noticed in its source database. Boulanger and Idriss (2012), were among those who noticed the discrepancies and proposed the following alternative expressions for equations (1.44) and (1.45):

$$P_L = \Phi\left(-\frac{\frac{(N_1)_{60,cs}}{14.1}+\left[\frac{(N_1)_{60,cs}}{126}\right]^2-\left[\frac{(N_1)_{60,cs}}{23.6}\right]^3+\left[\frac{(N_1)_{60,cs}}{25.4}\right]^4-2.67-\ln(CSR_{7.5})}{\sigma_{\ln(CRR_{7.5})}}\right) \quad (1.46)$$

$$CRR_{7.5} = \exp\left(\frac{(N_1)_{60,cs}}{14.1}+\left[\frac{(N_1)_{60,cs}}{126}\right]^2-\left[\frac{(N_1)_{60,cs}}{23.6}\right]^3+\left[\frac{(N_1)_{60,cs}}{25.4}\right]^4-2.67+\sigma_{\ln(CRR_{7.5})}\cdot\Phi^{-1}(P_L)\right) \quad (1.47)$$

where $\sigma_{\ln(CRR_{7.5})}$ is the standard deviation in the error of the natural logarithm of $CRR_{7.5}$.

Franke and Wright (2013) incorporated the Boulanger and Idriss (2012) approach into a performance based model to solve for the probability that the factor of safety against liquefaction, F_L, does not exceed a set level, F_L^*, according to:

$$P[F_L < F_L^*] = \Phi\left(\frac{\frac{(N_1)_{60,cs}}{14.1}+\left[\frac{(N_1)_{60,cs}}{126}\right]^2-\left[\frac{(N_1)_{60,cs}}{23.6}\right]^3+\left[\frac{(N_1)_{60,cs}}{25.4}\right]^4-2.67-\ln\left((F_L^*)\cdot CSR_{7.5}\right)}{-\sigma_\varepsilon}\right) \quad (1.48)$$

where σ_ε is the model standard deviation with a value of 0.28 if taking account of parameter measurement/estimation uncertainty (i.e. for $(N_1)_{60cs}$), and 0.13 if not.

1.6 ORGANIZATION OF THESIS

This thesis concentrates on the influence of the spatial variability of soil on slopes subjected to seismic loading, and develops a reliability-based design against seismic slope failure. As such, the approach to seismic slope analysis taken in this study shall seek to extend the pseudo-static methodology for examining seismic loading into probabilistic analysis using the RFEM approach to modeling spatial variability within soils. The following chapters shall investigate the relationship between the deterministic factor of safety and the probability of failure, in a manner similar to the approach taken by Javankhoshdel and Bathurst (2014). The intention of such an analysis is to create useful tools which geotechnical engineers may use as a reference for the safe evaluation and design of slopes.

In Chapter 2, the addition of an equivalent horizontal force to the RSLOPE2D program created by Griffiths and Fenton (2000, 2004) is used to model seismic behavior, as per the pseudo-static approach. The accuracy of the newly introduced seismic component is validated through comparison with existing studies. Results are compiled into deterministic seismic slope stability design charts which plot stability factor, λ, against the critical seismic

coefficient, k_c, which is a representation of the seismic load as a fraction of gravity, g. Chapter 3 introduces random field modeling to the seismic slope problem. A parametric study is performed through Monte Carlo simulation which focuses on the influence of spatial variability in the soil strength parameters. Results are compiled into probabilistic seismic slope stability design charts that plot the slope angle, β, against both the pseudo-static factor of safety, F_s, and the probability of failure, p_f.

Chapter 4 illustrates how the stability charts developed in Chapters 2 and 3 may be used within a reliability-based design framework. An example slope subjected to seismic loading is assessed both deterministically and probabilistically and the resulting pseudo-static factor of safety and probability of failure are compared to each other. The extent of failure, should it occur, is discussed.

Conclusions and suggested future work are presented in Chapter 5.

CHAPTER 2

DETERMINISTIC SEISMIC ANALYSIS OF $c - \phi$ SLOPES

2.1 GENERAL

Based upon the pseudo-static analysis method, the RSLOPE2D model developed by Griffiths and Fenton (2000, 2004) was modified to include a single constant, destabilizing (acting in the direction of slope failure) horizontal force representative of seismic acceleration, according to equations (1.16) and (1.17). Also required was the addition of the seismic coefficient, k, as an input parameter in the RSLOPE2D model. The final program, now modified to handle seismic accelerations for a 2-D slope mass, was renamed RSLOPE2A.

To begin examining the seismic stability of slopes with spatial variability, it was important to first confirm that RSLOPE2A was capable of capturing the effects of seismic loading. Validation of RSLOPE2A was performed by conducting a rigorous series of deterministic analyses and comparing to existing studies (Leschinsky and San, 1994; Michalowski, 2002; Loukidis et al., 2003; Baker et al., 2006). The parameters used in the validation study are shown in Table 2.1.

Table 2.1 Input parameters used in the validation of RSLOPE2A

Parameters	Values Considered
Slope angle, β	$10° \rightarrow 85°$
Mean friction angle, μ_ϕ	$10°, 15°, 20°, 25°, 30°, 35°, 40°$
Mean cohesion, μ_c	determined by λ
Stability factor, λ	$0 \rightarrow 1$
Seismic coefficient, k	$0 \rightarrow 1$ (g's)
Poisson's ratio, ν	0.3
Young's Modulus, E	10^5 kN/m^2
Unit weight, γ	18 kN/m^3
Height, H	5 m
Depth factor, D	2

The parameters selected in Table 2.1 correspond to those used in other in stability charts appearing in the literature, both static and pseudo-static. For example:

1) slope angle, β, values were those used in Leschinsky and San (1994) and Javankhoshdel and Bathurst (2014),

2) mean friction angle, μ_ϕ, values for the deterministic analysis were those used in Loukidis et al. (2003) and Baker et al. (2006),

3) mean cohesion, μ_c, values were based upon equation (1.21), which solved for μ_c gives:

$$\mu_c = \lambda \gamma H \tan \mu_\phi \tag{2.1}$$

As noted by Loukidis et al. (2003), λ normalizes the data based upon the ratio $\mu_c/\gamma H$. Since γ and H are held constant, the value of μ_c used, for any combination of μ_ϕ and λ, is derived solely from equation (2.1). This sometimes resulted in the use of unrealistic cohesion values, which may be ignored due to normalization,

4) the range of stability factor, λ, values was based upon the works of Loukidis et al. (2003) and Javankhoshdel and Bathurst (2014), where the case of $\lambda > 1$ only occurred for the $\mu_\phi = 10°$ case,

5) selection of the range of seismic coefficient values considered in this work agreed with Loukidis et al. (2003),

6) the constant soil parameters, Poisson's ratio, ν, and Young's Modulus, E, are not commonly used in slope stability analyses. The values shown in Table 2.1 are the nominal values suggested by Griffiths and Lane (1999),

7) the unit weight of soil, γ, is set to be the value used in the design examples of Baker et al. (2006). Michalowski (2002) and Javankhoshdel and Bathurst (2014) used a value of $\gamma = 17$ kN/m^3 and Loukidis et al. (2003) used a value of $\gamma = 20$ kN/m^3, so the value selected in Table 2.1 is in reasonable agreement with all of these authors,

8) the depth factor, D, is in agreement with that used by Leschinsky and San (1994), Michalowski (2002), and Javankhoshdel and Bathurst (2014),

9) the pore water pressure, u_d, is neglected in this work to simplify the analysis.

The validation of RSLOPE2A proceeded through the following process for each combination of parameters:

1) A deterministic analysis, starting from the static case ($k = 0$) and progressing to increasing seismic activity, was performed by increasing the seismic coefficient, k, from 0 to $1g$, in $0.01g$ steps. k increased until the deterministic analysis indicated $F_s = 1$ using equation (1.15), at which point the slope was assumed to have failed.

2) The k value corresponding to the $F_s = 1$ condition was recorded as the critical seismic coefficient, k_c, for that particular combination of stability number, λ, friction angle, ϕ, and slope angle, β. At this value of k, the slope is in a state of limit equilibrium brought on by the pseudo-static seismic loading.

3) Values of the critical seismic coefficient were plotted against the stability factor values, for comparison with previous studies

2.2 VALIDATION OF RSLOPE2A

Critical seismic coefficients (k_c's) obtained from the steps described in the previous section were plotted against the stability factor, λ, to obtain stability charts such as the one displayed in Figure 2.1. The format of the stability chart in Figure 2.1 is modeled after the work of Loukidis et al. (2003), where for a particular slope angle, curves for the critical seismic coefficient are plotted for a variety of friction angles, ϕ (hereafter referred to as "ϕ-curves"). To determine the stability of a particular slope, one first calculates λ, based upon the soil strength characteristics, and then moves across the chart until intercepting a line drawn up from the seismic coefficient the slope is being subjected to; this point is then compared to the line corresponding to the friction angle, ϕ, of the slope. If the point at which λ meets k is above and/or to the left of the k_c "ϕ-curve", then the slope is considered stable under the seismic load ($F_s > 1$). However, if this point is to the right and/or below the k_c curve, the slope will fail with $F_s < 1$. The complete collection of "ϕ-curve" stability charts from this study may be found in Appendix B.1 for $\beta = 20°, 25°, 30°, 35°, 40°, 45°$ and $50°$.

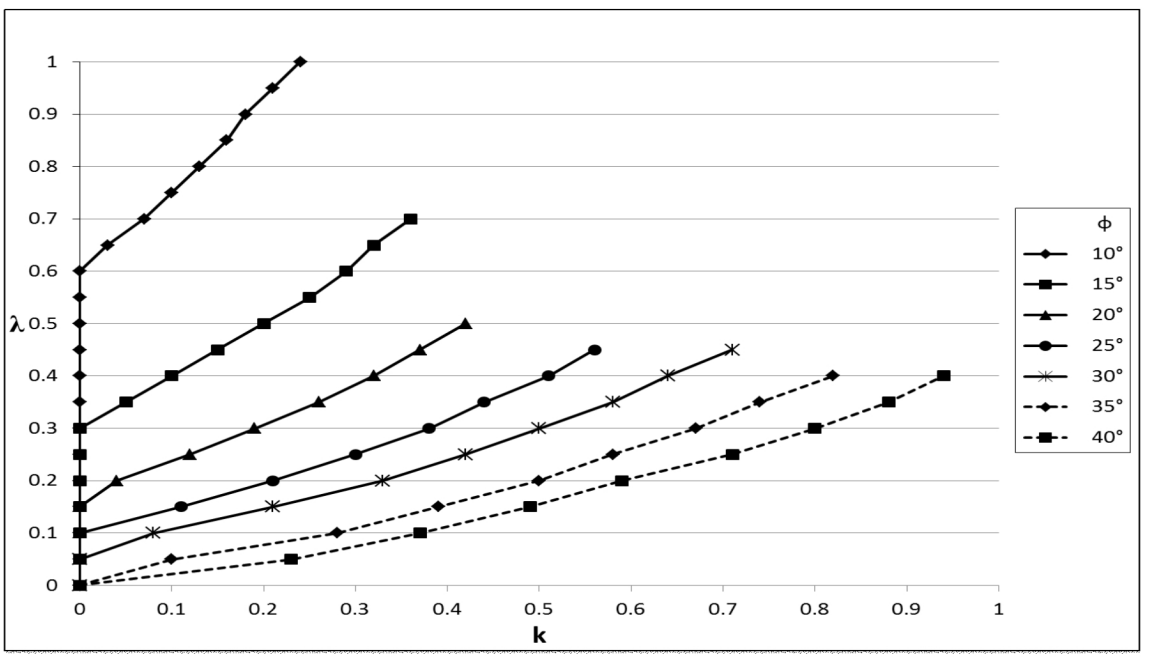

Figure 2.1 Critical seismic coefficients for a $\beta = 45°$ slope

Points of discontinuity are observed to occur at the end of the "ϕ-curves" in Figure 2.1. As discussed by Loukidis et al. (2003) these points correspond to the theoretical limit beyond which the entire slope is expected to move as a single mass sliding over its hard base (the hard layer). This block sliding occurs when k exceeds k_{lim}, where:

$$k_{lim} = \frac{\mu_c}{\gamma D H} + \tan \mu_\phi \tag{2.2}$$

Table 2.2 illustrates an example of the agreement between deterministic runs of RSLOPE2A and other studies. Figure 2.1 was compared to Figure 12 of Leschinsky and San (1994), the numerical lower bound curve of Figure 3c of Loukidis et al. (2003), and Figures 7c and 8a of Baker et. al (2006). It can be seen in Table 2.2 that the results of this work consistently reproduce values of existing studies.

Table 2.2 Comparison of k_c from Figure 2.1 with previous studies

λ	μ_ϕ	k_c			
		Figure 2.1	Leschinsky & San	Loukidis et al.	Baker et al.
0.10	25°	0.00	0.02	0.01	0.00
0.10	30°	0.14	0.15	0.15	0.14
0.10	40°	0.37	>0.25	0.39	0.40
0.20	25°	0.21	0.25	0.22	0.25
0.20	30°	0.36	>0.25	0.37	0.36
0.30	20°	0.19	0.20	0.20	0.20
0.35	15°	0.05	0.05	0.05	0.05
0.35	20°	0.26	>0.25	0.27	0.27
0.40	20°	0.32	>0.25	>0.30	0.33
0.50	15°	0.20	0.20	0.20	0.20
0.75	15°	0.37	>0.25	0.37	0.39
1.00	10°	0.24	0.25	0.24	0.25

2.3 ALTERNATIVE REPRESENTATION OF CHART DATA

Figure 2.2 presents an alternative representation of the data currently displayed in "ϕ-curves". The approach taken in Figure 2.2 was to exchange of the roles of β and μ_ϕ, generating "β-curves" for particular μ_ϕ values. An advantage of this representation is that k_{lim} (see equation 2.2), which is independent of β and dependent upon μ_ϕ, can be plotted as a curve alongside the "β-curves" for each μ_ϕ value. As before, points above and to the left of a curve indicate slope survival, $F_s > 1$, while those below and to the right indicate slope failure, $F_s < 1$. The full collection of "β-curve" stability charts obtained from this study may be found in Appendix B.2 for $\mu_\phi = 10°, 15°, 20°, 25°, 30°, 35°$ and $40°$ and for the full range of β values considered.

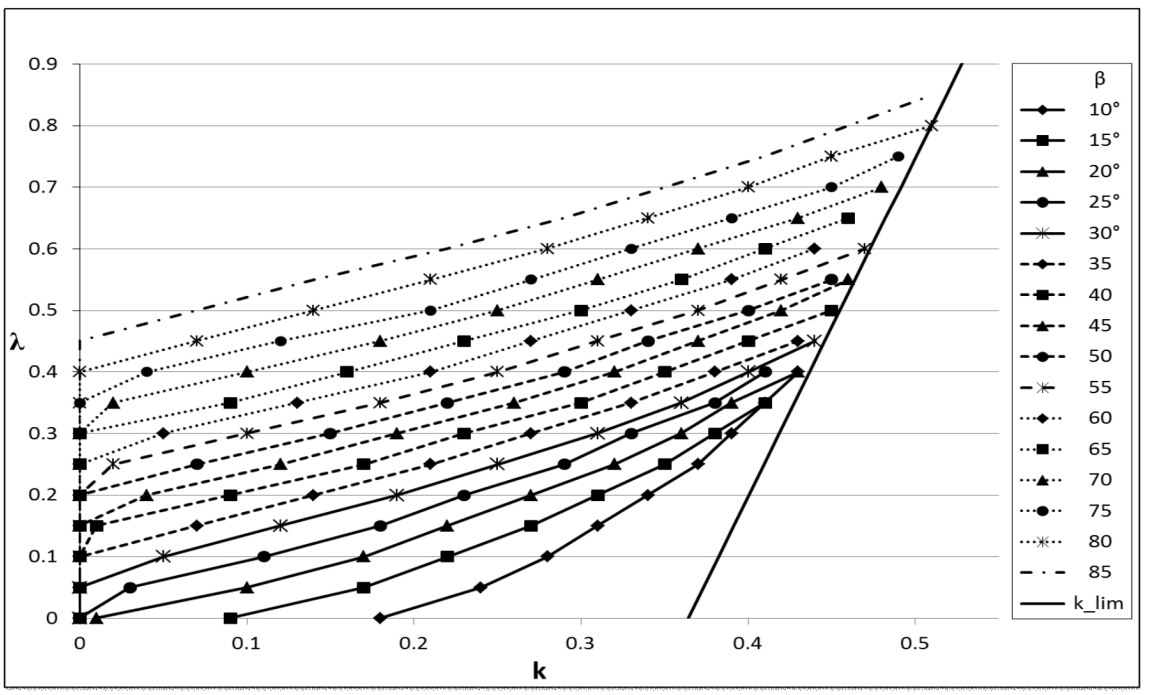

Figure 2.2 Critical seismic coefficients for slopes with $\mu_\phi = 20°$

2.4 DISCUSSION

The objective of this chapter was to ensure that RSLOPE2A was capable of handling the addition of seismic loading. The program was validated through comparison with existing pseudo-static slope stability studies. Examination of the results in Table 2.2 indicates that the RSLOPE2A program consistently predicts critical seismic coefficients which agree with those found in the literature. This agreement extends to the other β values examined and suggests that the finite element analysis in RSLOPE2A is evaluating the seismic loading correctly. The results were assembled into two sets of slope stability design charts (see Appendix B). The first set of design charts is based upon the "ϕ-curves" commonly found in the literature, and the second set is based upon the proposed alternative "β-curves". Having confirmed that the deterministic seismic component is working, and with the knowledge that the probabilistic component of RSLOPE2A, inherited from RSLOPE2D, has been validated for static slope stability before (Griffiths and Fenton, (2004); Griffiths et al., (2009)) the pseudo-static approach was deemed ready to extend into probabilistic analysis.

CHAPTER 3

PROBABILISTIC SEISMIC ANALYSIS OF $c - \phi$ SLOPES

3.1 GENERAL

The objective of this chapter is to develop design charts through a parametric study over a series of correlation lengths, θ, to examine the probability of failure, p_f, of cohesive-frictional ($c - \phi$) slopes subjected to various degrees of seismic loading. This analysis is similar to that of Javankhoshdel and Bathurst (2014) in providing a link between the traditional factor of safety approach and probabilistic slope analyses. The generation of design charts presented here was done through Monte Carlo simulations based upon the parameters shown in Table 3.1. Simulations proceed by generating many realizations of the spatially variable slope and observing the proportion of these realizations which fail ($F_s < 1$). In practice, the accuracy of this approach depends upon how well the simulated soil fields represent possible real slopes. Considering that the simulation component of RSLOPE2A has been tested rigorously for static slopes using Monte Carlo simulations (Griffiths and Fenton, 2004, Griffiths et al., 2009), the interest here is in capturing the seismic effects upon the probability of slope failure. In brief, 2000 Monte Carlo simulations are run for each combination of the parameters outlined in Table 3.1, with a varying number of soil finite elements (dependent upon β) each of size $0.1H$, and treating both the cohesion, c, and the tangent of the friction angle, $\tan\phi$, as lognormally distributed random fields. The probability of failure is then estimated by dividing the number of realizations which failed by the total number of realizations.

Table 3.1 Input parameters used in the parametric study

Parameters	Values Considered
Slope angle, β	$10° \rightarrow 85°$
Mean friction angle, μ_ϕ	20 °
Mean cohesion, μ_c	determined by λ
Coefficient of variation, $v_c = v_{tan\phi} = v$	0.1, 0.2, 0.3
Stability factor, λ	0.1, 0.2, 0.3, 0.4, 0.5
Seismic coefficient, k	0, 0.1, 0.2, 0.3 (g's)
Poisson's ratio, ν	0.3
Young's Modulus, E	10^5 kN/m^2
Unit weight, γ	18 kN/m^3
Height, H	5 m
Depth factor, D	2
Correlation, θ/H	0.1, 0.2, 0.3, 0.5, 0.7, 1, 2, 3, 5, 7, 10

The parameters outlined in Table 3.1 are the same as those used for the deterministic analysis in Chapter 2 with the addition of the spatial variability parameters v and θ. The slope angles, constant soil parameters, height, and depth factor remain the same as those in the previous analysis. Furthermore, pore water pressure, u_d, remains ignored. Selection of the parameter values that have been changed and added are detailed as follows:

1) Only one mean friction angle, μ_ϕ, was selected here for analysis. This was to allow the investigation to focus on the effects of the spatial variability of soils subject to seismic loading. Typical μ_ϕ values examined in study of $c - \phi$ soils range from $0°$-$40°$. A reasonable intermediate value was selected here.

2) Determination of the mean cohesion, μ_c, values was again based upon solving equation 2.1 for the particular λ values chosen in Table 3.1.

3) The stability factor, λ, values were based upon the selection of the seismic coefficient, k, values. The k values were chosen to represent the static case, as well as three sample seismic loads, within the typical restrictions set upon pseudo-static analysis ($k \leq 0.3$). λ values were selected to cover slopes which have some likelihood of failing.

4) Selection of the coefficients of variation, v, was roughly based upon the work of Phoon and Kulhawy (1999) who suggest v_c values between 0.1 and 0.5 and v_ϕ values between 0.1 and 0.2. In this study, the two separate values of coefficients of variation were taken to be equal with $v_c = v_\phi = v$ between 0.1 and 0.3. It should also be noted that the v associated with the friction angle in this study is actually for the distribution of $\tan\phi$. Further, since Phoon and Kulhawy (1999) suggest $v_\gamma < 0.1$, γ is assumed deterministic and is held constant at the same value selected in Chapter 2.

7) The correlation length, θ, which defines the spatial correlation structure of the soil, is varied over a range to investigate whether a "worst-case" correlation length exists. The "worst-case" correlation length would possess the highest slope failure probability.

3.2 RESULTS

Probabilistic seismic design charts were generated based upon the parametric study described in the previous section. These charts were modeled after Figure 12 of Javankhoshdel and Bathurst (2014), but modified by plotting β rather than μ_ϕ against both deterministic factor of safety (on the left y-axis) and probability of failure (on the right y-axis).

3.2.1 Effects of λ, k, and v

For each correlation length, θ, four probabilistic design charts were generated (one for each value of k considered). In each chart are a collection of twenty curves, five associated with the deterministic factor of safety (1 per λ value), and fifteen probability curves (3 per λ corresponding to the 3 v values). To eliminate sampling jitter, the probability curves are smoothed using logistic growth curves. Figures 3.1 to 3.4 display the probabilistic design charts for $\theta = 0.2H$. For given values of β and $\lambda_i = i/10$, where $i = 1, 2, 3, 4, 5$ these charts provide the deterministic factor of safety and the failure probabilities, p_f, for v = 0.1, 0.2, and 0.3. The full collection of design charts can be found in Appendix C.

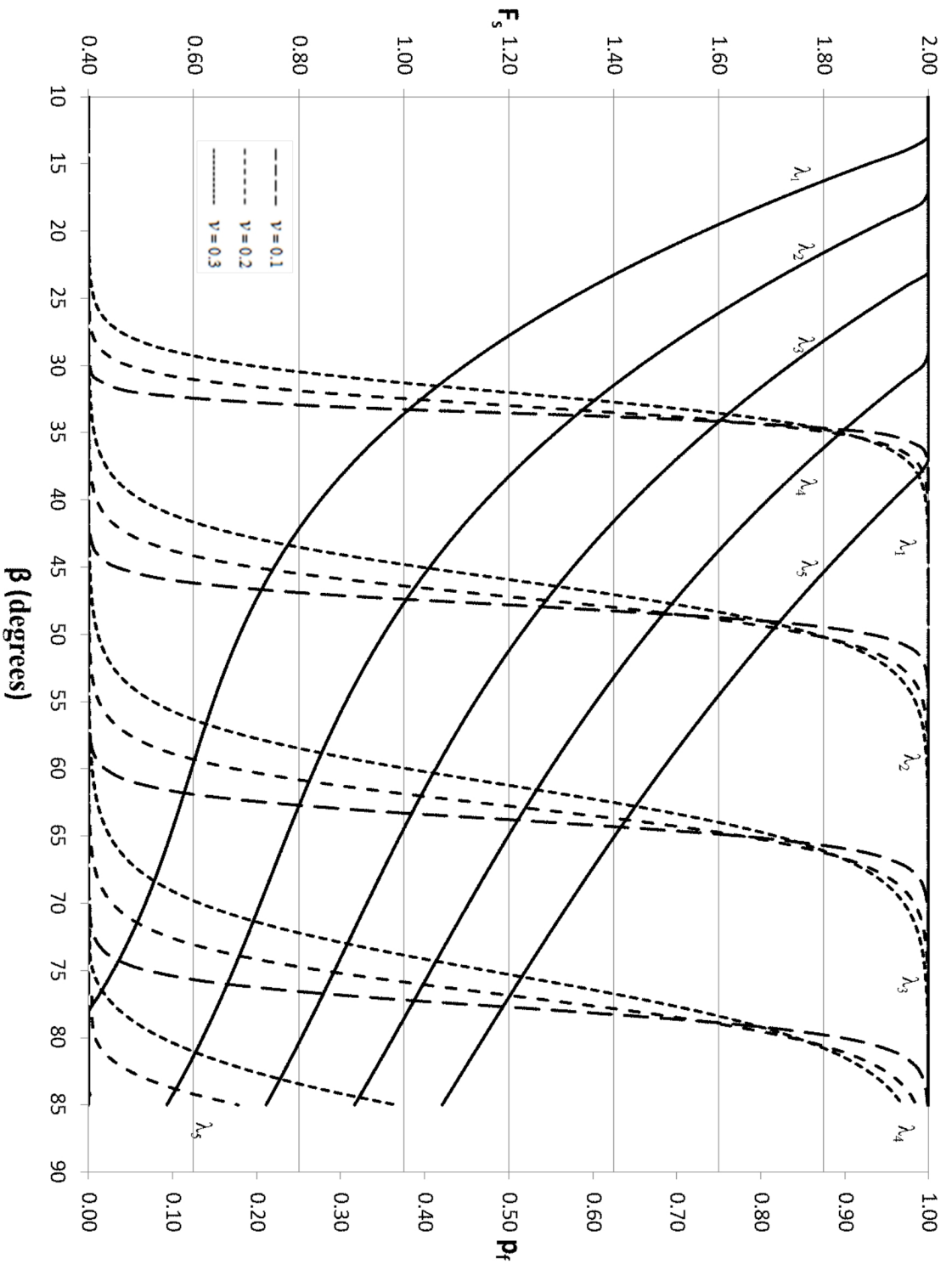

Figure 3.1 Probabilistic pseudo-static slope stability design chart for $\mu_\phi = 20°$, $k = 0, \theta = 0.2H$. Solid lines plot F_s. $\lambda_i = i/10$

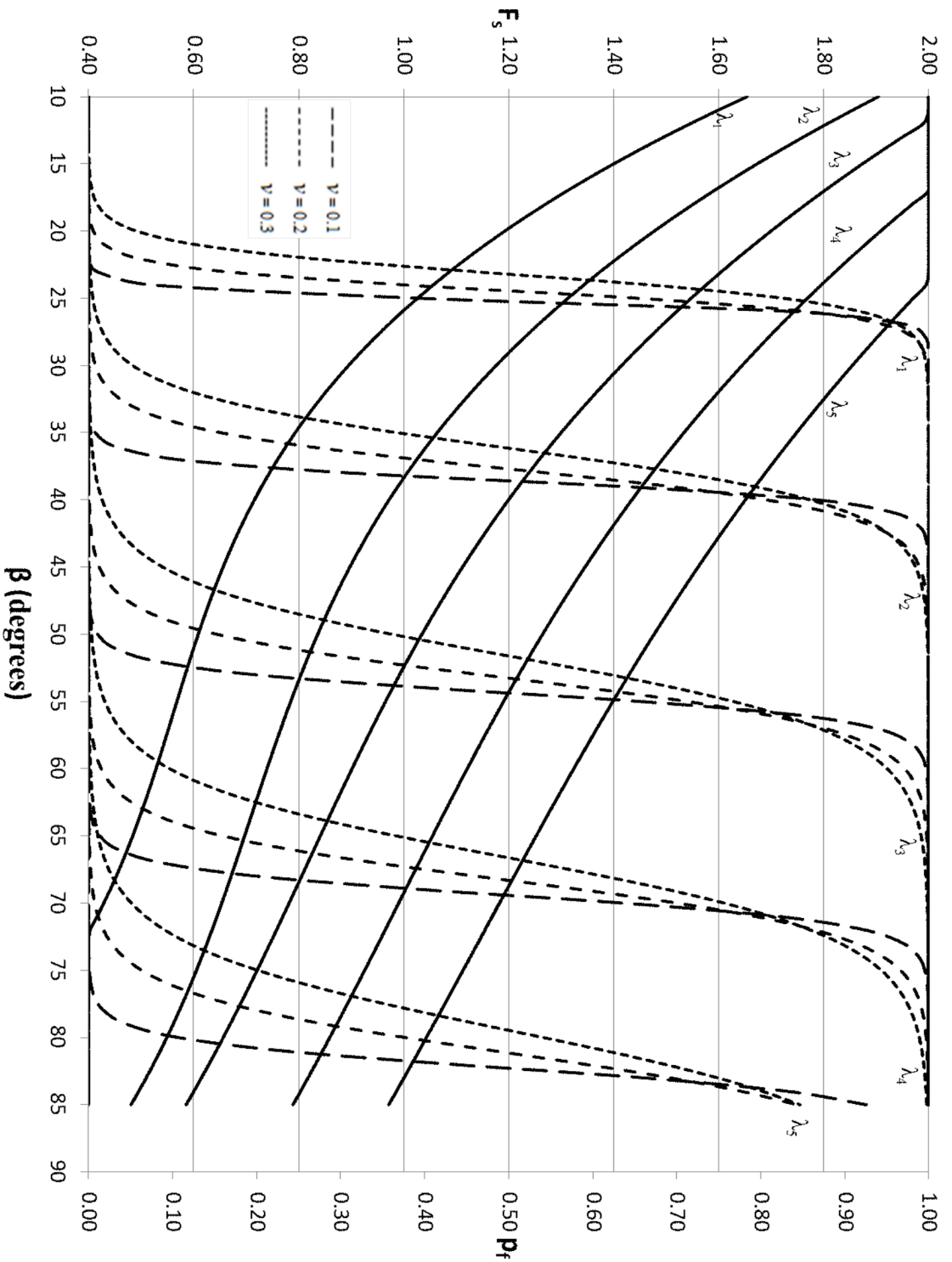

Figure 3.2 Probabilistic pseudo-static slope stability design chart for $\mu_\phi = 20°$, $k = 0.1g$, $\theta = 0.2H$. Solid lines plot F_s. $\lambda_i = i/10$

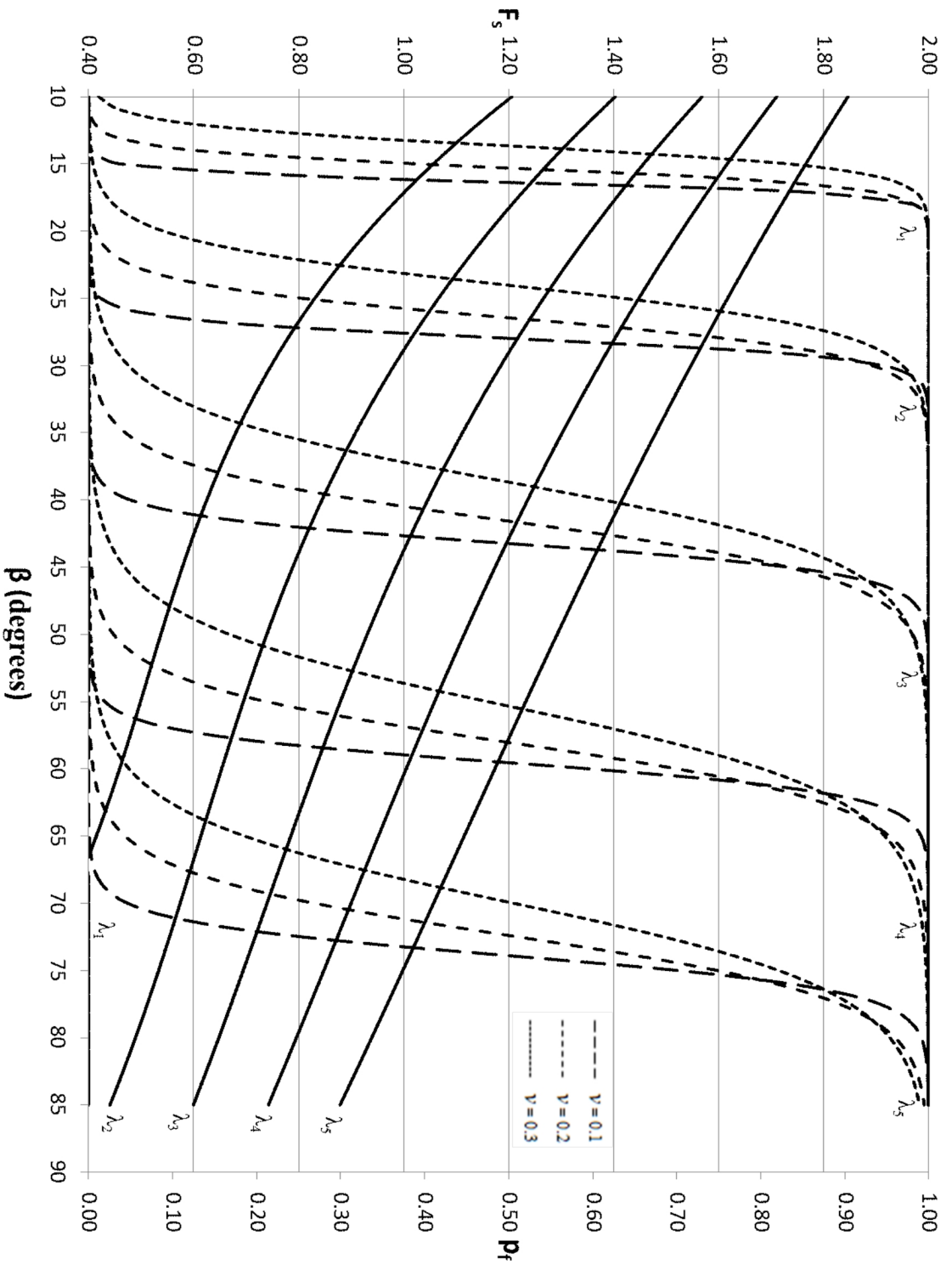

Figure 3.3 Probabilistic pseudo-static slope stability design chart for $\mu_\phi = 20°$, $k = 0.2g$, $\theta = 0.2H$. Solid lines plot F_s. $\lambda_i = i/10$

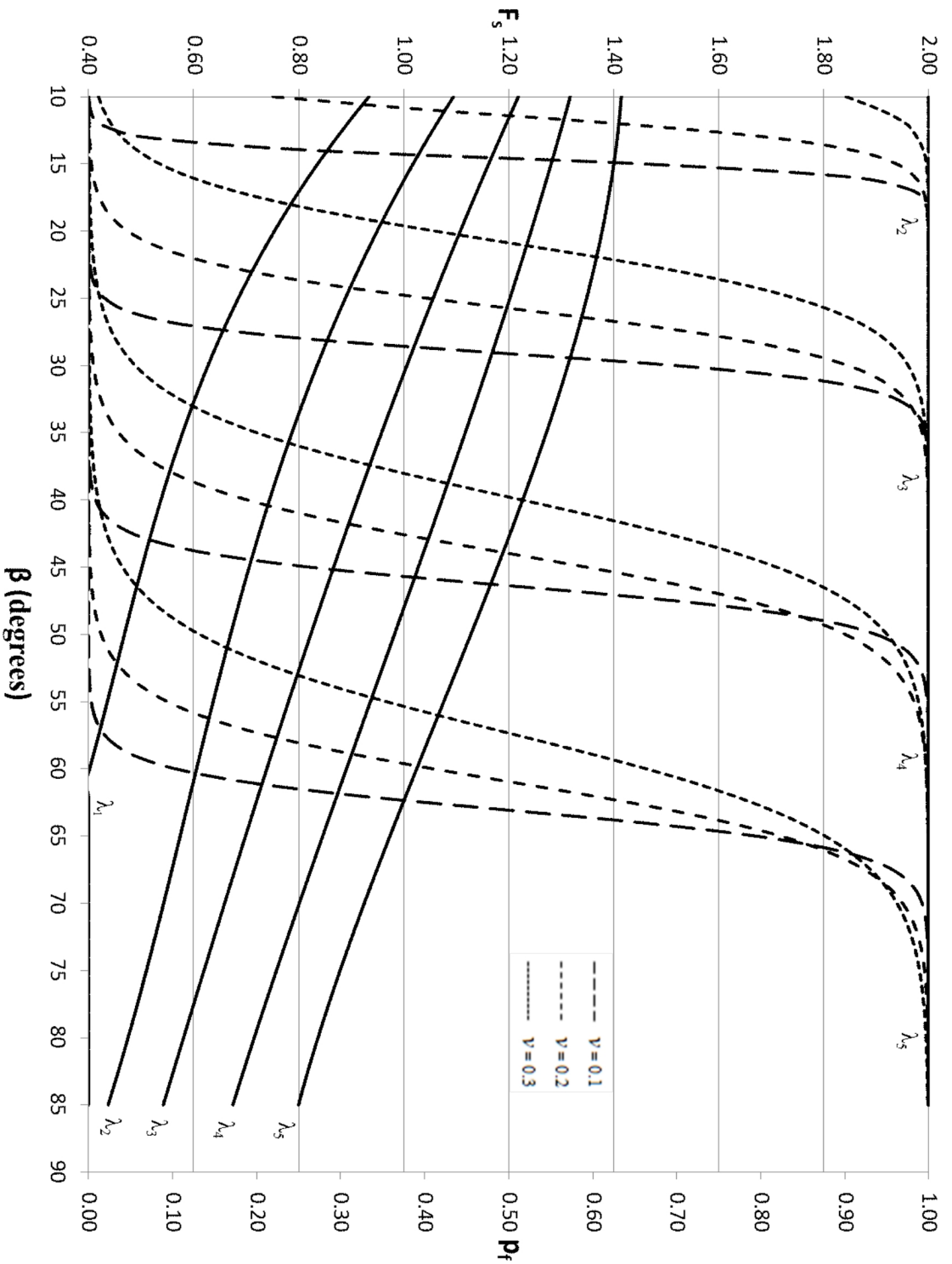

Figure 3.4 Probabilistic pseudo-static slope stability design chart for $\mu_\phi = 20°$, $k = 0.3g$, $\theta = 0.2H$. Solid lines plot F_s. $\lambda_i = i/10$

Clearly visible in Figures 3.1 to 3.4 are the effects of both the stability number, λ, and the seismic coefficient, k, which have opposing roles in the slope stability problem. As λ increases, the probability of failure for a particular slope angle, β goes down. This is visible when examining the different values of λ present on a particular plot; from left to right, increases in λ are observed to shift the probability of failure curve to higher β values, which means an increase in slope stability and a decreased risk of failure. This makes sense, since for fixed friction angle an increase in λ implies an increase in mean cohesive strength. Alternatively, when increasing k from one chart to another, all of the λ curves are observed to shift to lower β values, which is consistent with the expected loss of stability, and thus increased risk of failure brought on by increased seismic loading. Similarly, the deterministic factor of safety is observed to increase for increasing λ and reduce as k is increased.

Also observed in Figures 3.1 to 3.4 are the effects of the coefficient of variation, v. Increasing values of v were observed to broaden the range of β values over which there is a risk of failure. The increase in probability of failure at lower slope angles, and decrease at higher slope angles is due to the increased variability, which creates more regions of weaker and stronger soils, during the Monte Carlo realizations. At low slope angles, the broadening β range provides conservative estimates of slope stability, as the increased likelihood of weaker soil being present in the slope requires lower slope angles for the slope to remain stable. The broadening at higher β values may be ignored since geotechnical engineers are interested in small p_f in design.

3.2.2 Effects of θ

In the previous section, Figures 3.1 to 3.4 presented a set of probabilistic seismic design charts for one of the θ values indicated in Table 3.1. For each value of θ the entire probabilistic analysis was repeated, producing additional sets of charts. The use of any particular set of charts is dependent upon the estimated correlation length for a particular slope site. To determine if there is a "worst-case" θ value, associated with the highest amount of risk, Figure 3.5 plots a comparison of low, medium, and high correlation length values against the $\theta \to \infty$ case (the latter of which represents the SRV approach described in Chapter 1).

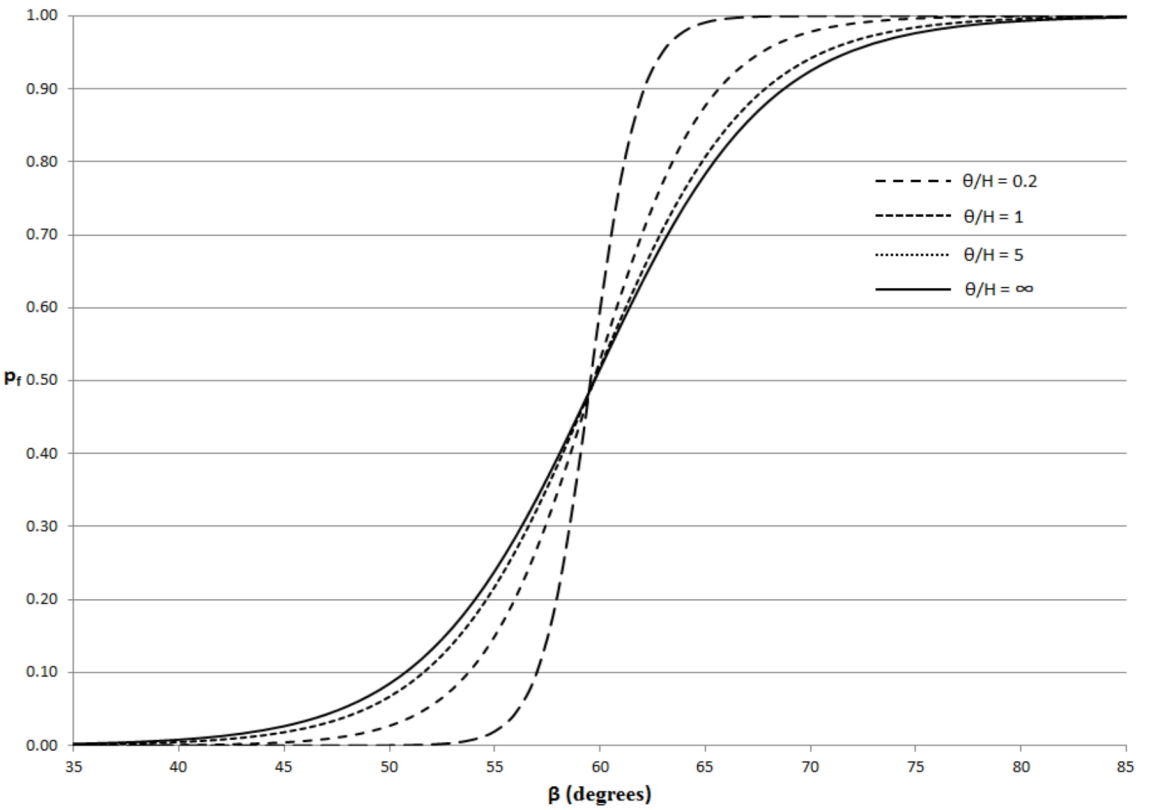

Figure 3.5 Influence of correlation length on the probability of slope failure for $\mu_\phi = 20°$, $k = 0.2g$, $\lambda = 0.4$, $v = 0.1$

Observed in Figure 3.5 is the broadening of the range of β values which experience a risk of failure as θ increases, resulting in the $\theta \rightarrow \infty$ case exhibiting the highest slope failure probability at lower slope angles which is thus the most conservative case. However, the $\theta \rightarrow \infty$ case yields a Monte Carlo simulation where each realization is a different homogeneous slope with constant soil strength parameters throughout, which is not realistic. As the focus of this work is in the effects of spatial variability, the $\theta \rightarrow \infty$ case is not particularly interesting, and design should attempt to use reasonable values for θ. The $\theta = 10H$ case adequately approximates the $\theta \rightarrow \infty$ case, and the plots in Appendix C corresponding to $\theta = 10H$ may be used as conservative estimates of the SRV ($\theta \rightarrow \infty$) approach.

3.3 DISCUSSION

The RSLOPE2A program was used to conduct a parametric study over a series of correlation lengths to examine the probability of failure of a cohesive-frictional slope subjected to various degrees of seismic loading. Monte Carlo simulations were conducted for a single mean friction angle, $\mu_\phi = 20°$, and for slope angles ranging from $10°$ to $85°$ over a broad range of correlation lengths. All simulations assumed non-liquefiable soils, and ignored ground water effects. The results of this study were assembled into design charts (see Appendix C) which compare the deterministic factor of safety to the probability of failure for each slope angle over a variety of seismic loadings, stability factors, and coefficients of variation. Included in the analysis was the static ($k = 0$) slope problem, which recovered known results from previous RFEM studies (Griffiths and Fenton, 2004, Griffiths et al., 2009), for comparison to the effects of seismic loading.

When compared to the deterministic analysis of Chapter 2, the results of the probabilistic pseudo-static slope stability design charts identify the inability of traditional factor of

safety measures to fully capture the margin of safety of a particular slope. Nominally, this discrepancy is observed when two slopes with identical factors of safety but different combinations of soil strength parameters exhibit significantly different probabilities of slope failure. This imperfect quantification of slope stability through use of the factor of safety rather than probabilities of failure has also been observed by Javankhoshdel and Bathurst (2014) in their extension of static slope stability design charts into probabilistic analysis for cohesive (ϕ = 0) and cohesive-frictional ($c - \phi$) soils using the SRV approach. The static (k = 0, $\theta = 10H \rightarrow \infty$ in Appendix C) results within this work, reproduce the results of Javankhoshdel and Bathurst (2014) for the case v = 0.1. Again, the probabilities of failure presented by Javankhoshdel and Bathurst (2014) and the $\theta \rightarrow \infty$ case described in this study lead to overly conservative estimates of the probability of slope failure, as they do not account for realistic spatial variability in the soil strength parameters. Griffiths and Fenton (2000) compared the use of the SRV approach to RFEM analysis and found that, for $0.1 \leq v_c \leq 0.5$, the single random variable approach was more conservative, while the opposite was found to be true for larger v_c values. It is therefore not surprising that the SRV approach is more conservative than the RFEM approach in the production of the probabilistic pseudo-static slope stability design charts in this work, as the selection of v values does not exceed a value of 0.3.

The design charts in Appendix C offer a means to estimate the effects of realistic, spatially varying soil properties, and irregular failure paths. These charts may be useful for geotechnical engineers for slope design purposes, both in conjunction with the work of Javankhoshdel and Bathurst (2014) (when k = 0), and as an expansion upon existing deterministic pseudo-static slope stability design charts (when $k > 0$). Practical application of the developed probabilistic pseudo-static design charts in slope stability analysis is discussed in the following chapter.

CHAPTER 4

PROPOSED ANALYSIS PROCEDURE

4.1 EXISTING SLOPE DESIGN APPROACHES

In general, existing seismic design approaches are predominately pseudo-static in nature due to the high computational cost of fully dynamic models. Often the choice of methodology is determined case by case, depending upon the complexity of the problem. For simplified homogeneous slope masses existing seismic slope stability charts may be used, such as those presented by Leschinsky and San (1994) and Loukidis et al. (2003), provided the slope in question adheres to a few key assumptions:

1) Slopes must be comprised of soils which are not expected to experience liquefaction. Determination of the liquefaction potential of soils may be conducted using the empirical relationships described in section 1.5.

2) Effects of pore water pressure are not important (u_d = 0). This means that pseudo-static slope stability design charts are best used when the ground water table is low.

3) Seismic coefficients used in pseudo-static design analysis are limited such that $k \leq 0.3g$ (Hynes-Griffin and Franklin, 1984; Baker et al., 2006).

4) The static factor of safety of the slope being examined is in the range of $1.0 \leq F \leq 1.7$ (Hynes-Griffin and Franklin, 1984).

For a slope which satisfies the above conditions, geographical hazard maps are used to determine the strongest seismic coefficient, k, that a slope within a particular region is

expected to experience. Soil samples taken from the site may be analyzed to determine estimates of the soil strength parameters μ_c, μ_ϕ, and γ. Measurements can be taken to determine the approximate slope angle (β) and height (H), and borings made to estimate the depth to the hard layer (DH). Based upon the soil strength parameters evaluated through sampling, the stability factor, λ, (or stability number, N) is calculated. The seismic coefficients obtained from the hazard maps are then compared to the critical seismic coefficient, k_c, obtained from the pseudo-static stability charts for the particular λ, β, and μ_ϕ values to determine whether the slope remains stable under the expected seismic loading ($k < k_c$ indicates $F_s \geq 1$). Newmarkian approaches (see equation 1.24) can then also be applied to determine the expected displacement when the stability charts indicate unstable slopes ($k > k_c$).

As an example, consider a slope having the parameters outlined in Table 4.1 that is expected to experience a seismic event with k = 0.2. Evaluation of the seismic slope stability, using the pseudo-static slope stability design charts derived in this study proceeds as follows:

Table 4.1 Input parameters for an example slope subjected to seismic loading

Parameters	**Values Considered**
Slope angle, β	55 °
Mean friction angle, μ_ϕ	20 °
Mean cohesion, μ_c	13 kN/m^2
Poisson's ratio, ν	0.3
Young's Modulus, E	10^5 kN/m^2
Unit weight, γ	18 kN/m^3
Height, H	5 m
Depth to hard layer	10 m

1) The depth factor, D, is simply taken as the depth to the hard layer divided by the height of the slope, D = 10m/5m = 2. The stability factor, λ, is determined from equation (1.21):

$$\lambda = \frac{\mu_c}{\gamma H \tan \mu_\phi} = \frac{13 \text{ kN/m}^2}{\left(18 \text{ kN/m}^3\right)(5 \text{ m})(\tan 20^\circ)} \approx 0.4$$

2) The deterministic factor of safety curve of Figure 3.1 (k = 0, or static loading) for $\lambda = 0.4$ and $\beta = 55^\circ$ was used to determine a static factor of safety of $F = 1.37$ for the example slope described in Table 4.1. This factor of safety indicates a statically stable slope, but one which falls within the range that should undergo pseudo-static analysis according to Hynes-Griffin and Franklin (1984).

3) Since $\mu_\phi = 20^\circ$, the deterministic pseudo-static slope stability chart in Figure 2.2 is consulted to determine if the slope remains stable under the seismic load. For $\beta = 55^\circ$, a slope with $\lambda = 0.4$ has $k_c \approx 0.25$. Since $k_c > k$ the slope is considered to be stable by the pseudo-static analysis.

The above example illustrates a typical deterministic pseudo-static stability analysis. However, this analysis assumes a deterministic (homogeneous) slope mass which in practice does not occur. Further, consideration of the spatial variability of the soil strength, evident in real-world slopes, provides further insight into the stability of cohesive-frictional slopes along with the ability to actually estimate failure probability. The addition of spatial variability parameters to the example above is discussed in the next section.

4.2 RELIABILITY-BASED SLOPE DESIGN

As an investigation of the effects of spatially varying soil strength parameters, let c and $\tan\phi$ be random fields having lognormal distributions with means μ_c and $\mu_{\tan\phi}$, standard deviations σ_c and $\sigma_{\tan\phi}$, and correlation length θ. Suppose that $\theta_{\ln c} \approx \theta_{\ln \tan\phi} \approx 0.2H$. Based upon these assumptions, Figure 4.1 displays a modified version of Figure 3.3, which pertains to slopes with $\theta = 0.2H$, $\mu_\phi = 20°$, and $k = 0.2$, and displays only the curves having $\lambda = 0.4$.

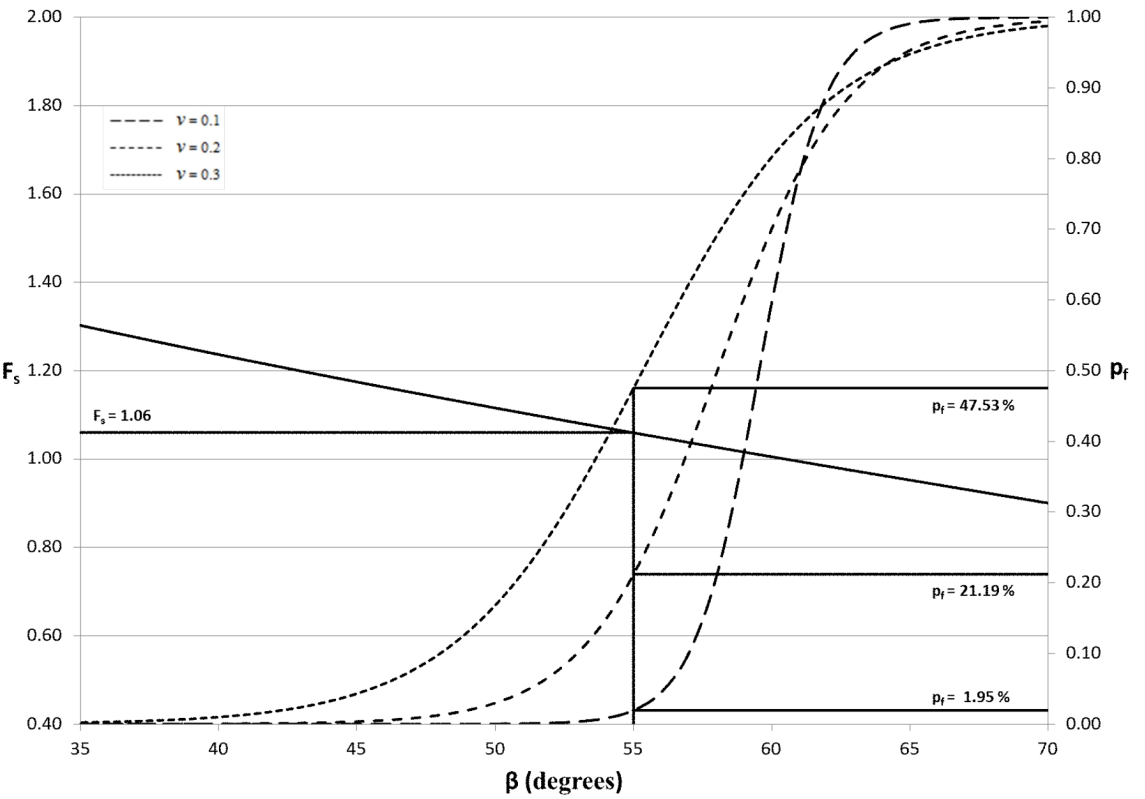

Figure 4.1 Evaluation of the seismic slope stability of the existing slope

For the example slope, Figure 4.1 shows $F_s = 1.06$, which agrees with the deterministic pseudo-static analysis of the previous section and suggests the slope survives ($F_s > 1$). However, the probability of slope failure ranges from about 2% to 48% for v ranging from

0.1 to 0.3. Probabilities of failure of such magnitude are typically unacceptable, except perhaps where the failure of the slope would have no significant consequences. In many cases, this example slope would be considered too unsafe and have to be remediated by excavating to a shallower slope angle, if this is an existing slope, or using a stronger fill material, if this is a constructed slope. Reduction of the probability of failure by means of reducing the slope angle is illustrated in Figure 4.2. Slopes angles of $50°$, $45°$, and $40°$ (with static factor of safety $F = 1.46$, 1.57, and 1.69 respectively) might be suggested as the remediated slope angle if $v = 0.3$. If geotechnical engineers are targeting the probability of failure to $p_f \leq 1\%$, remediation would require that the slope angle be reduced to $\beta \leq 40°$.

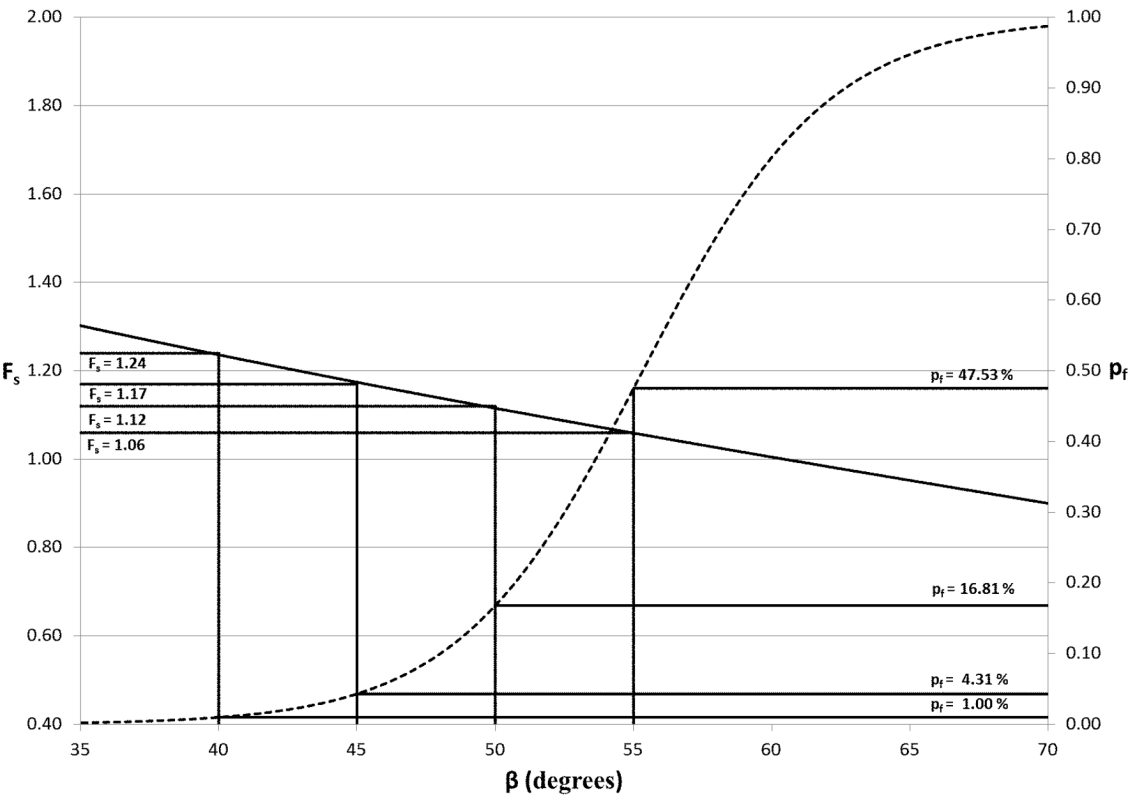

Figure 4.2 Evaluation of seismic slope stability of alternative slope angles for the example problem for $v = 0.3$

4.3 COMPARISON TO THE SRV APPROACH

Suppose that, instead of using the estimate of the correlation length provided in the previous section, the described slope was investigated through use of the SRV approach ($\theta \to \infty$). In this study, the condition that $\theta \to \infty$ was roughly approximated by the $\theta = 10H$ case. Figure 4.3 displays the deterministic factor of safety and the probabilities of failure of the same slope angles ($55°$, $50°$, $45°$, and $40°$) displayed in Figure 4.2.

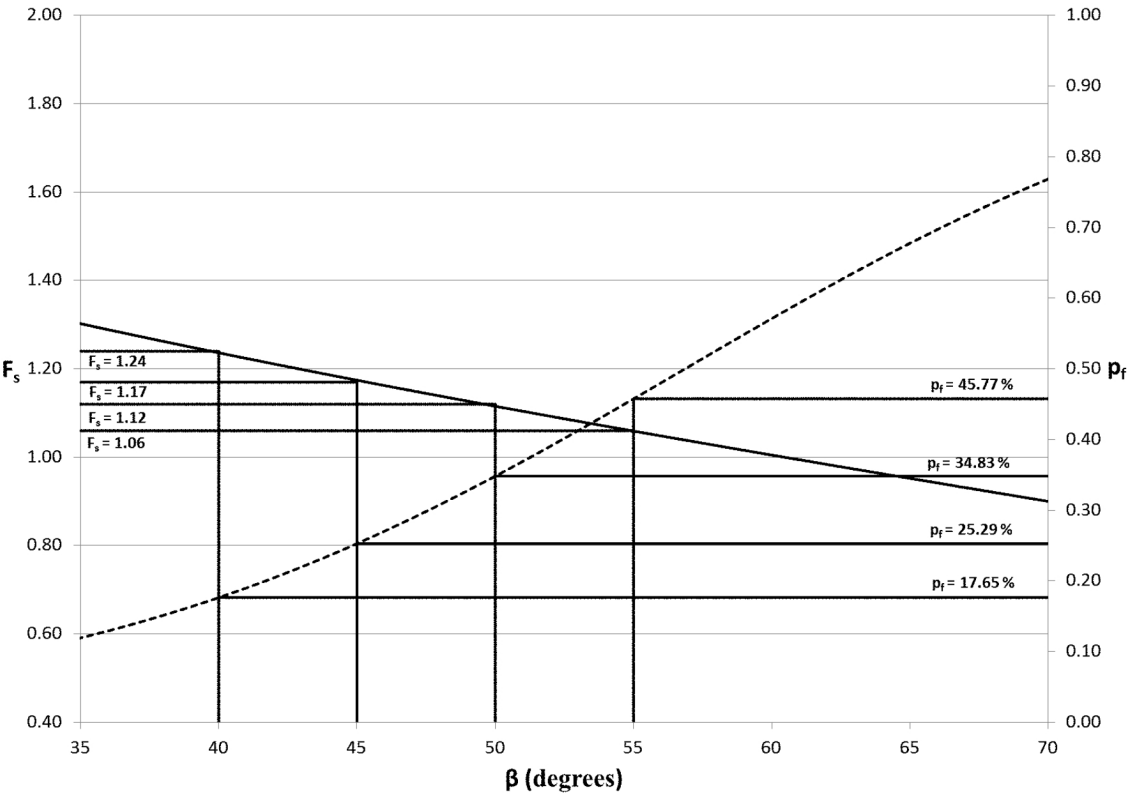

Figure 4.3 Reconsideration of Figure 4.2 for the $\theta \to \infty$ case

Clearly seen in Figure 4.3 is the general increase in the probabilities of failure caused by the increase in θ, while the deterministic pseudo-static factor of safety, F_s, remains unchanged. F_s remains unchanged due to its independence from the correlation measure, θ, as F_s is evaluated at the mean values of the soil strength parameters (thereby neglecting spatial

variability). A comparison of the probabilities of failure from the previously considered $\theta = 0.2H$ case to those of the $\theta \to \infty$ approach is shown in Table 4.2 for $v = 0.3$. Table 4.2 shows that p_f, for the considered slope angles, is initially less for the SRV approach when $\beta = 55°$, however p_f also remains significantly higher for the SRV case than for the $\theta = 0.2H$ case as β is reduced. Since geotechnical engineers seek to minimize p_f, the SRV approach may be viewed as an overly conservative estimate of the probability of slope failure.

Table 4.2 Probabilities of slope failure for the example slope with $v = 0.3$ when $\theta = 0.2H$ and $\theta \to \infty$

β	p_f (%)	
(degrees)	$\theta = 0.2H$	$\theta \to \infty$
55	47.53	45.77
50	16.81	34.80
45	4.31	25.25
40	1.00	17.60

4.4 EVALUATING THE EXTENT OF FAILURE

Current means for estimating the extent of failure of a slope subject to seismic loading is predominately based on Newmarkian sliding block analysis. As an expansion upon the pseudo-static method, Newmarkian models evaluate the displacement of the slope mass when the seismic acceleration exceeds the critical acceleration for the slope ($k > k_c$). For example, the probabilistic seismic hazard analysis equations presented by Rathje and Saygili (2009, 2011), given by equations (1.24) and (1.25), examine the displacement when $k > k_c$ through the ratio k_c/k (k is used in place of PGA). Newmarkian models determine the displacement of the slope mass as if it were a block moving along a plane. Evaluation of the distribution of block displacement is more difficult. In the previous section, a $\beta = 55°$

slope was observed to have a probability of failure as high as 48%. The problem is that this probability of failure was for a slope having a deterministic factor of safety $F_s > 1$ since $k < k_c$. When $k < k_c$ the Newmarkian models cannot be used to determine the extent of slope failure, even though spatial variability indicates a significant probability that the slope mass will actually move. This restriction is a product of the spatial variability being analyzed, as each realization within a Monte Carlo simulation for a combination of soil strength parameters would possess its own F_s and k_c values that vary from the mean (deterministic) case. Without shifting to a dynamic analysis, a proposed method by which to evaluate the extent of failure for the probabilistic pseudo-static slope stability design charts is as follows:

1) For each realization within a single Monte Carlo simulation a critical seismic coefficient, k_c, for the realized slope mass can be estimated by varying the applied seismic coefficient, k, and finding the smallest value of which just causes slope failure. This k value is then k_c.

2) Once the series of k_c values are estimated for each realization, a series of realizations of block displacements, using Newmarkian methods, can be determined, from which a displacement distribution may be estimated.

3) The displacement realizations could also be directly used to determine the probability of exceeding a particular limit displacement.

Due to the computationally expensive nature of this task, requiring multiple finite element analyses for each realization, evaluation of the extent of failure of the slope masses was not feasible in this study.

4.5 DISCUSSION

The objective of this chapter was to illustrate the practical application of the pseudo-static slope stability design charts developed in Chapters 2 and 3. The "β-curve" plots developed in Chapter 2 used in conjunction with the probabilistic design charts developed in Chapter 3 allow for the consideration of the spatial variability of soil strength parameters and the probability of slope failure under seismic loading. The results of the presented example show that the SRV approach is overly conservative. It is advisable to estimate the correlation length and consult the probabilistic pseudo-static slope stability design charts developed herein to obtain safe and economical slope designs in earthquake prone regions.

CHAPTER 5

CONCLUSIONS

In this work, the stability of cohesive-frictional ($c - \phi$) slopes subjected to seismic loading was investigated using a finite element model combined with random-field generation techniques to examine the influence of spatial variability of soil strength parameters. The approach used is called the random finite element method (RFEM). This study built upon the RSLOPE2D program developed by Griffiths and Fenton (2004). Both deterministic and probabilistic seismic slope analyses were performed to generate stability charts, and the deterministic charts were validated through comparison with existing studies. The stability charts were then used to develop a reliability-based procedure for the safe design of slopes. The validation conducted in Chapter 2 ensured that the RSLOPE2A program (created through the addition of a pseudo-static seismic component to the RSLOPE2D program) agreed with previous studies which utilized pseudo-static analysis. Both traditional "ϕ-curve" and alternative "β-curve" representations of the pseudo-static seismic stability charts were presented. The complete collection of deterministic seismic stability design charts can be found in Appendix B.

In Chapter 3, the RSLOPE2A program was used to conduct a parametric study over a series of correlation length values to examine the probability of failure of a cohesive-frictional ($c - \phi$) slope subjected to various degrees of seismic loading. Monte Carlo simulations were conducted for a single mean friction angle, $\mu_\phi = 20°$, with slope angles ranging from $10°$ to $85°$. The results of this study were assembled into design charts which give the deterministic factor of safety and the probability of failure for each slope angle

at particular seismic loadings, represented by the seismic coefficient, k. The probabilistic seismic stability charts show the expected rapid loss in stability with increasing seismic loading, as well as with increasing slope angle, β, and decreasing stability factor, λ. Said probabilistic seismic stability charts illustrate the deterministic factor of safety and the probability of slope failure for varying degrees of spatial variability in the soil strength random fields, c and $\tan\phi$. The deterministic factor of safety was found to be an inadequate measure of slope stability when the spatial variability of soil was taken into account, due to the potential for high probabilities of slope failure to occur when the deterministic factor of safety indicates stability ($F_s > 1$). The complete collection of probabilistic seismic slope stability design charts can be found in Appendix C.

Finally, the application of the design charts developed in Chapters 2 and 3 was illustrated in Chapter 4 through a design example. The design example showed how the deterministic plots were first used to determine the need for further analysis, and allowed for an initial estimate of the seismic response of the slope. The probabilistic plots could then be used to provide further insight into the probabilistic response of the slope when variability in the soil properties was considered. The design charts were used to determine, for example, the maximum slope angle for a target maximum acceptable failure probability.

Further research would be recommended in the following areas;

a) Expansion of the analysis performed in Chapter 3 to additional friction angles, notably $\mu_\phi = 10°$ and $\mu_\phi = 30°$

b) Implementation of pore-water pressure, u_d, into a seismic slope analysis model

c) Consideration of the extent of failure after it occurs, as discussed in Chapter 4

d) Development of a computationally-efficient, fully dynamic analysis

REFERENCES

Baker, R. (2003). "A second look at Taylor's stability chart," *J. Geotech. Geoenv. Engng.*, **129**(12), 1102–1108.

Baker, R., Shukha, R., Operstein, V., and Frydman, S. (2006). "Stability charts for pseudo-static slope stability analysis," *Soil Dynamics and Earthquake Engineering*, **26**(9), 813-823.

Bishop, A.W. (1955). "The use of the slip circle in the stability analysis of slopes," *Geotechnique*, **5**(1), 7–17.

Boulanger, R.W. and Idriss, I.M. (2012). "Probabilistic standard penetration test-based liquefaction-triggering procedures," *J. Geotech. Geoenv. Engrg.*, **138**(10), 1185–1195.

Bray, J.D. (2007). "Simplified seismic slope displacement procedures,"*Earthquake Geotechnical Engineering*, **Chapter 14**, 327–353. K.D. Pitilakis, Ed., Springer.

Bray, J.D. and Sancio, R.B. (2006). "Assessment of the Liquefaction Susceptibility of Fine-Grained Soils," *J. Geotech. Geoenv. Engrg.*, **132**, 1165–1177.

Cetin, K.O., Seed, R.B., Kiureghian, A.D., Tokimatsu, K., Harder, L.F. Jr., Kayen, R.E., and Moss, R.E.S. (2004). "Standard Penetration Test-Based Probabilistic and Deterministic Assessment of Seismic Soil Liquefaction Potential,"*Journal of Geotechnical and Geoenvironmental Engineering*, **130**, 1314–1340.

Chen, W.F. (1975). *Limit analysis and soil plasticity*. Amsterdam: Elsevier.

Chugh A.K. (1983). "Slope stability analysis for earthquakes,"*International Journal for Numerical and Analytical Methods in Geomechanics*, **11**, 79–102 .

Coduto, D.P., Yeung, M.R., and Kitch, W.A (2011). *Geotechnical Engineering: Practices and Principles*,(2nd Edition), Prentice Hall, Upper Saddle River, NJ.

Cousins, B.F (1978). "Stability charts for simple earth slopes," *J. Geotech. Engng, ASCE* **104**(2), 267–279.

Duncan, J.M. (1996). "State of the art: limit equilibrium and finite element analysis of slopes," *J. Geotech. Engng. ASCE* **122**(7), 577–596.

Duncan, J.M. (2000). "Factors of safety and reliability in geotechnical engineering", *J. Geotech. Geoenv. Engng, ASCE*, **126**(4): 307–316.

Eurocode 8 (1993). "Structures in seismic regions – design. Part 5 – Foundations, retaining structures and geotechnical aspects."

Fellenius, W. (1936). "Calculation of the stability of earth dams," *Proc. 2nd congr. large dams, Washington DC* **4**.

Fenton, G.A., and Griffiths, D.V. (2008). "Risk assessment in geotechnical engineering." John Wiley & Sons, New York.

Fenton, G.A., and VanMarcke, E.H. (1990). "Simulation of random fields via local average subdivision," *J. Eng. Mech.*, **116**(8), 1733–1749.

Franke, K.W. and Wright, A.D. (2013). "An alternative performance-based liquefaction initiation procedure for the standard penetration test," *GeoCongress 2013: Stability and Performance of Slopes and Embankments III* , ASCE,San Deigo, 846–849.

Griffiths, D.V., and Fenton, G.A. (2000). "Influence of soil strength spatial variability of an undrained clay slope by finite elements," In *Slope Stability 2000*, Proceeding of GeoDenver 2000, pages 184–193. ASCE, 2000.

Griffiths, D.V., and Fenton, G.A. (2004). "Probabilistic slope stability analysis by finite elements," *J. Geotech. Geoenv. Engrg.*, **130**(5): 507–518.

Griffiths, D.V., Huang, J., and Fenton, G.A. (2009)."Influence of spatial variability on slope reliability using 2–D random fields," *J. Geotech. Genenv. Engrg.*, **135**(10): 1367–1378

Griffiths, D.V., and Lane, P.A. (1999). "Slope stability analysis by finite elements," *Geotechnique*, **49**(3): 387-403.

Harr, M.E. (1987). *Reliability based design in civil engineering*, McGraw Hill, London, New York.

Hynes-Griffin, M.E., and Franklin, A.G. (1984). "Rationalizing the seismic coefficient method," Miscellaneous paper GL-84-13 US Army Corps of Engineers. Waterways Experiment Station.

Idriss, I.M. and Boulanger, R.W. (2006). "Semi-empirical procedures for evaluating liquefaction potential during earthquakes,"*Soil Dynamics and Earthquake Engineering*, **26**, 115–130 .

IITK–GSDMA, Indian Institute of Technology Kampur – Gujarat State Disaster Management Authority (2005). "Guidelines for seismic design of earth dams and embankments: provisions with commentary and explanatory examples." National Information Center of Eathquake Engineering, Indian Instituite of Technology Kanpur.

Javankhoshdel, S., and Bathurst, R.J. (2014). "Simplified probabilistic slope stability design charts for cohesive and cohesive-frictional ($c-\phi$) soils," *Can. Geotech. J.*, **51**, 1033–1045.

Juang, C.H., Jiang, T. and Andrus, R.D. (2002). "Assessing probability-based methods for liquefaction potential evaluation,"*J. Geotech. Geoenv. Engrg.*, **128**, 580–589.

Leschinsky, D., and San, K. (1994). "Pseudostatic seismic stability of slopes: Design charts," *J. Geotech. Engrg*, **120**(9), 1514-1532.

Loukidis, D., Bandini, P. and Salgado, R. (2003). "Stability of seismically loaded slopes using limit analysis," *Geotechnique*, **53**(5), 463–479.

Makdisi, F. I. and Seed, H. B. (1978). "Simplified procedure for estimating dam and embankment earthquake induced deformations,"*J. Geotech. Eng. Div.*, **104**(GT7), 849–867.

Michalowski, R.L. (1995). "Slope tability analysis: a kinematical approach," *Geotechnique*, **45**(2), 283–293.

Michalowski, R.L. (2002). "Stability charts for uniform slopes," *J. Geotech. Geoenv. Engrg.*, **124**(4): 351-355.

Mostyn, G.R. and Small, J.C. (1987). "Methods of stability analysis,"*in: Walker, B.F., and Fell, R., (eds) Soil Slope Instability and Stabilization.*,A.A. Balkema, Sydney, Australia, 315–324.

Newmark, N.M. (1965). "Effects of earthquakes on dams and embankments,"*Geotechnique*, **15**(2), 139–160.

NZ Transport Agency (2013). "Earthquake induced liquefaction, slope instability and ground deformation," In *The NZ Transport Agency's Bridge Manual SP/M/022*, Third Edition, Amendment 0, p. 6-16–6-22.

Phoon, K.-K., and Kulhway, F.H. (1999). "Characterization of geotechnical variability," *Canadian Geotechnical Journal*, **36**(4), 612–624.

Rathje, E.M. and Saygili, G. (2008). "Probabilistic seismic hazard analysis for the sliding displacement of slopes: scalar and vector approaches,"*J. Geotech. Geoenv. Engrg.*, **136**(6), 804–814.

Rathje, E.M. and Saygili, G. (2009). "Probabilistic assessment of earthquake-induced sliding displacements of natural slopes,"*Bull. N. Z. Soc. Earthquake Eng.*, **42**, 18–27.

Rathje, E.M. and Saygili, G. (2011). "Estimating fully probabilistic seismic sliding displacements of slopes from a pseudoprobabilistic approach,"*J. Geotech. Geoenv. Engrg.*, **137**(3), 208–217.

Sarma, S.K. (1973). "Seismic stability of earth dams and embankments,"*Geotechnique*, **25**(4), 743–761.

Shumway, R.H., and Stoffer, D.S. (2011). "Time Series Analysis and its Applications: With R Examples. Third Edition". New York: Springer Science and Business Media

Smith, I.M., and Griffiths, D.V. (1988). "Programming the Finite Element Method". John Wiley and Sons, Chichester, New York, 2nd edition.

Smith, I.M., and Griffiths, D.V. (1998). "Programming the Finite Element Method". John Wiley and Sons, Chichester, New York, 3rd edition.

Spencer, E. (1967). "A method of analysis of the stability of embankments assuming parallel interslice forces," *Geotechnique* **17**(1), 11–26.

Steward, T., Sivakugan, N., Shukla, S.K, and Das, B.M. (2011). "Taylor's slope stability charts revisted," *International Jounal of Geomechanics*, **11**(4), 348–352.

Taylor, D.W. (1937). "Stability of earth slopes," *J. Boston Soc. Civ. Eng.* **24**, 197–246.

USACE, US Army Corps of Engineers (1989). "Engineering and design of retaining and flood walls," *EM 1110-2-2502*

VanMarcke, E.H. (1984). *Random field: Analysis and synthesis*, The MIT Press, Cambridge, Mass.

Youd, T.L, Idriss, I.M., Andrus, R.D., Arango, I., Castro, G., Christian, J.T., Dobry, R., Finn, W.D.L., Harder, L.F. Jr., Hynes, M.E., Ishihara, K., Koester, J.P., Liao, S.S.C., Marcuson, W.F. III, Martin, G.P., Mitchell, J.K., Moriwaki, Y., Power, M.S., Robertson, P.K., Seed, R.B., and Stokoe, K.H. II (2001). "Liquefaction resistance of soils: Summary report from the 1996 NCEER and 1998 NCEER/NSF workshops on evaluation of liquefaction resistance of soils.,"*J. Geotech. Geoenv. Engrg., ASCE;* **127**(10), 817–833.

Appendix A

Comparison of log-space and real-space correlation length

A.1 Introduction

A key parameter in modeling spatial variability of a random field is the correlation length,θ_x, which describes the distance within which points are significantly correlated (in exceedance of 10At times, it may be found that a random field is best characterized by a lognormal distribution but we wish to perform normal distribution based calculations; this can be achieved through use of the logarithm of the random field. What comes into question is whether the correlation length of the random field and its logarithm are interchangeable, or if a calculable relation between them exists.

A.2 Definition of the Correlation Structures

To begin relating log-space to real-space, let us first consider the correlation structure of a random field, X, with mean μ_x, and variance σ_x^2. If we assume the correlation function, $\rho_x(\underset{\sim}{\tau})$, is defined such that:

$$\rho_x(\underset{\sim}{\tau}) = \exp\left\{\frac{-2|\underset{\sim}{\tau}|}{\theta_x}\right\} \tag{A.1}$$

then this is an exponentially decaying correlation structure (Fenton and Griffiths, 2008), i.e.

$$\text{Cov}\left[X(\underset{\sim}{x}), X(\underset{\sim}{x}+\underset{\sim}{\tau})\right] = \sigma_x^2 \rho_x(\underset{\sim}{\tau}) = C_x(\underset{\sim}{\tau}) \tag{A.2}$$

where $\rho_x(\underset{\sim}{\tau})$ is parameterized by the correlation length, θ_x, and $C_x(\underset{\sim}{\tau})$ shall be the shorthand representation of the covariance function for this document.

If we further consider the case where X is lognormally distributed, then lnX is normally distributed with mean $\mu_{\ln x}$, and variance $\sigma_{\ln x}^2$. We may then rewrite equations (A.1) and (A.2) for the lognormal case such that:

$$\rho_{\ln x}(\underset{\sim}{\tau}) = \exp\left\{\frac{-2|\underset{\sim}{\tau}|}{\theta_{\ln x}}\right\} \tag{A.3}$$

and

$$\text{Cov}\left[\ln X(\underline{x}), \ln X(\underline{x}+\underline{\tau})\right] = \sigma^2_{\ln X}\rho_{\ln X}(\underline{\tau}) = C_{\ln X}(\underline{\tau}) \tag{A.4}$$

where, in accordance to the previous equations, $\rho_{\ln X}(\underline{\tau})$ is parameterized by the log-space correlation length, $\theta_{\ln X}$, and $C_{\ln X}(\underline{\tau})$ shall be the shorthand representation of the log-space covariance function for this document.

A.3 Relation Between the Log-space and Real-space Parameters

The log-space parameters $\mu_{\ln X}$ and $\sigma^2_{\ln X}$ can be obtained from the real-space parameters μ_X and σ^2_X based upon the following relationships:

$$\mu_{\ln X} = \ln(\mu_X) - \frac{1}{2}\sigma^2_{\ln X} \tag{A.5}$$

$$\sigma^2_{\ln X} = \ln\left(1 + \frac{\sigma^2_X}{\mu^2_X}\right) \tag{A.6}$$

which are derived by taking the expectation and variance of X (Fenton and Griffiths, 2008). Equation (A.6) may be simplified further by implementing another parameter, $v_X = \mu_X/\sigma_X$, known as the coefficient of variation of X, such that:

$$\sigma^2_{\ln X} = \ln\left(1 + v^2_X\right) \tag{A.7}$$

Finally, recalling that the log-space variance, $\sigma^2_{\ln X}$, is a special case of the log-space covariance structure occurring at $\tau = 0$ (Shumway and Stoffer, 2011), equation (A.6) can be generalized to exhibit a direct relation between the correlation structures:

$$C_{\ln X}(\underline{\tau}) = \ln\left(1 + \frac{C_X(\underline{\tau})}{\mu^2_X}\right) \tag{A.8}$$

A.4 Solving for the Log-space Correlation Length

A relationship between the real-space and log-space correlation lengths (θ_X and $\theta_{\ln X}$ respectively) can be derived by utilizing the relationship displayed in equation (A.8). Solving equation (A.4) for $\rho_{\ln X}(\tau)$ and substituting equations (A.8) and (A.7) for $C_{\ln X}(\tau)$ and $vlnX$ respectively, yields:

$$\rho_{\ln X}(\tau) = \frac{C_{\ln X}(\tau)}{\sigma^2_{\ln X}} = \frac{\ln\left(\frac{1+C_X(\tau)}{\mu_X^2}\right)}{\ln\left(1+v_X^2\right)} \qquad (A.9)$$

The log-space correlation structure displayed equation (A.9) can then be related to its real-space counterpart by substituting equation (A.2) for $C_X(\tau)$, and simplifying using v_X:

$$\rho_{\ln X}(\tau) = \ln\left(\frac{1+\rho_X(\tau)\sigma_X^2}{\mu_X^2}\right) / \ln\left(1+v_X^2\right) = \frac{\ln\left(1+v_X^2\rho_X(\tau)\right)}{\ln\left(1+v_X^2\right)} \qquad (A.10)$$

Having found the relationship between the correlation structures, we may now relate the log-space correlation structure and the real-space correlation length by substituting the identity for $\rho_X(\tau)$ in equation (A.1) into equation (A.10):

$$\rho_{\ln X}(\tau) = \frac{\ln\left(1+\frac{v_X^2\exp(-2|\tau|)}{\theta_X}\right)}{\ln\left(1+v_X^2\right)} \qquad (A.11)$$

We are now ready derive the relationship between θ_X and $\theta_{\ln X}$. Solving equation (A.3) in terms of $\theta_{\ln X}$ and substituting equation (A.11) for$\rho_{\ln X}(\tau)$ produces the following identity:

$$\theta_{\ln X} = \frac{-2|\tau|}{\ln\left(\ln\left(1+v_X^2\exp\left(-2|\tau|/\theta_X\right)/\ln\left(1+v_X^2\right)\right)\right)} \qquad (A.12)$$

A.5 Evaluating the Relationships Limits with Respect to v_x

For any given spacing τ and real-space correlation length θ_x, it can be seen that as the coefficient of variation approaches zero, first order Mercator series approximations ($\ln(1 + a) \approx a$, for small values of a) in the denominator express that $\theta_x \approx \theta_{\ln x}$:

$$\lim_{v_x \to 0} \frac{-2|\tau|}{\ln\left(\ln\left(1 + v_x^2 \exp\left(-2|\tau|/\theta_x\right)/\ln\left(1 + v_x^2\right)\right)\right)} = \frac{-2|\tau|}{\ln\left((\exp\left(-2|\tau|/\theta_x\right)\right)} = \theta_x \tag{A.13}$$

Appendix B

DETERMINISTIC SEISMIC SLOPE DESIGN CHARTS

B.1 Phi-curves

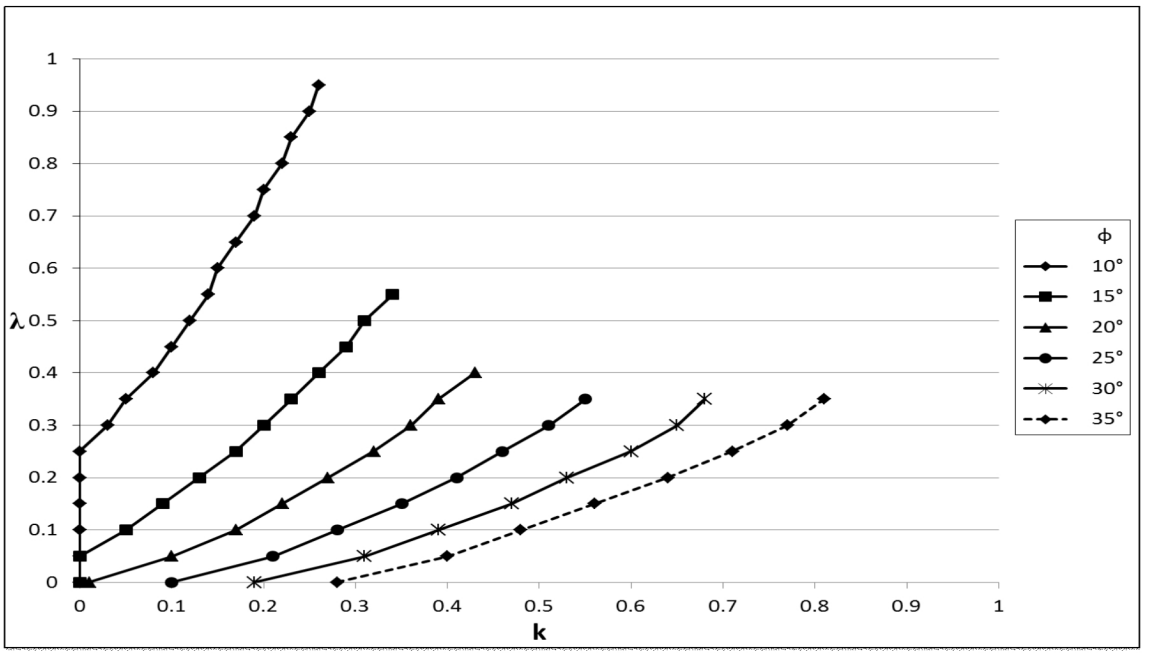

Figure B.1 Critical seismic coefficients for a 20° slope

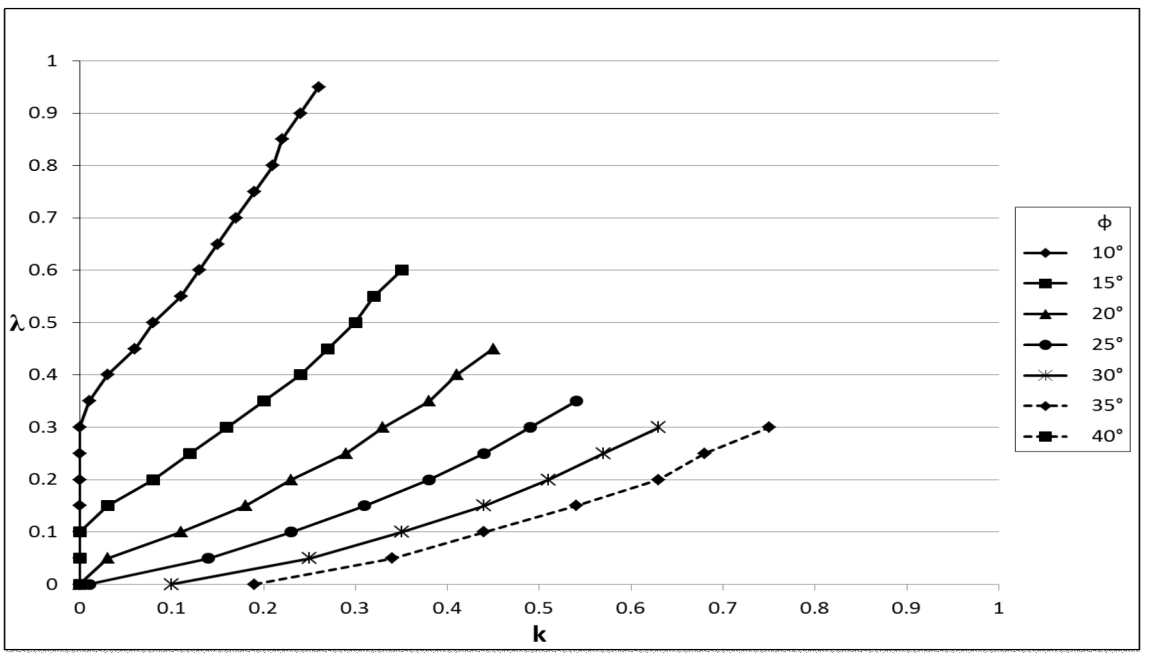

Figure B.2 Critical seismic coefficients for a 25° slope

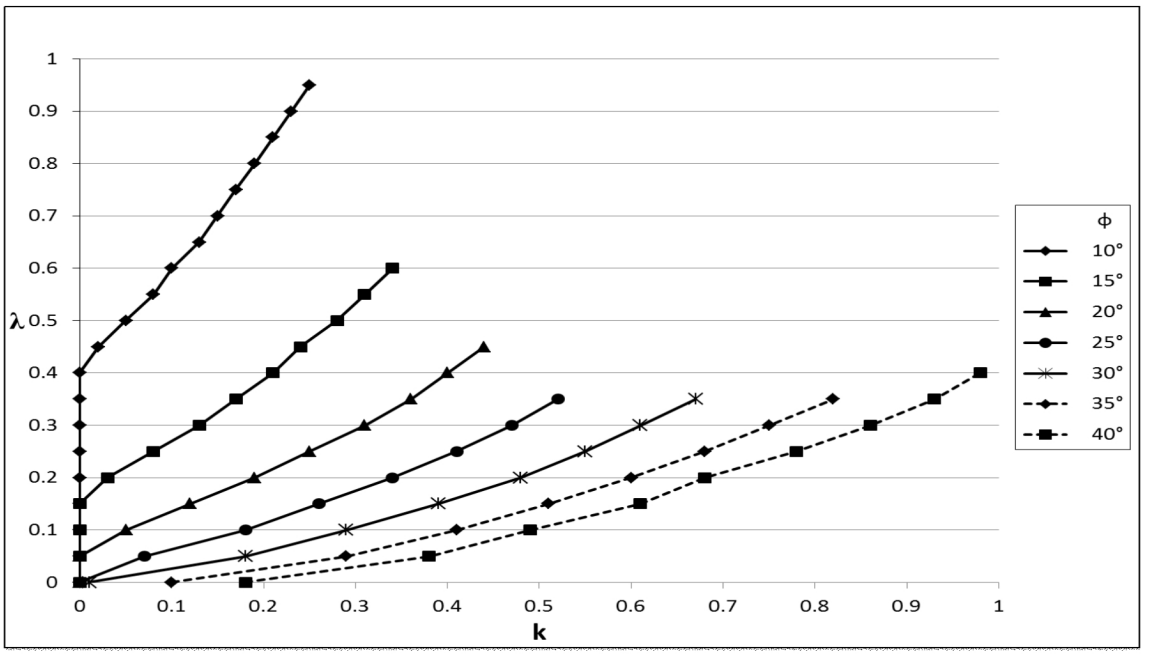

Figure B.3 Critical seismic coefficients for a 30° slope

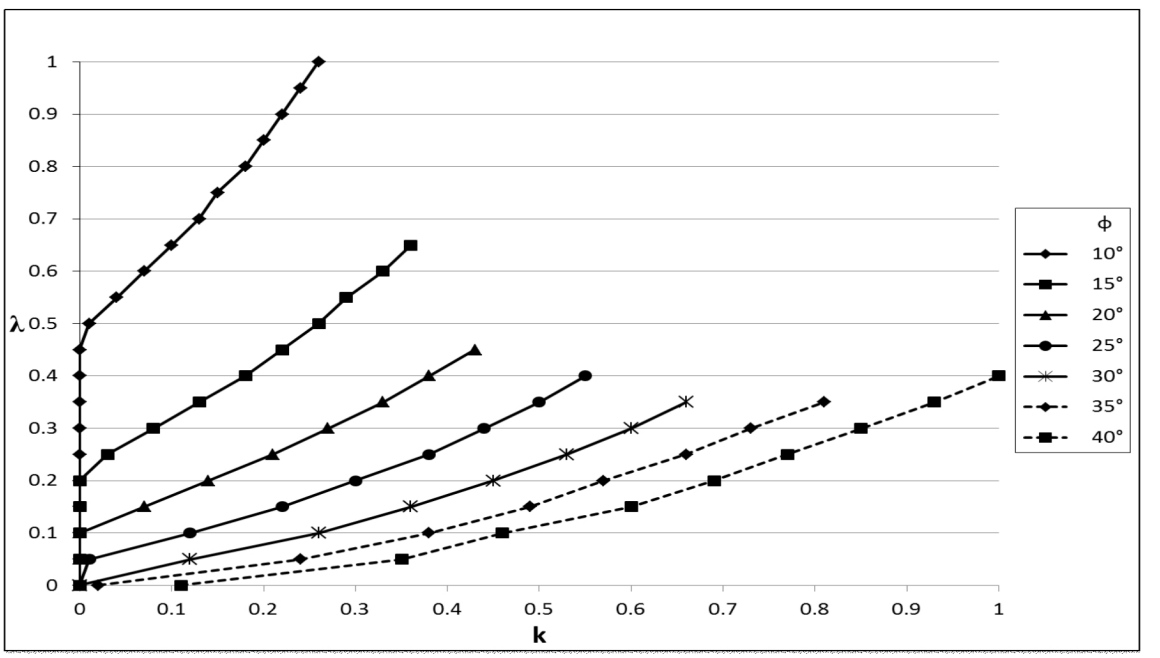

Figure B.4 Critical seismic coefficients for a 35° slope

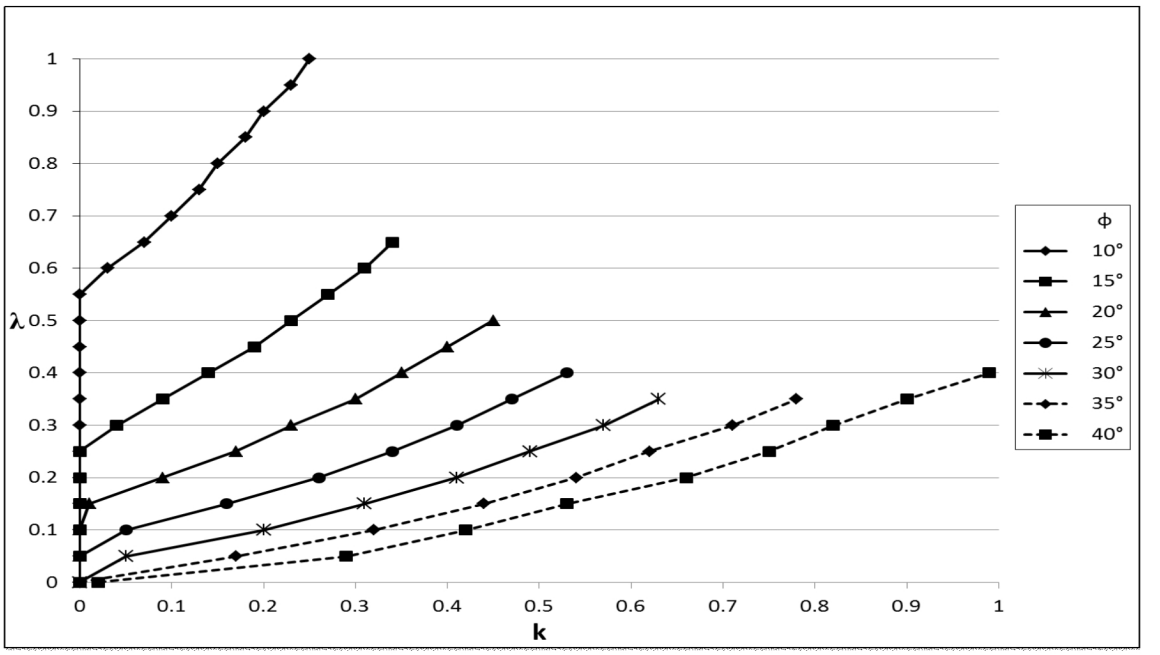

Figure B.5 Critical seismic coefficients for a 40° slope

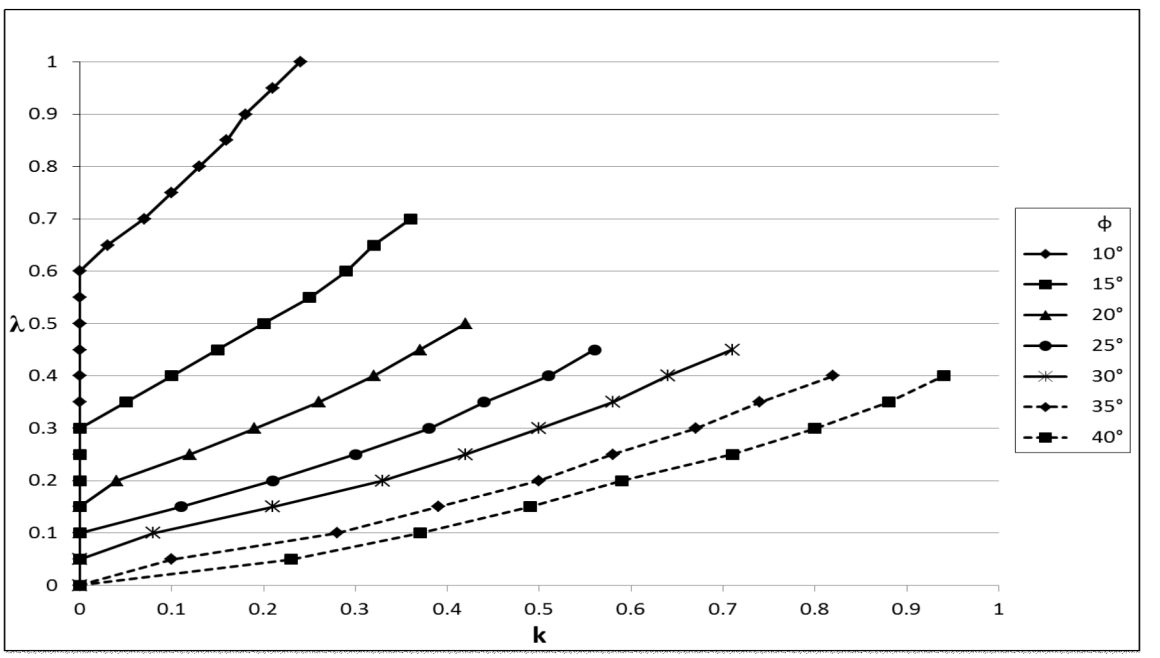

Figure B.6 Critical seismic coefficients for a 45° slope

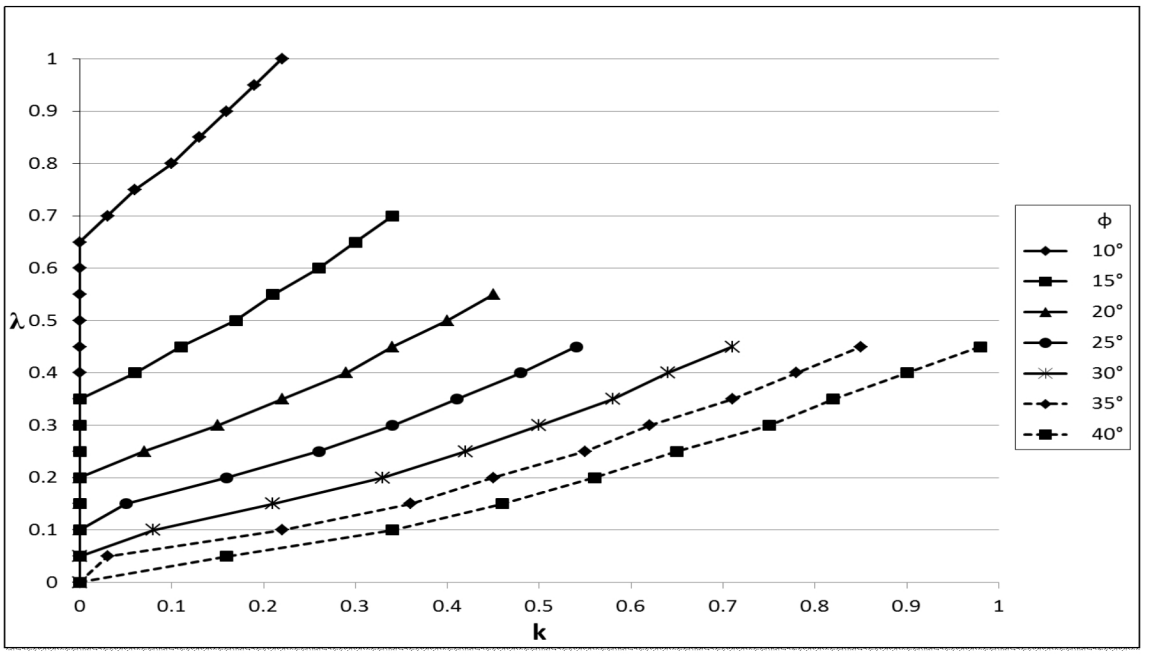

Figure B.7 Critical seismic coefficients for a 50° slope

B.2 Beta-curves

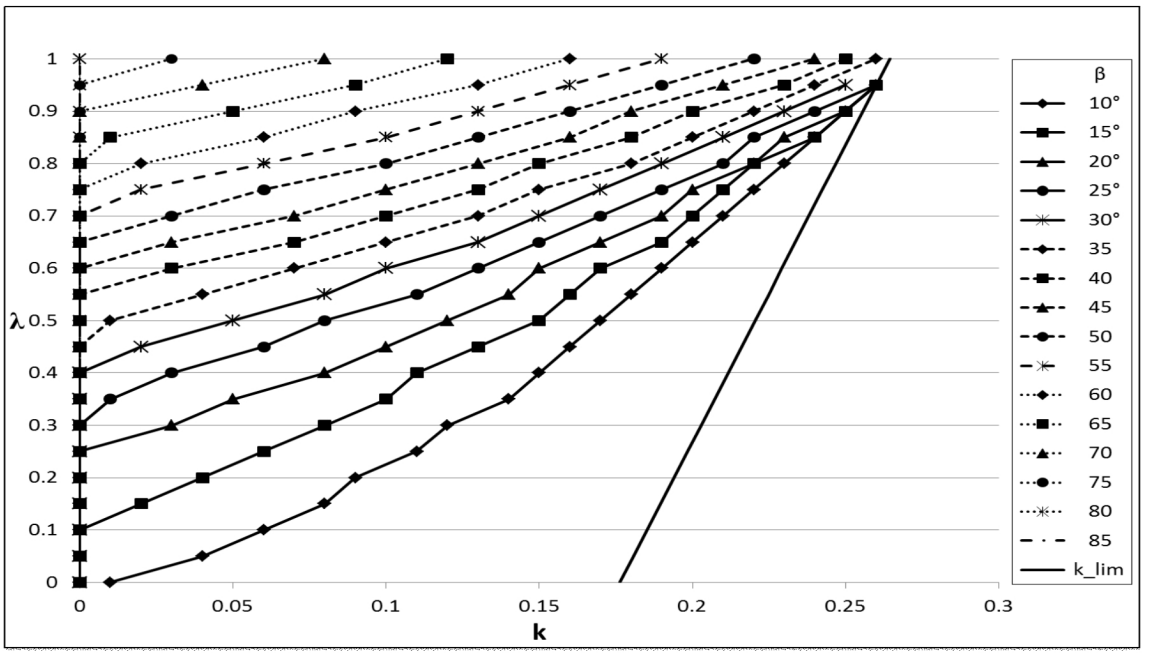

Figure B.8 Critical seismic coefficients for slopes with $\phi = 10°$

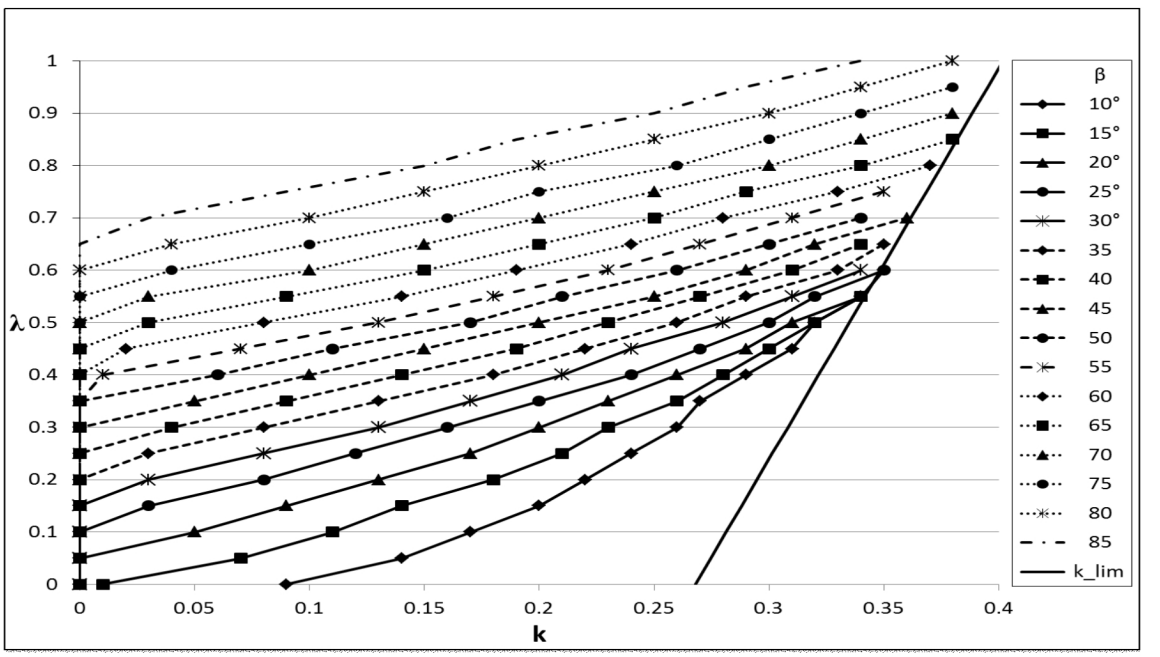

Figure B.9 Critical seismic coefficients for slopes with $\phi = 15°$

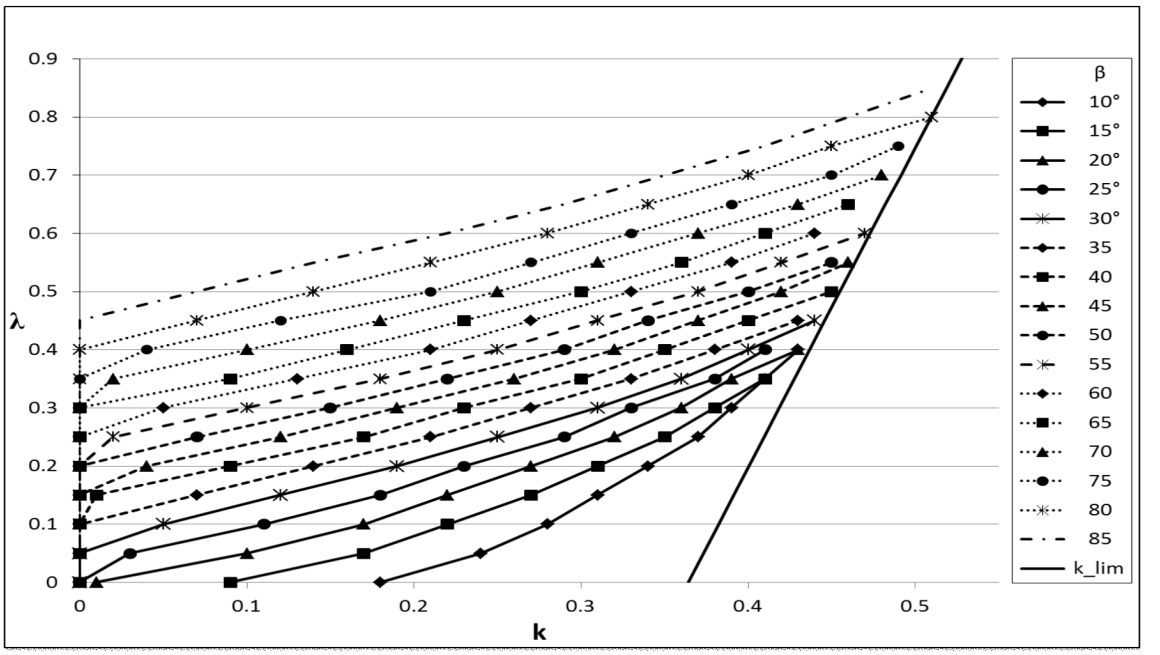

Figure B.10 Critical seismic coefficients for slopes with $\phi = 20°$

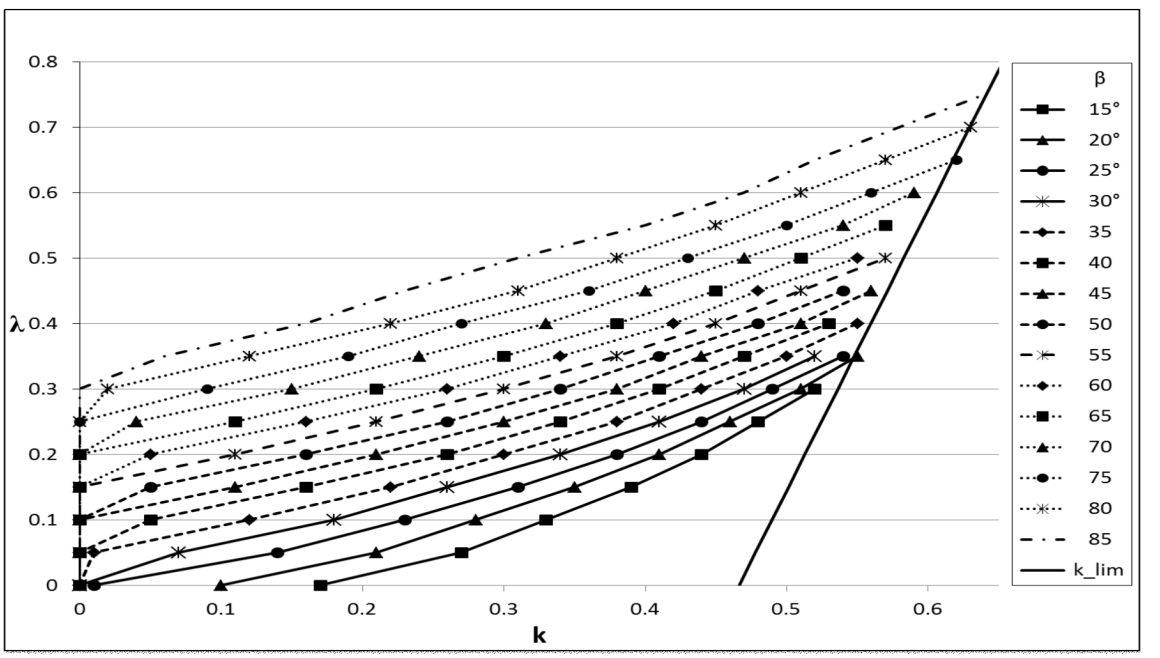

Figure B.11 Critical seismic coefficients for slopes with $\phi = 25°$

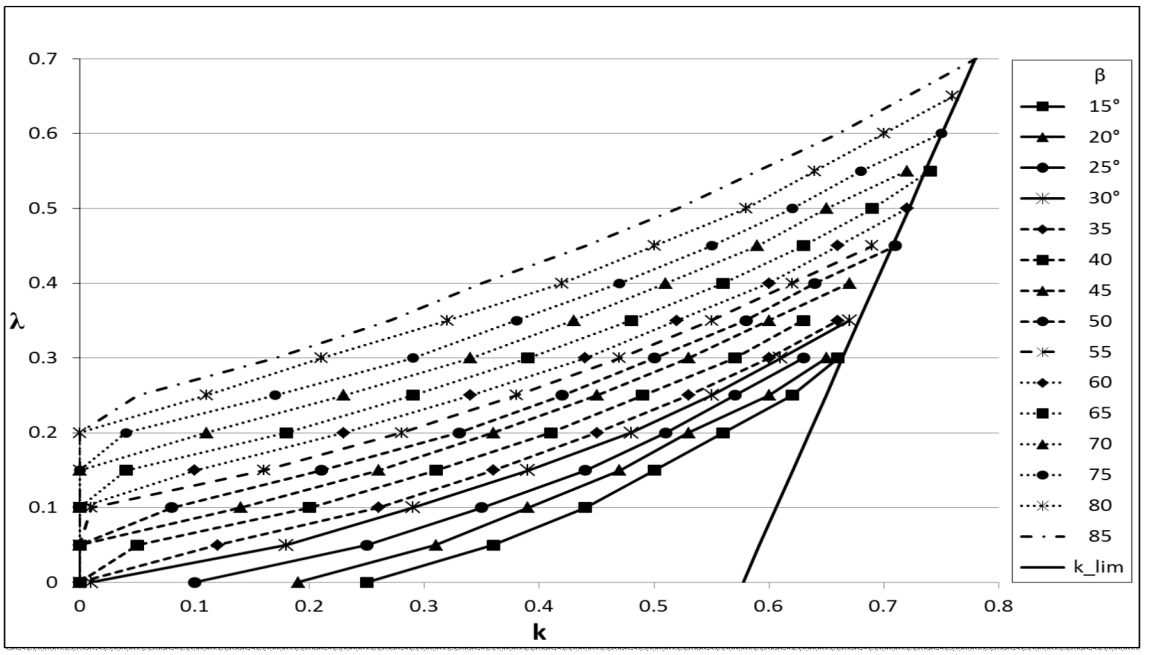

Figure B.12 Critical seismic coefficients for slopes with $\phi = 30°$

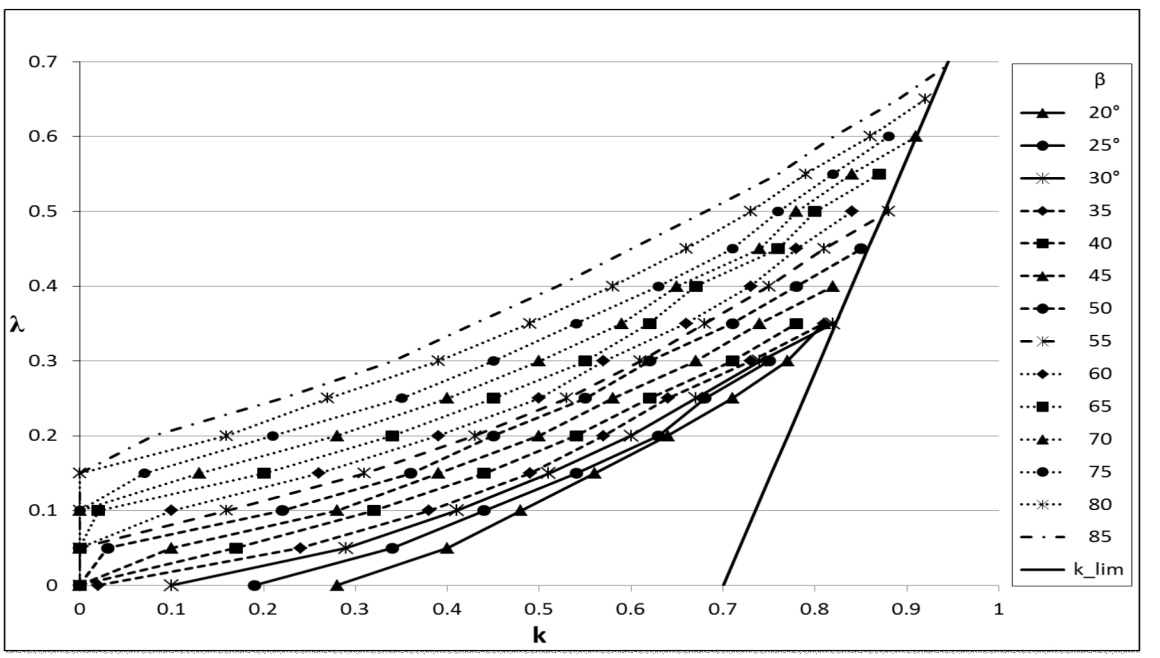

Figure B.13 Critical seismic coefficients for slopes with $\phi = 35°$

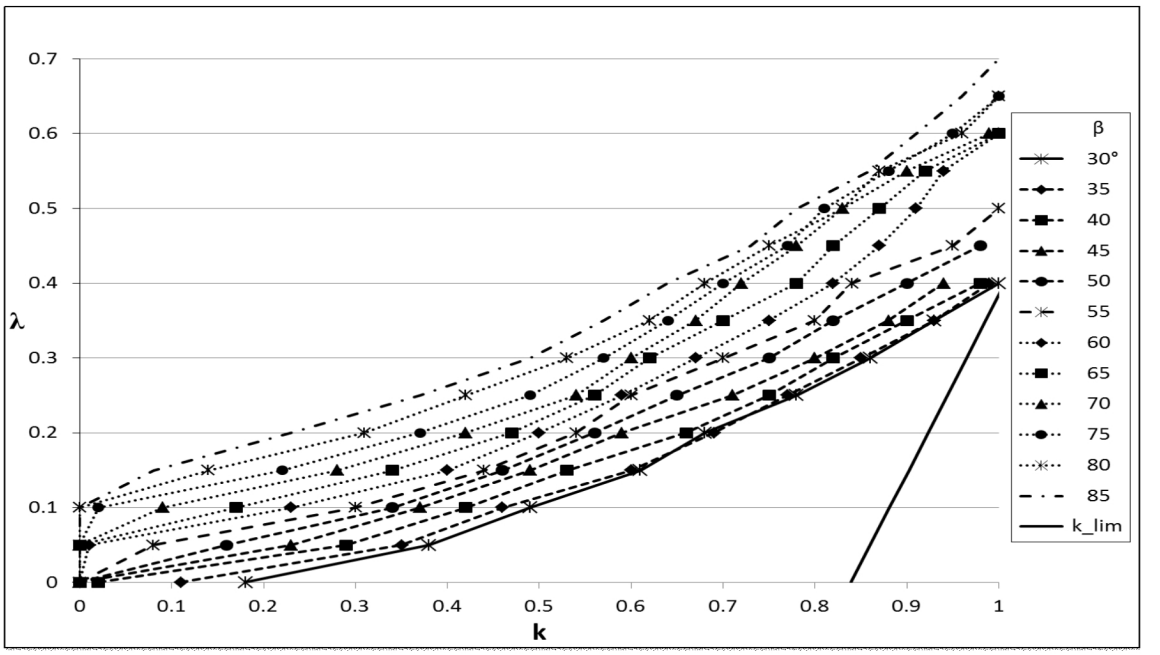

Figure B.14 Critical seismic coefficients for slopes with $\phi = 40°$

Appendix C

PROBABILISTIC SEISMIC SLOPE DESIGN CHARTS

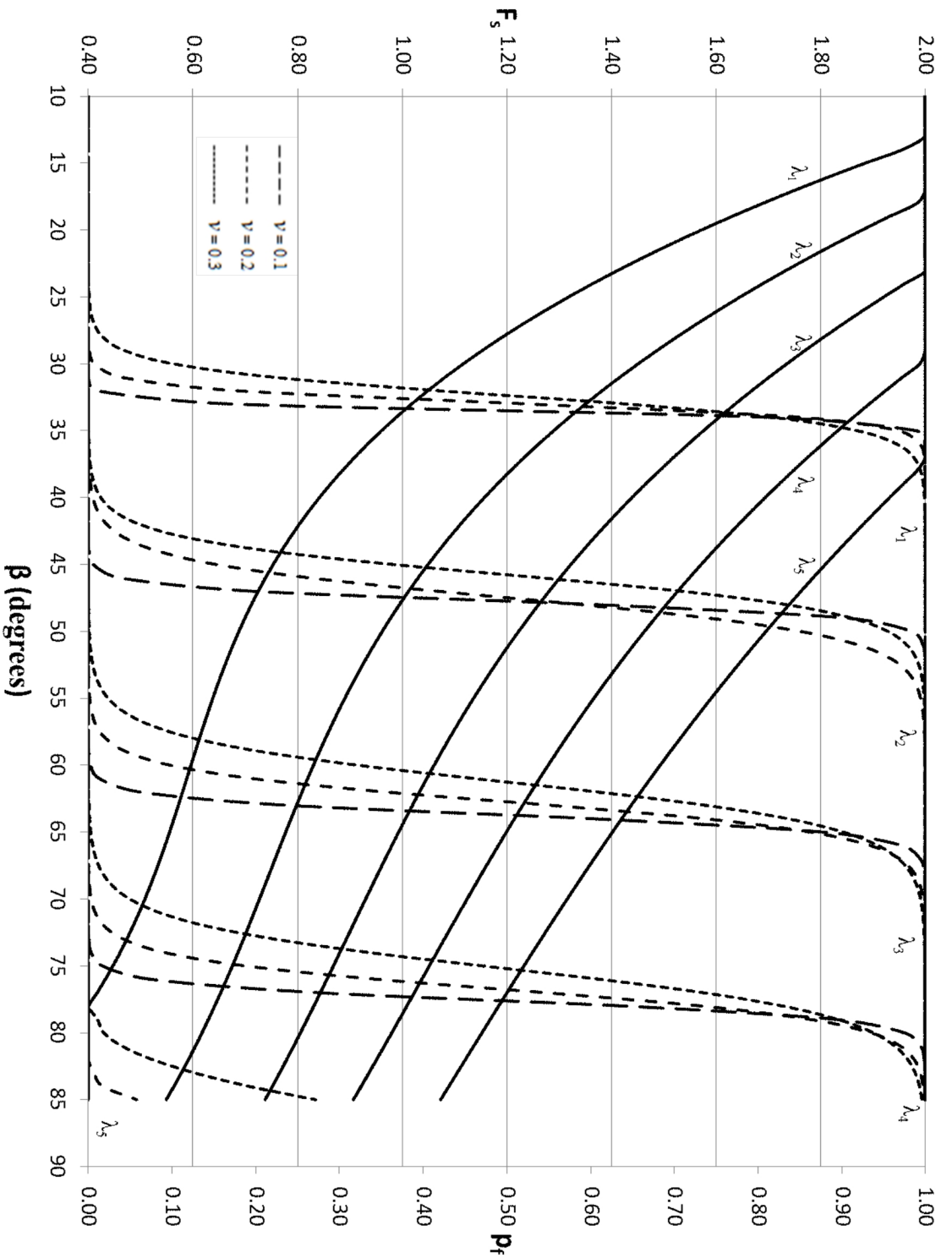

Figure C.1 Probabilistic pseudo-static slope stability design chart for $\mu_\phi = 20°$, $k = 0, \theta = 0.1H$. Solid lines plot F_s. $\lambda_i = i/10$

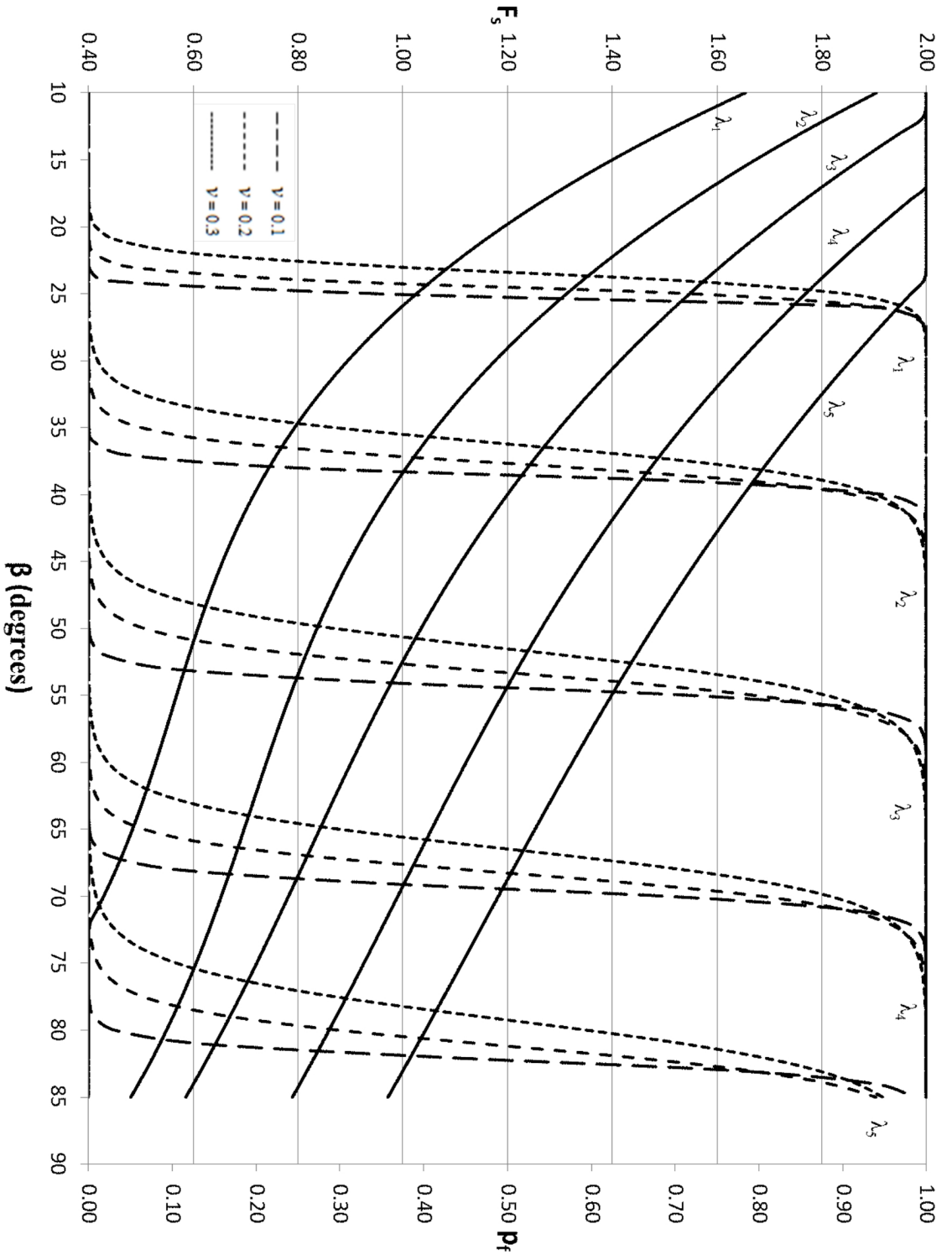

Figure C.2 Probabilistic pseudo-static slope stability design chart for $\mu_\phi = 20°$, $k = 0.1g$, $\theta = 0.1H$. Solid lines plot F_s. $\lambda_i = i/10$

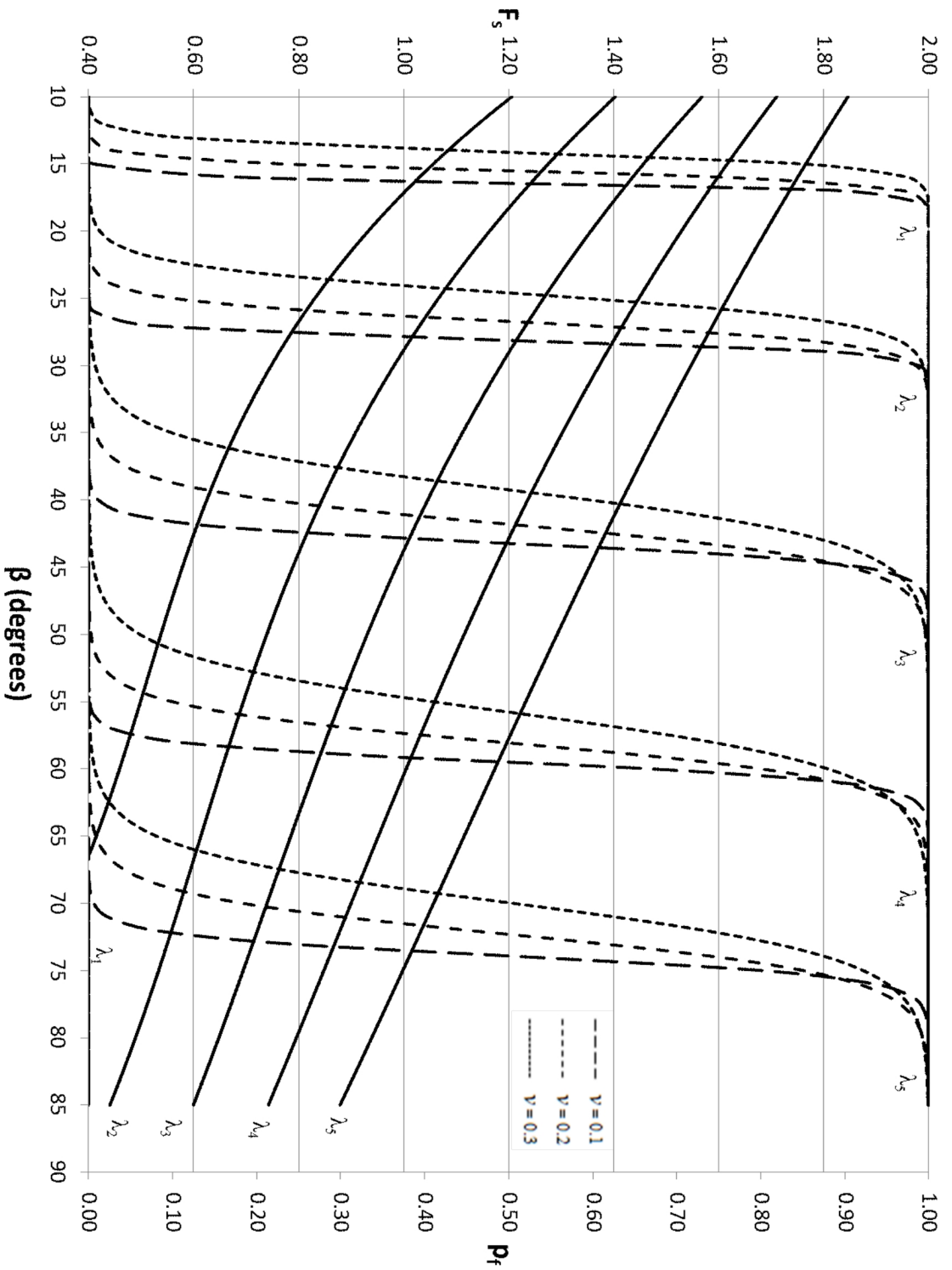

Figure C.3 Probabilistic pseudo-static slope stability design chart for $\mu_\phi = 20°$, $k = 0.2g$, $\theta = 0.1H$. Solid lines plot F_s. $\lambda_i = i/10$

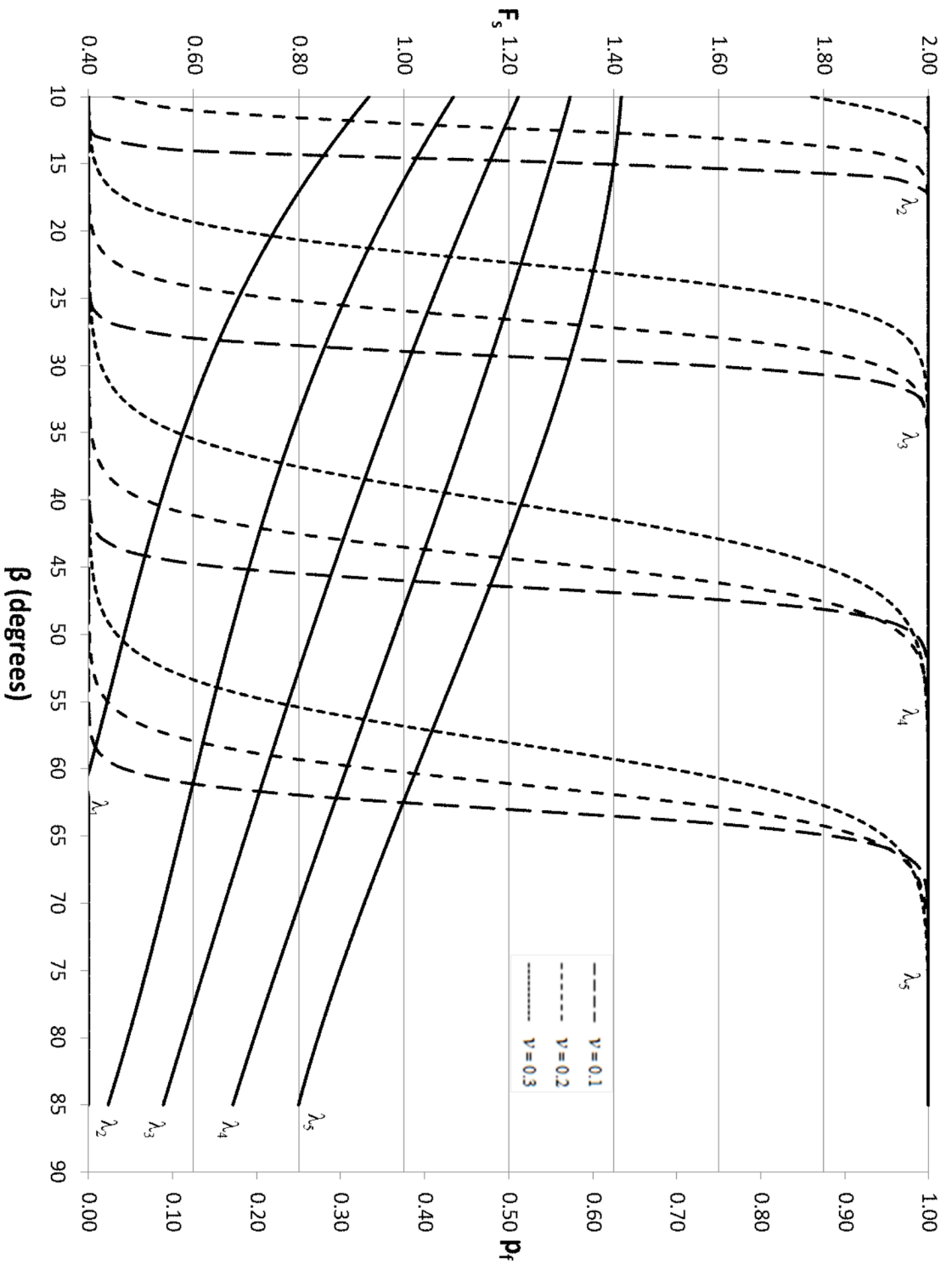

Figure C.4 Probabilistic pseudo-static slope stability design chart for $\mu_\phi = 20°$, $k = 0.3g$, $\theta = 0.1H$. Solid lines plot F_s. $\lambda_i = i/10$

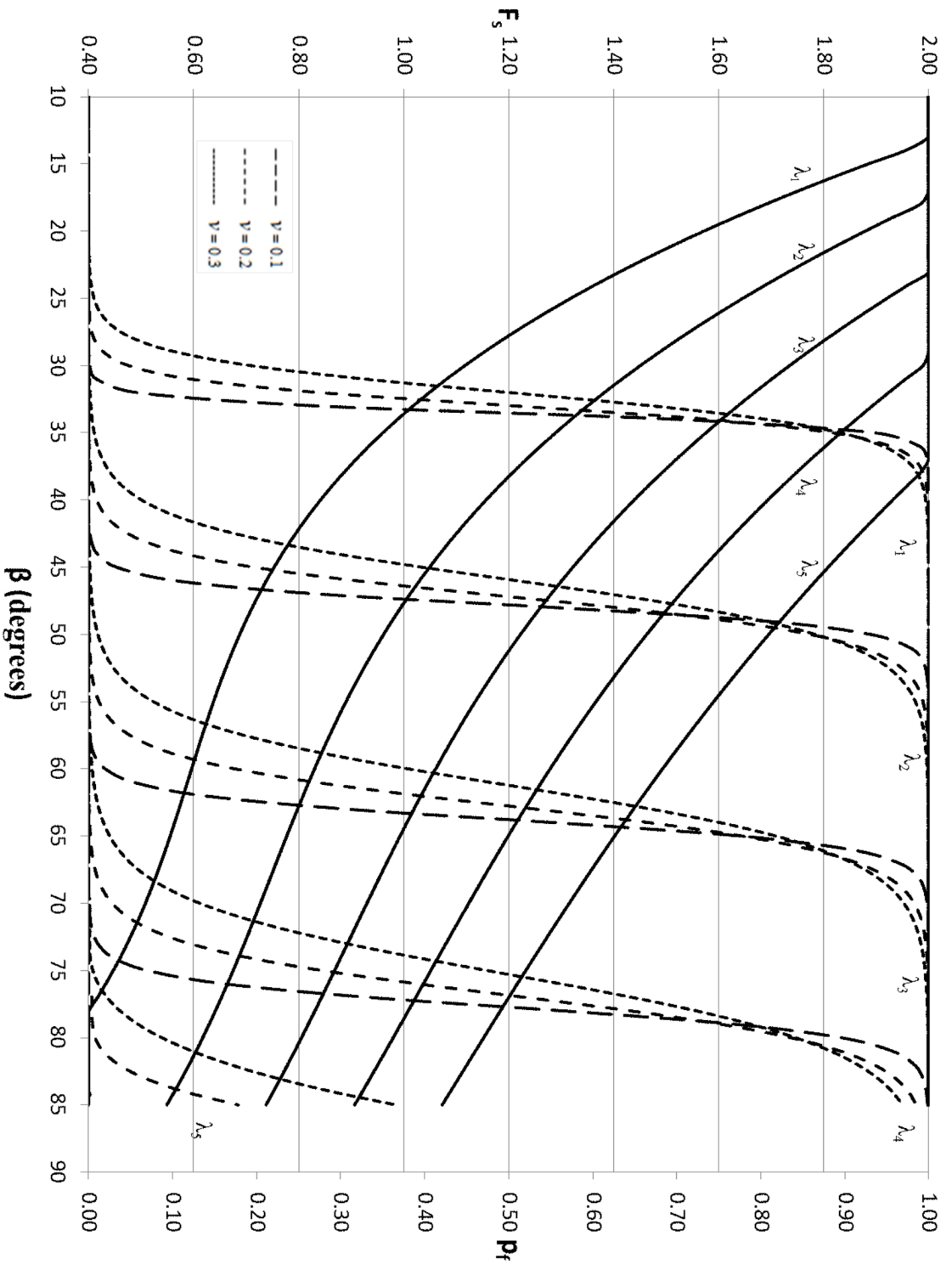

Figure C.5 Probabilistic pseudo-static slope stability design chart for $\mu_\phi = 20°$, $k = 0, \theta = 0.2H$. Solid lines plot F_s. $\lambda_i = i/10$

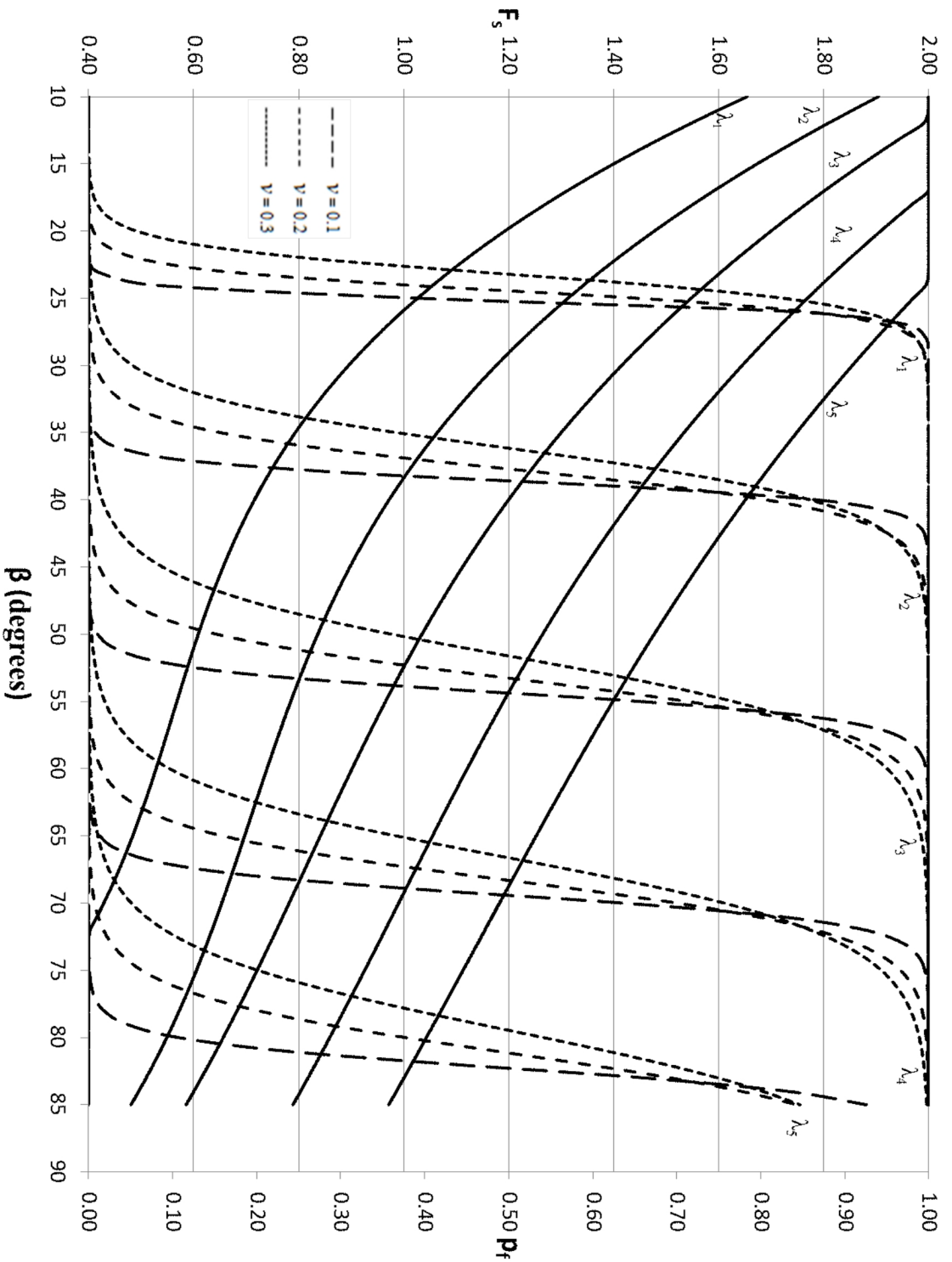

Figure C.6 Probabilistic pseudo-static slope stability design chart for $\mu_\phi = 20°$, $k = 0.1g$, $\theta = 0.2H$. Solid lines plot F_s. $\lambda_i = i/10$

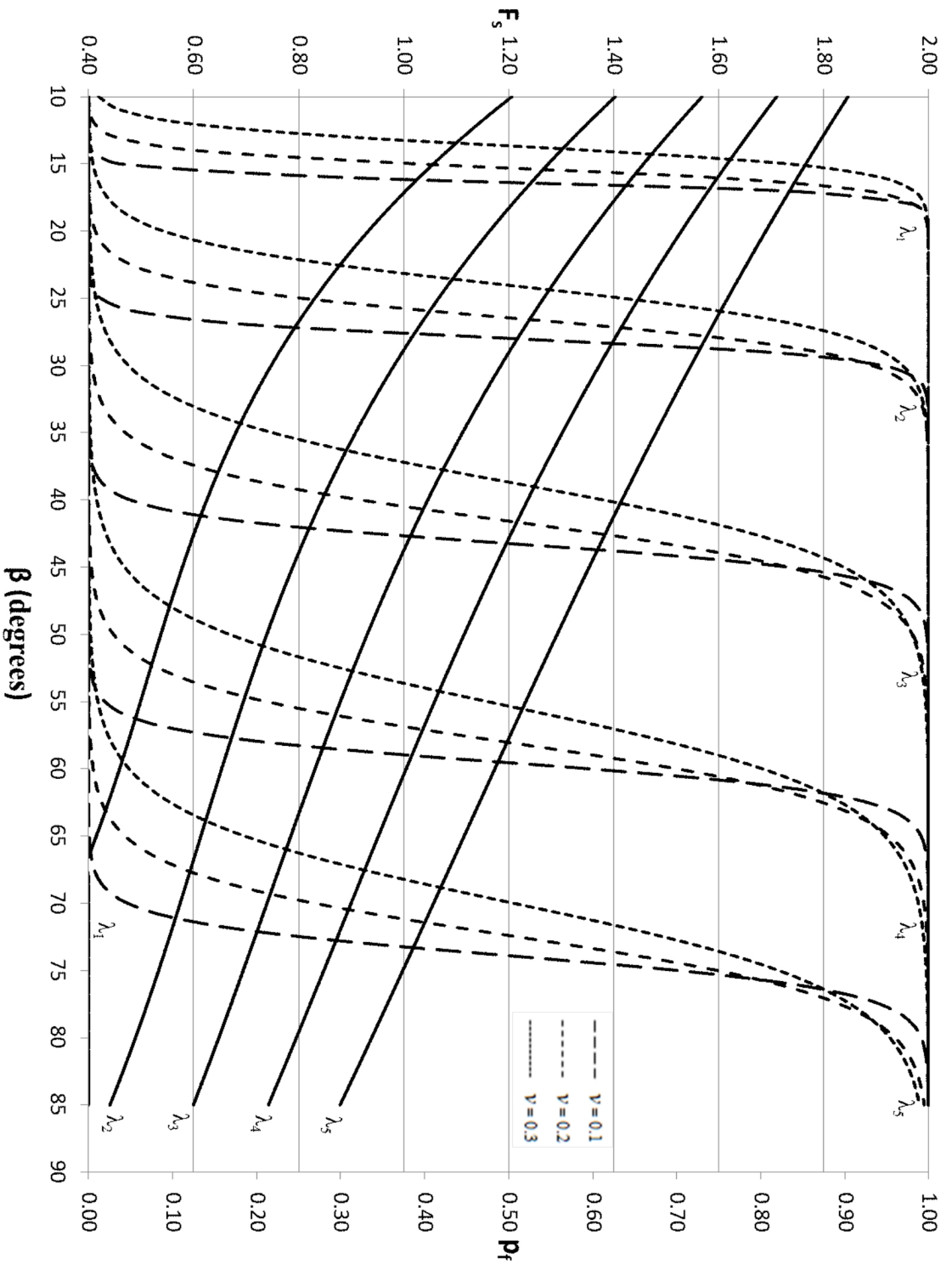

Figure C.7 Probabilistic pseudo-static slope stability design chart for $\mu_\phi = 20°$, $k = 0.2g$, $\theta = 0.2H$. Solid lines plot F_s. $\lambda_i = i/10$

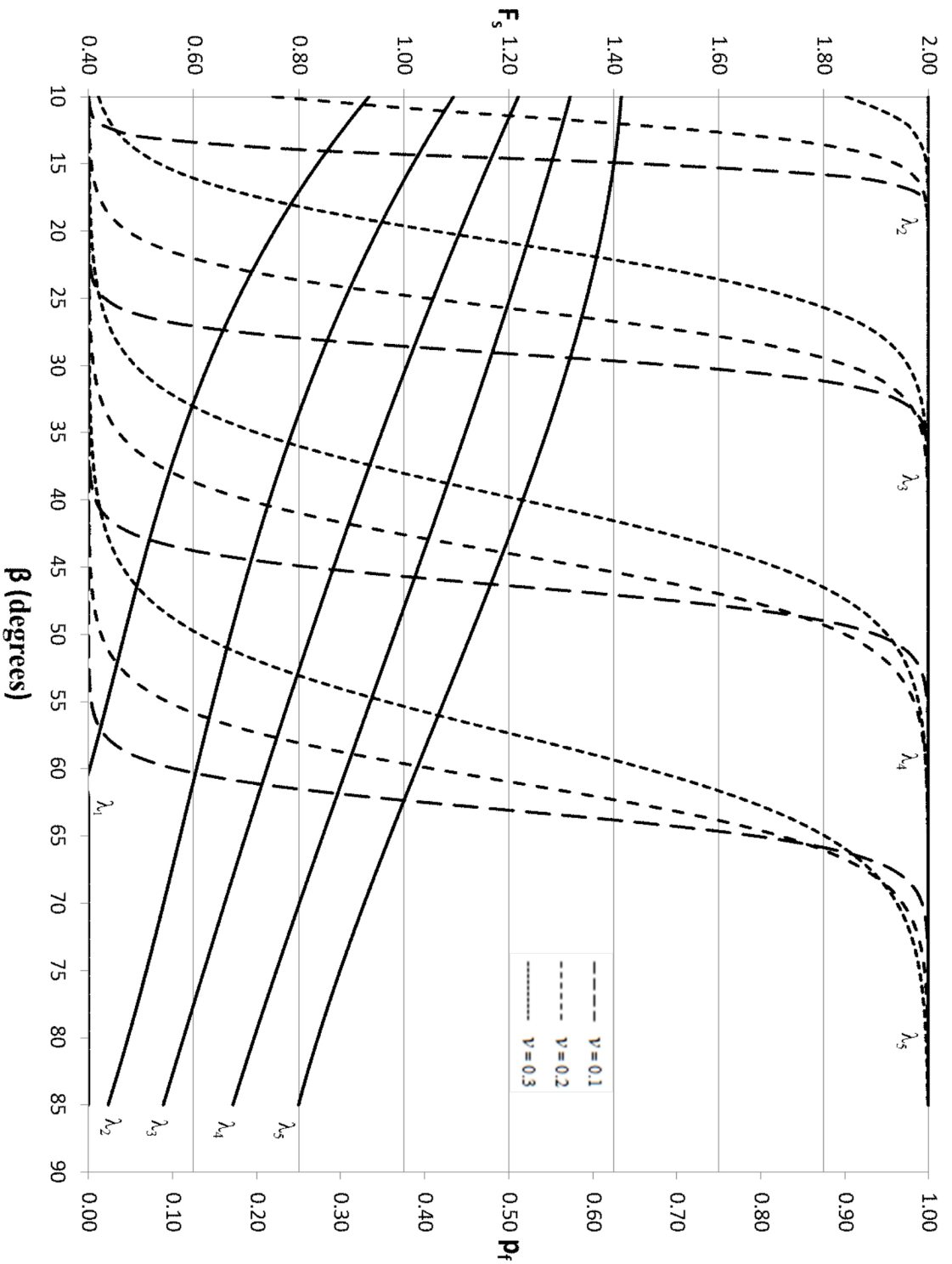

Figure C.8 Probabilistic pseudo-static slope stability design chart for $\mu_\phi = 20°$, $k = 0.3g$, $\theta = 0.2H$. Solid lines plot F_s. $\lambda_i = i/10$

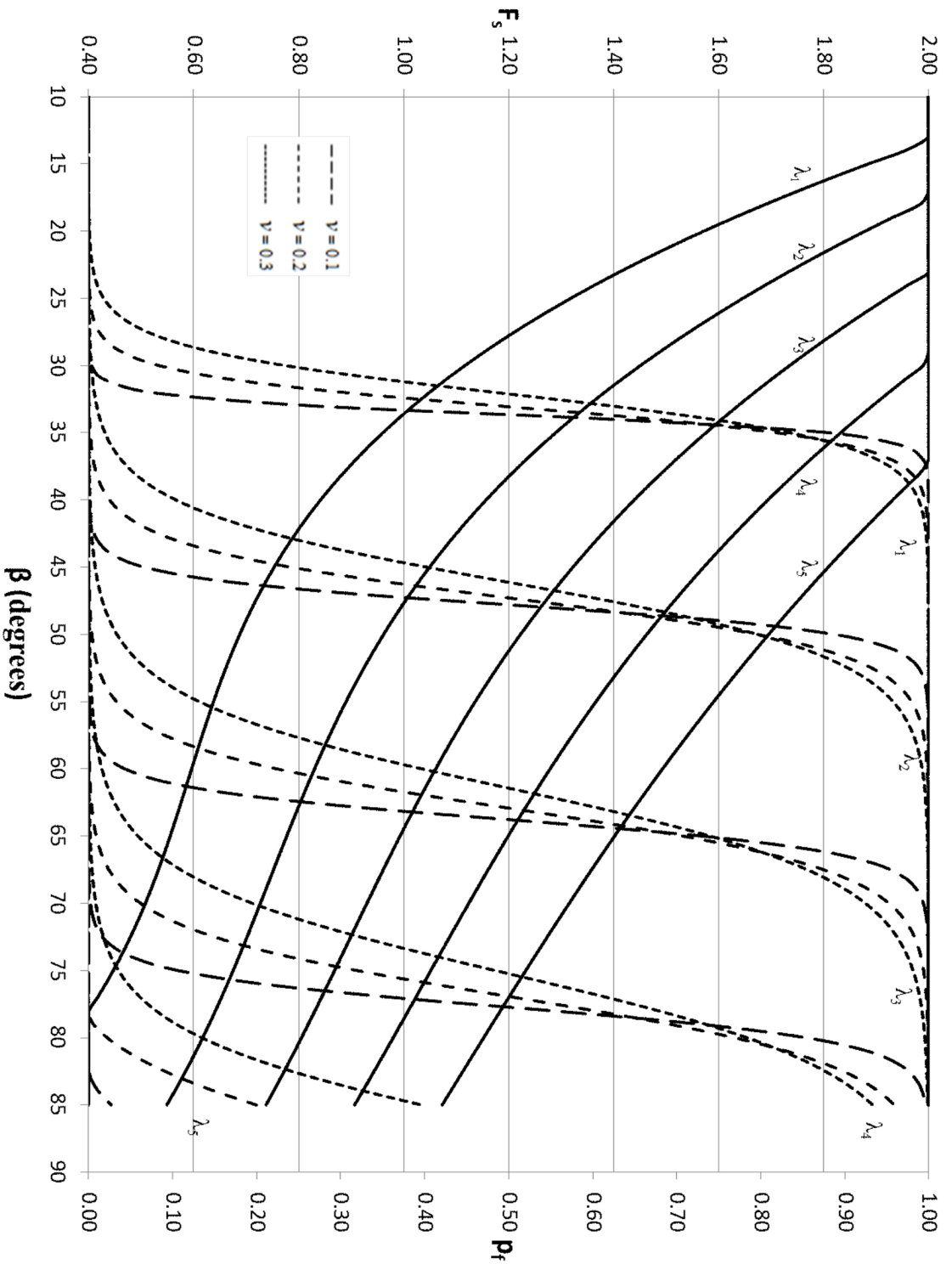

Figure C.9 Probabilistic pseudo-static slope stability design chart for $\mu_\phi = 20°$, $k = 0, \theta = 0.3H$. Solid lines plot F_s. $\lambda_i = i/10$

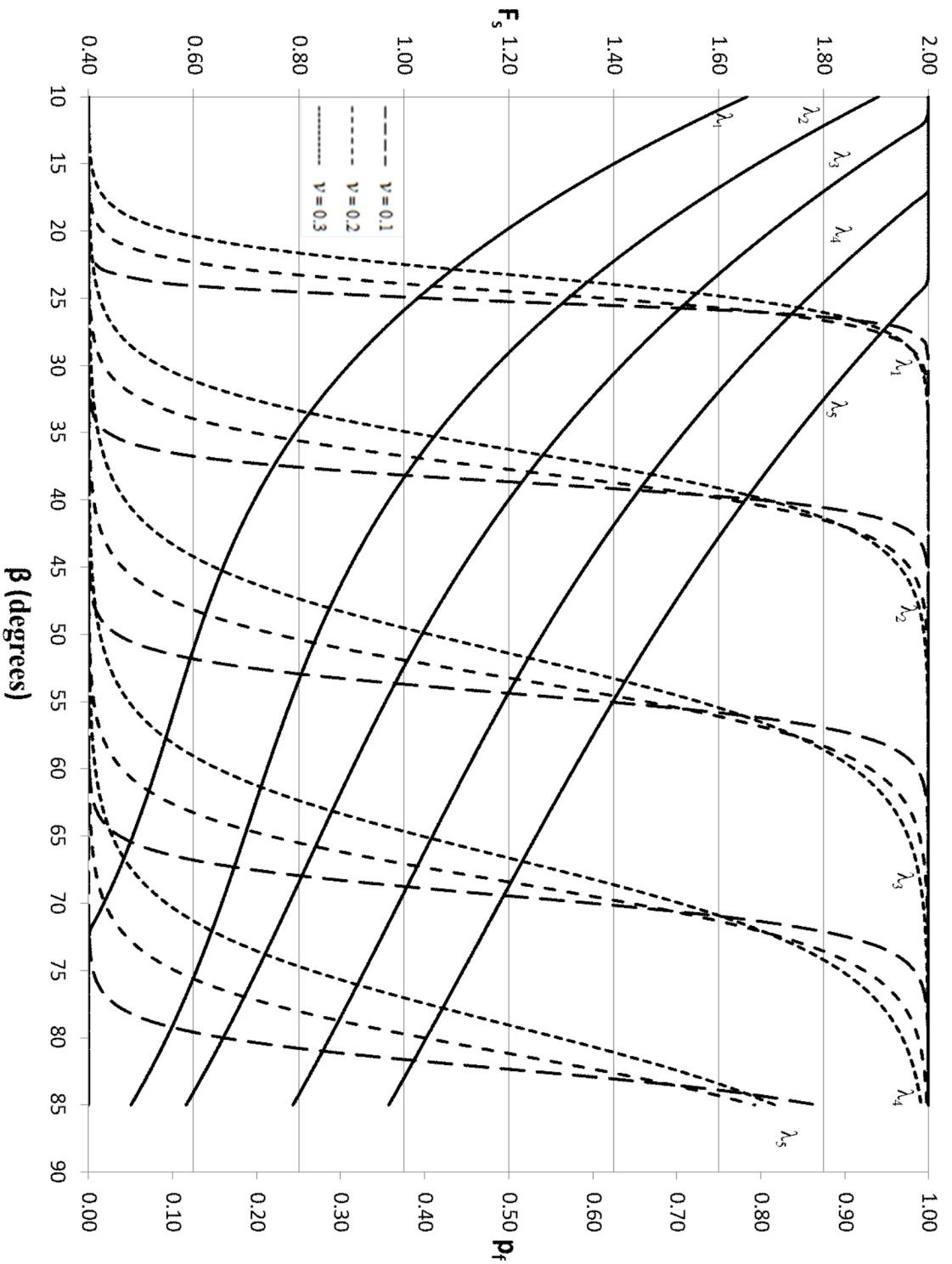

Figure C.10 Probabilistic pseudo-static slope stability design chart for $\mu_\phi = 20°$, $k = 0.1g$, $\theta = 0.3H$. Solid lines plot F_s. $\lambda_i = i/10$

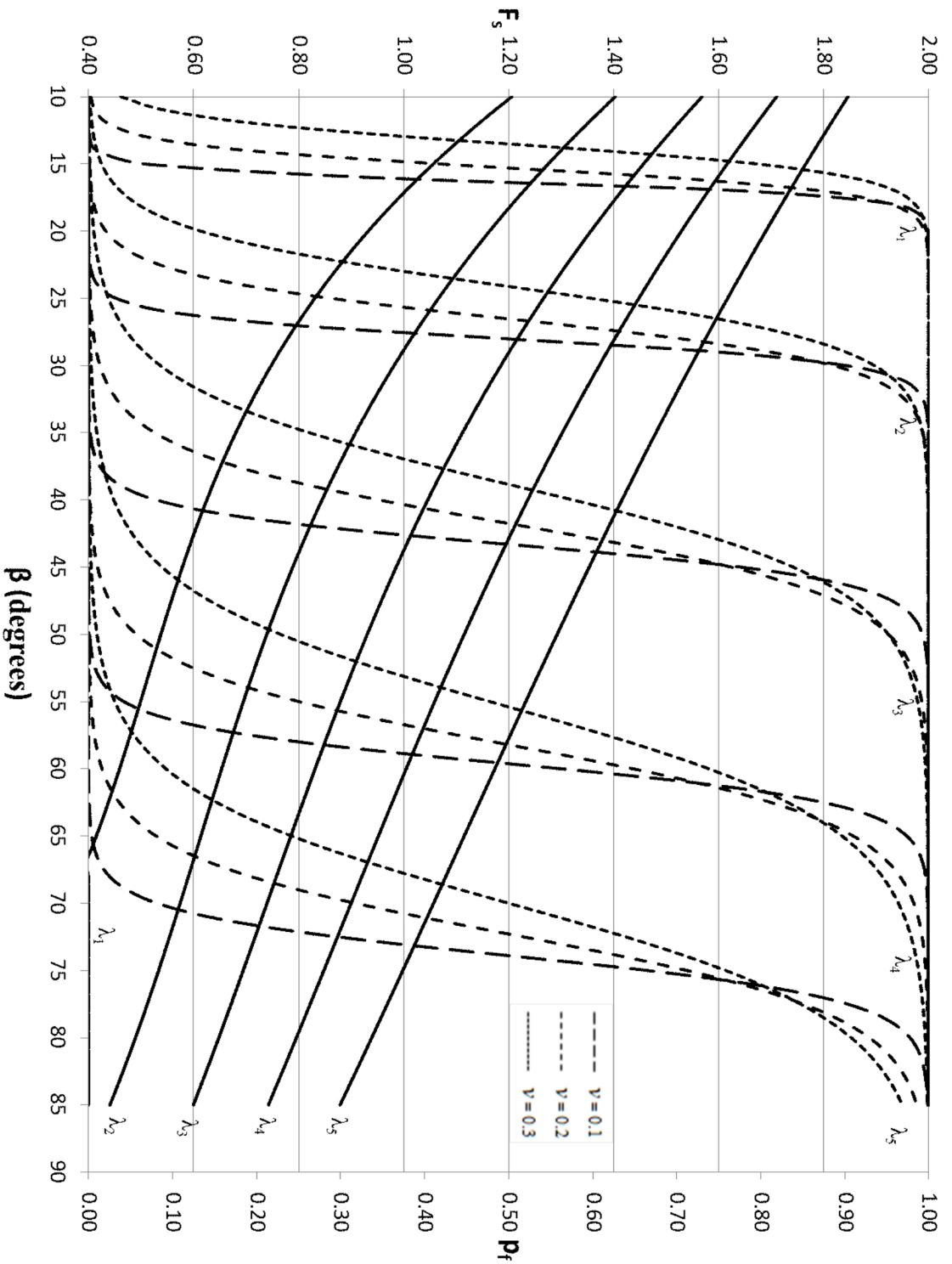

Figure C.11 Probabilistic pseudo-static slope stability design chart for $\mu_\phi = 20°$, $k = 0.2g$, $\theta = 0.3H$. Solid lines plot F_s. $\lambda_i = i/10$

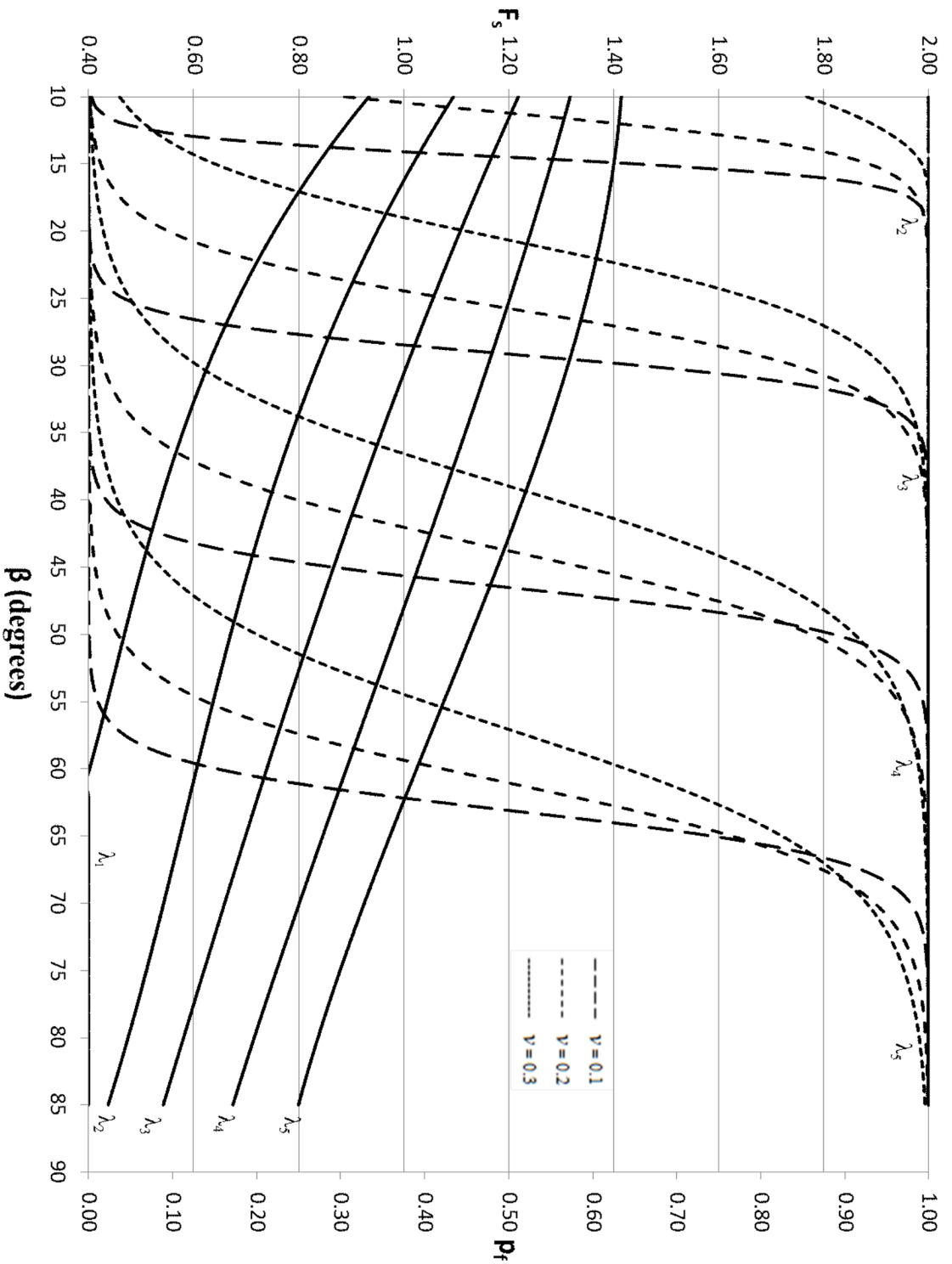

Figure C.12 Probabilistic pseudo-static slope stability design chart for $\mu_\phi = 20°$, $k = 0.3g$, $\theta = 0.3H$. Solid lines plot F_s. $\lambda_i = i/10$

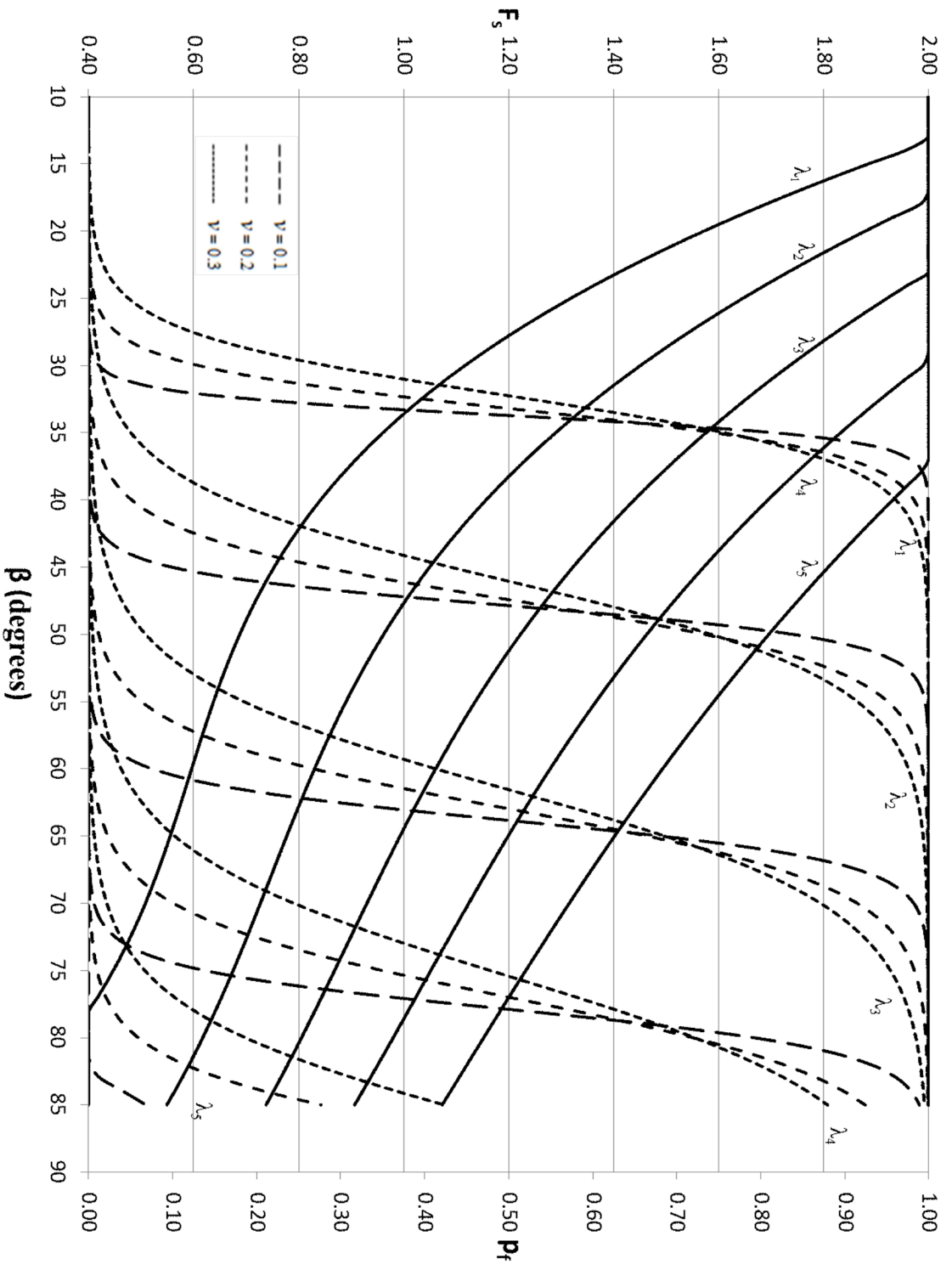

Figure C.13 Probabilistic pseudo-static slope stability design chart for $\mu_\phi = 20°$, $k = 0$, $\theta = 0.5H$. Solid lines plot F_s. $\lambda_i = i/10$

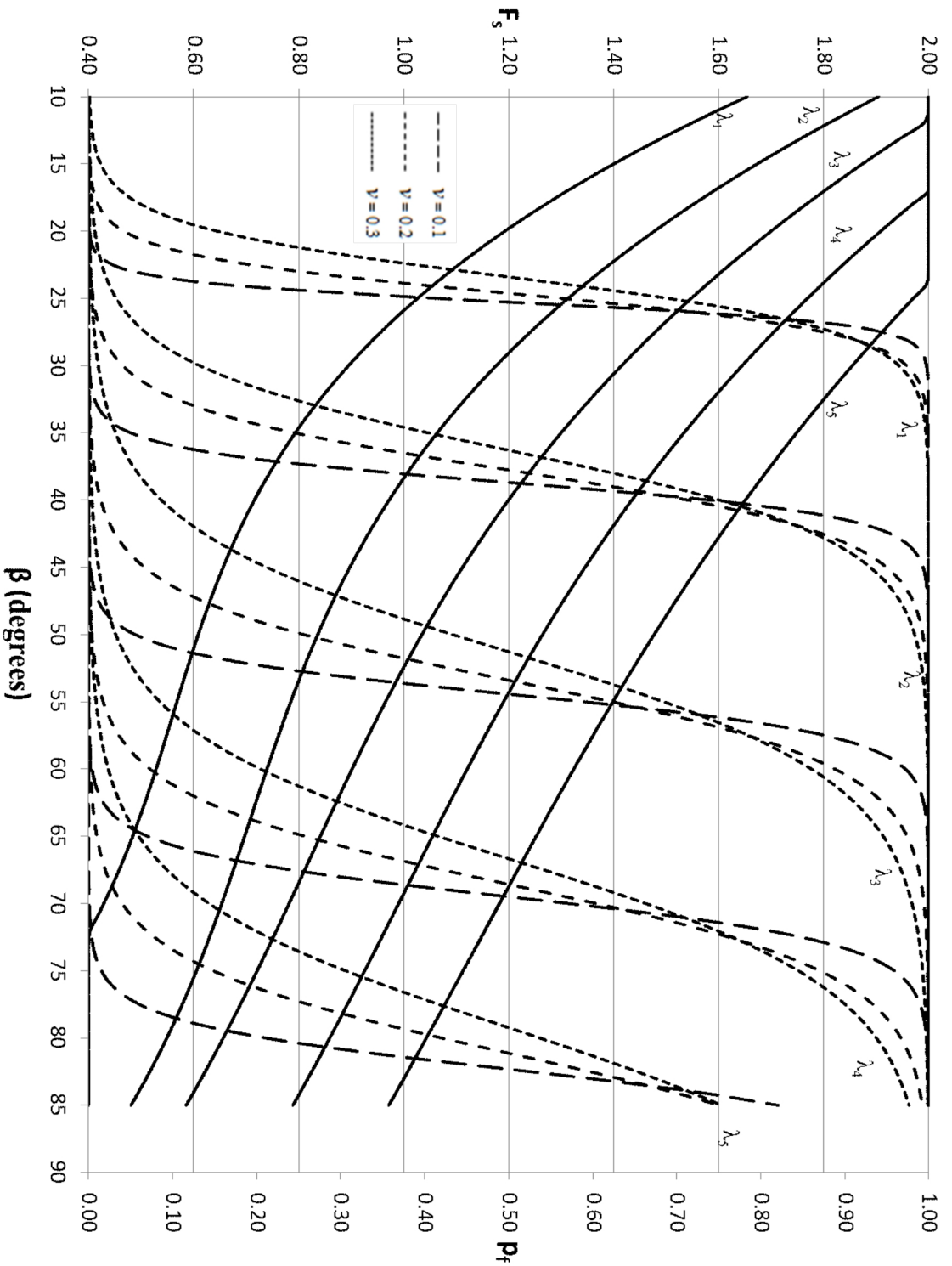

Figure C.14 Probabilistic pseudo-static slope stability design chart for $\mu_\phi = 20°$, $k = 0.1g$, $\theta = 0.5H$. Solid lines plot F_s. $\lambda_i = i/10$

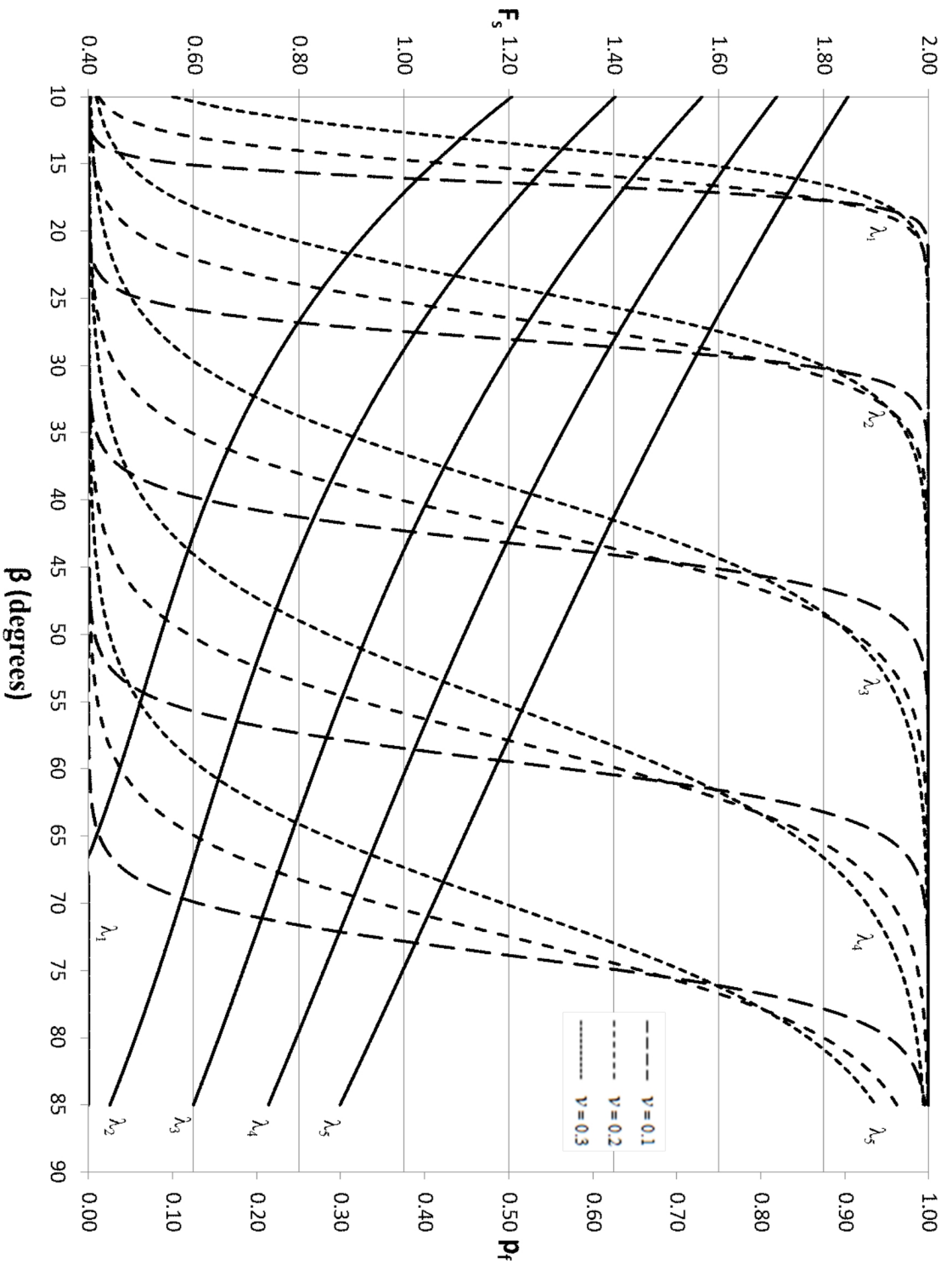

Figure C.15 Probabilistic pseudo-static slope stability design chart for $\mu_\phi = 20°$, $k = 0.2g$, $\theta = 0.5H$. Solid lines plot F_s. $\lambda_i = i/10$

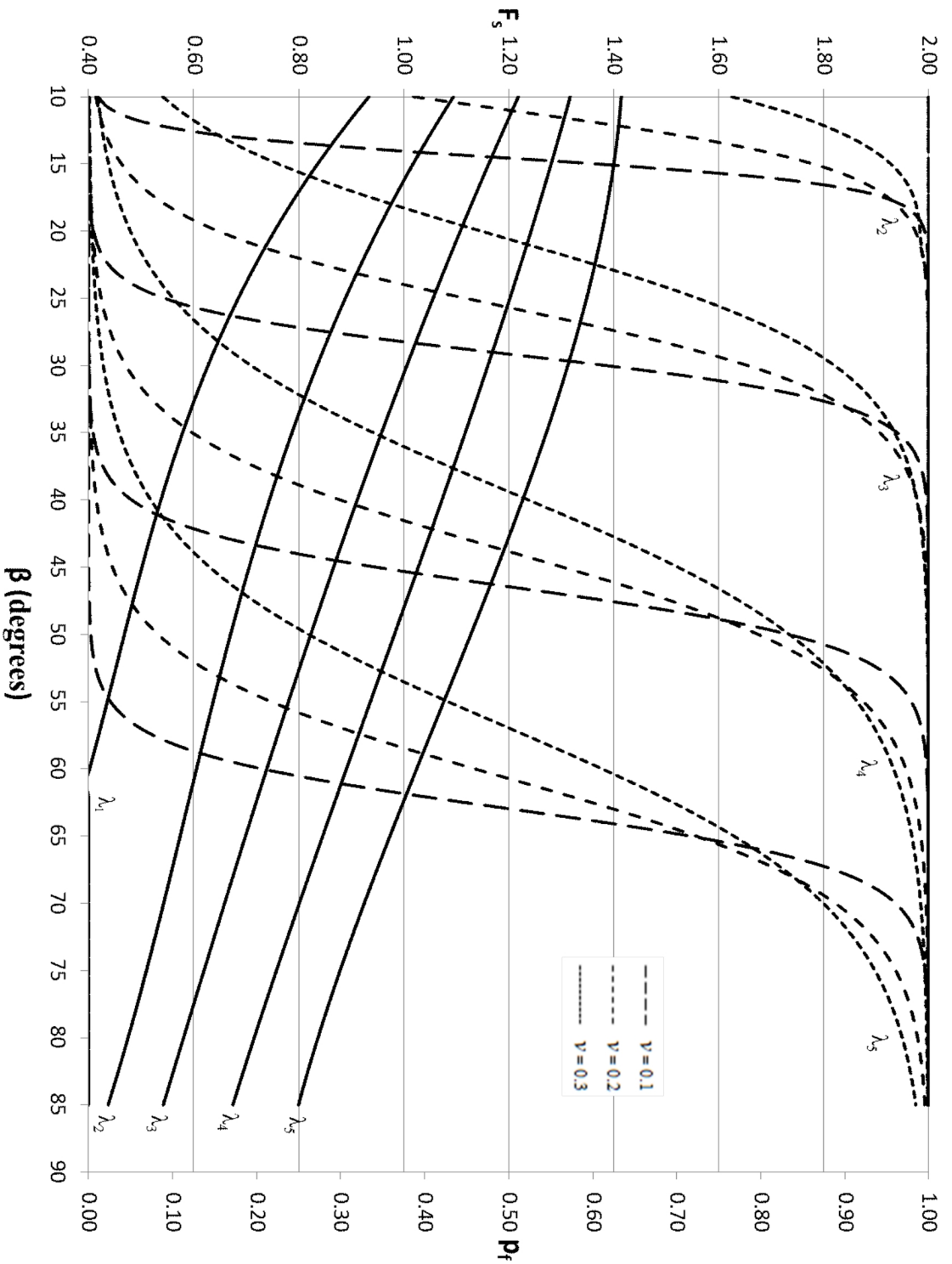

Figure C.16 Probabilistic pseudo-static slope stability design chart for $\mu_\phi = 20°$, $k = 0.3g$, $\theta = 0.5H$. Solid lines plot F_s. $\lambda_i = i/10$

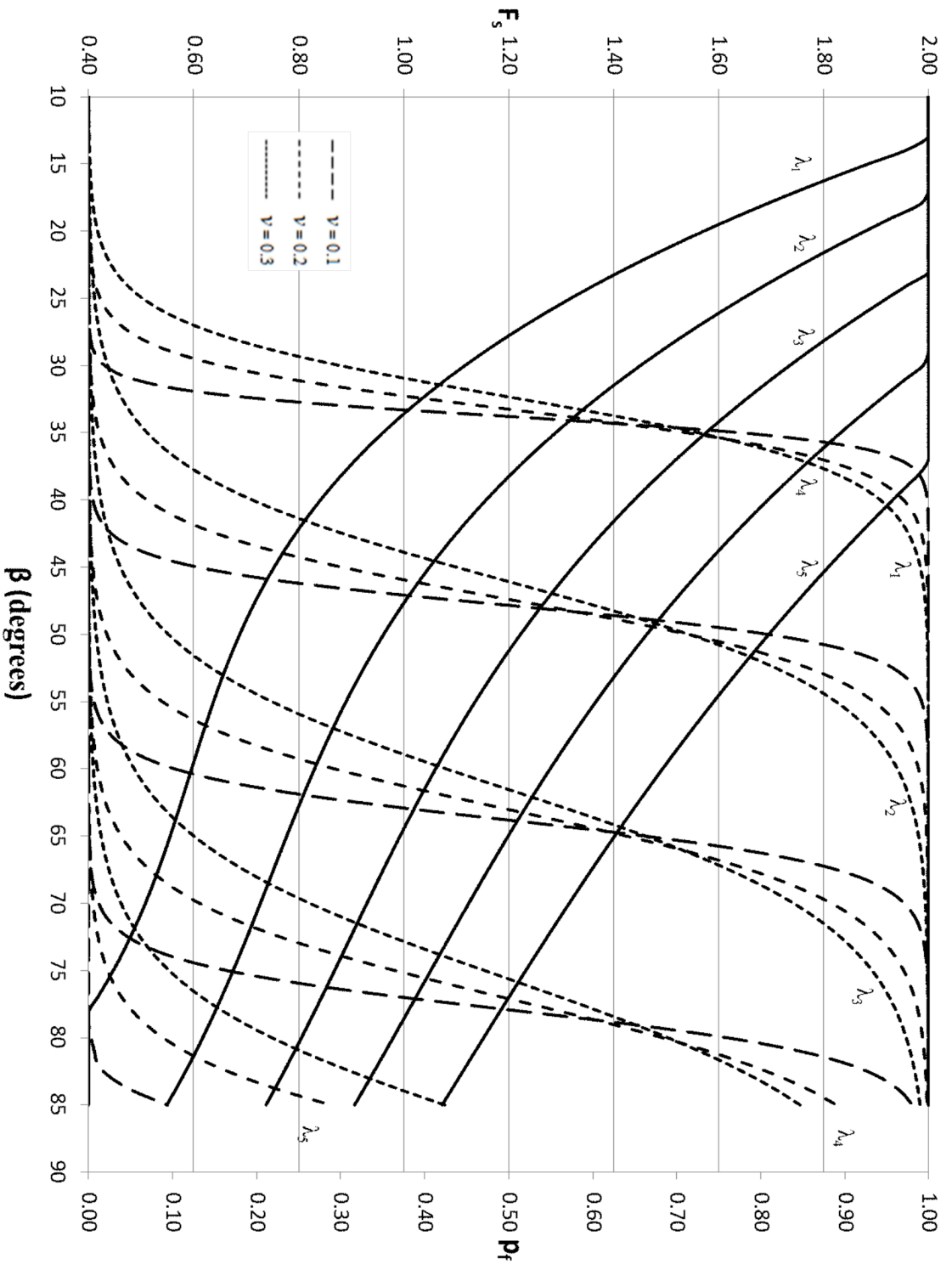

Figure C.17 Probabilistic pseudo-static slope stability design chart for $\mu_\phi = 20°$, $k = 0$, $\theta = 0.7H$. Solid lines plot F_s. $\lambda_i = i/10$

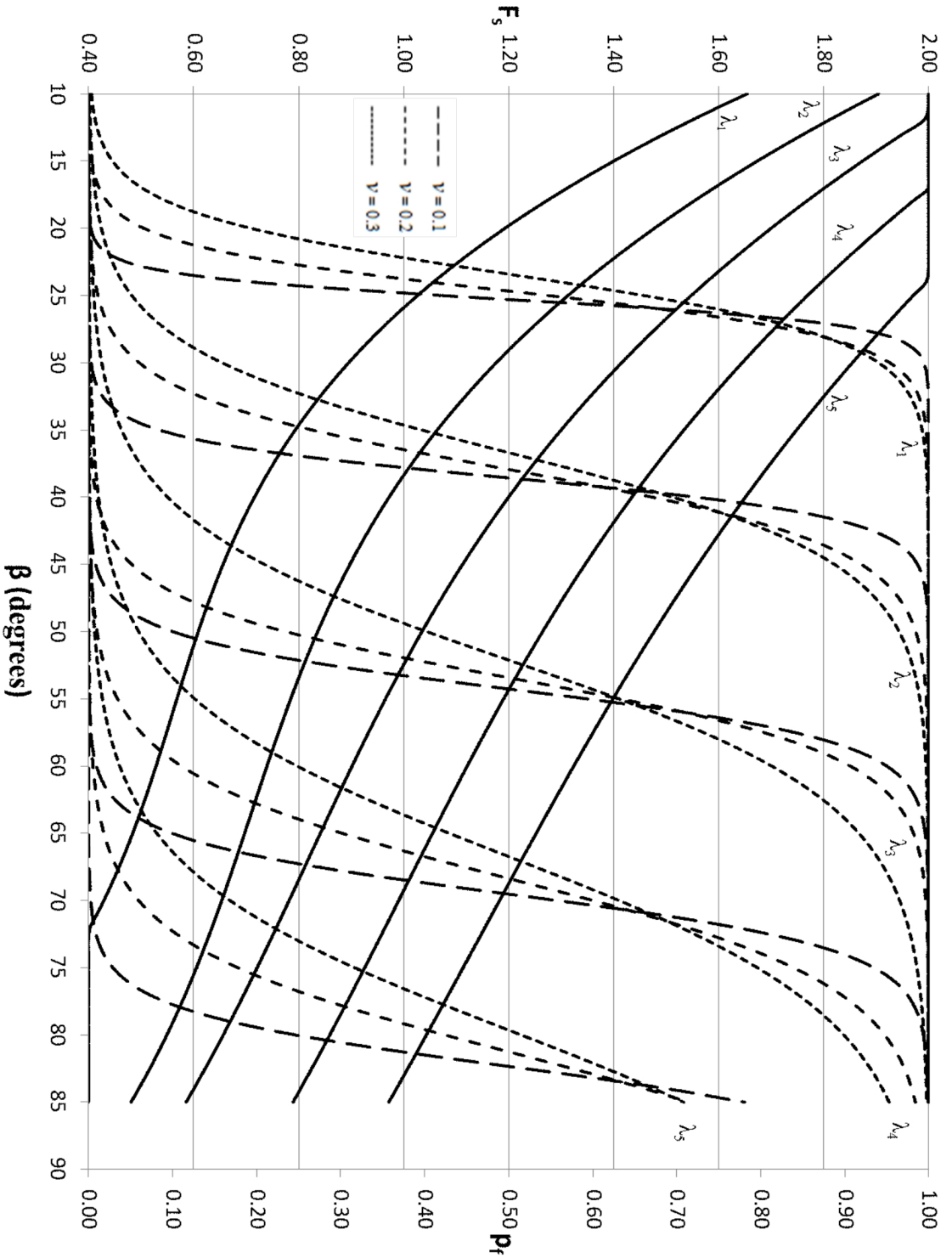

Figure C.18 Probabilistic pseudo-static slope stability design chart for $\mu_\phi = 20°$, $k = 0.1g$, $\theta = 0.7H$. Solid lines plot F_s. $\lambda_i = i/10$

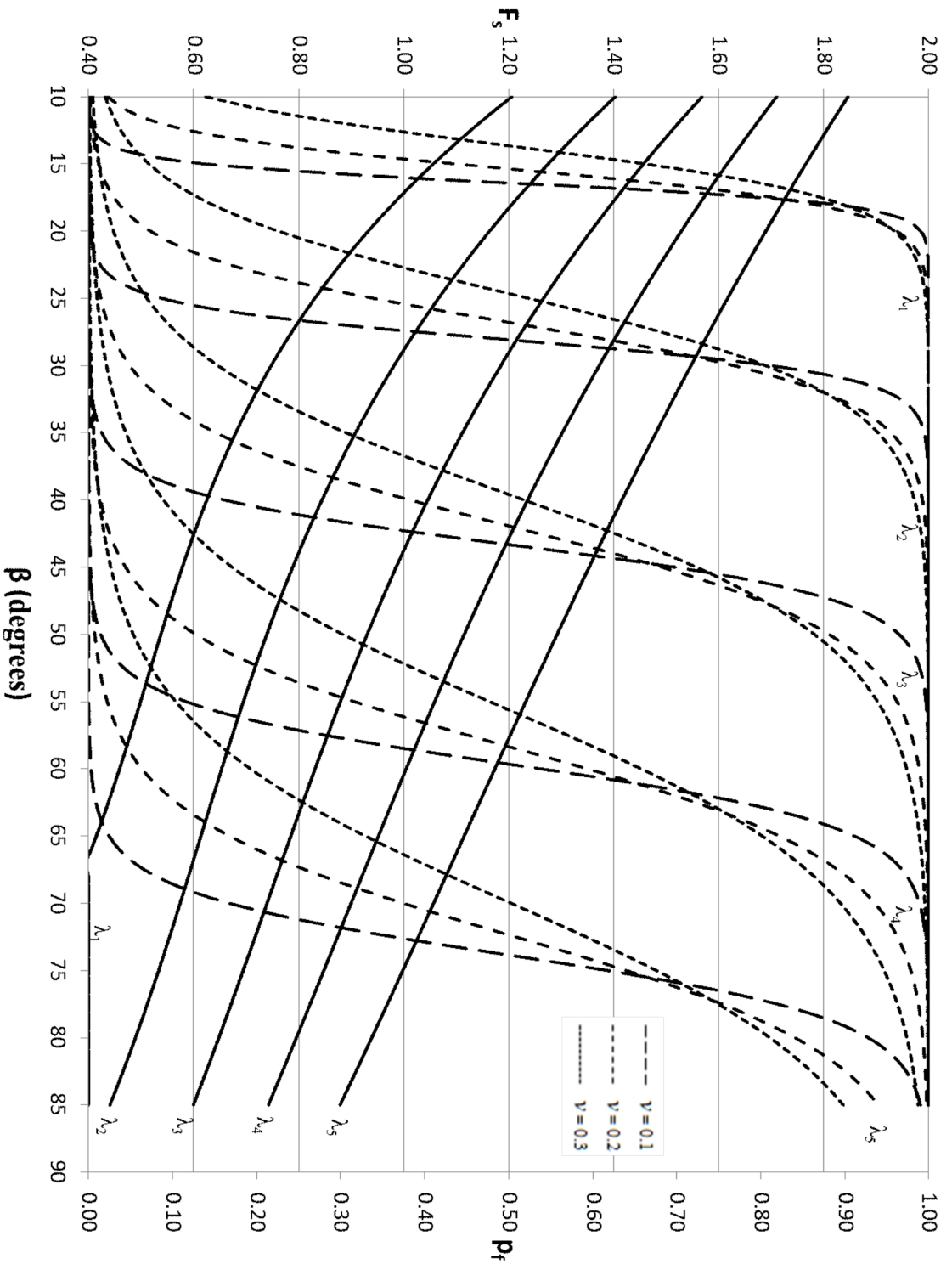

Figure C.19 Probabilistic pseudo-static slope stability design chart for $\mu_\phi = 20°$, $k = 0.2g$, $\theta = 0.7H$. Solid lines plot F_s. $\lambda_i = i/10$

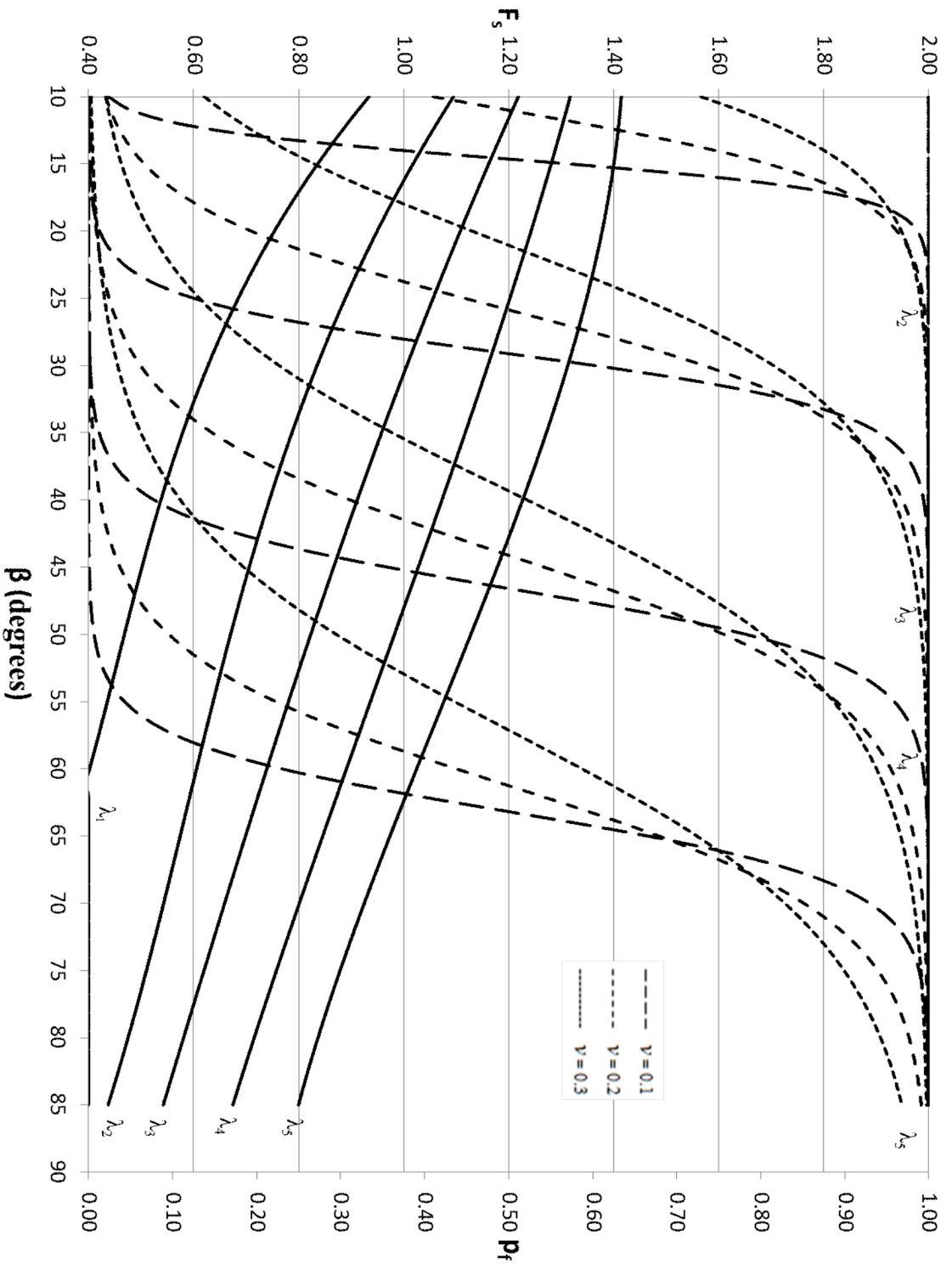

Figure C.20 Probabilistic pseudo-static slope stability design chart for $\mu_\phi = 20°$, $k = 0.3g$, $\theta = 0.7H$. Solid lines plot F_s. $\lambda_i = i/10$

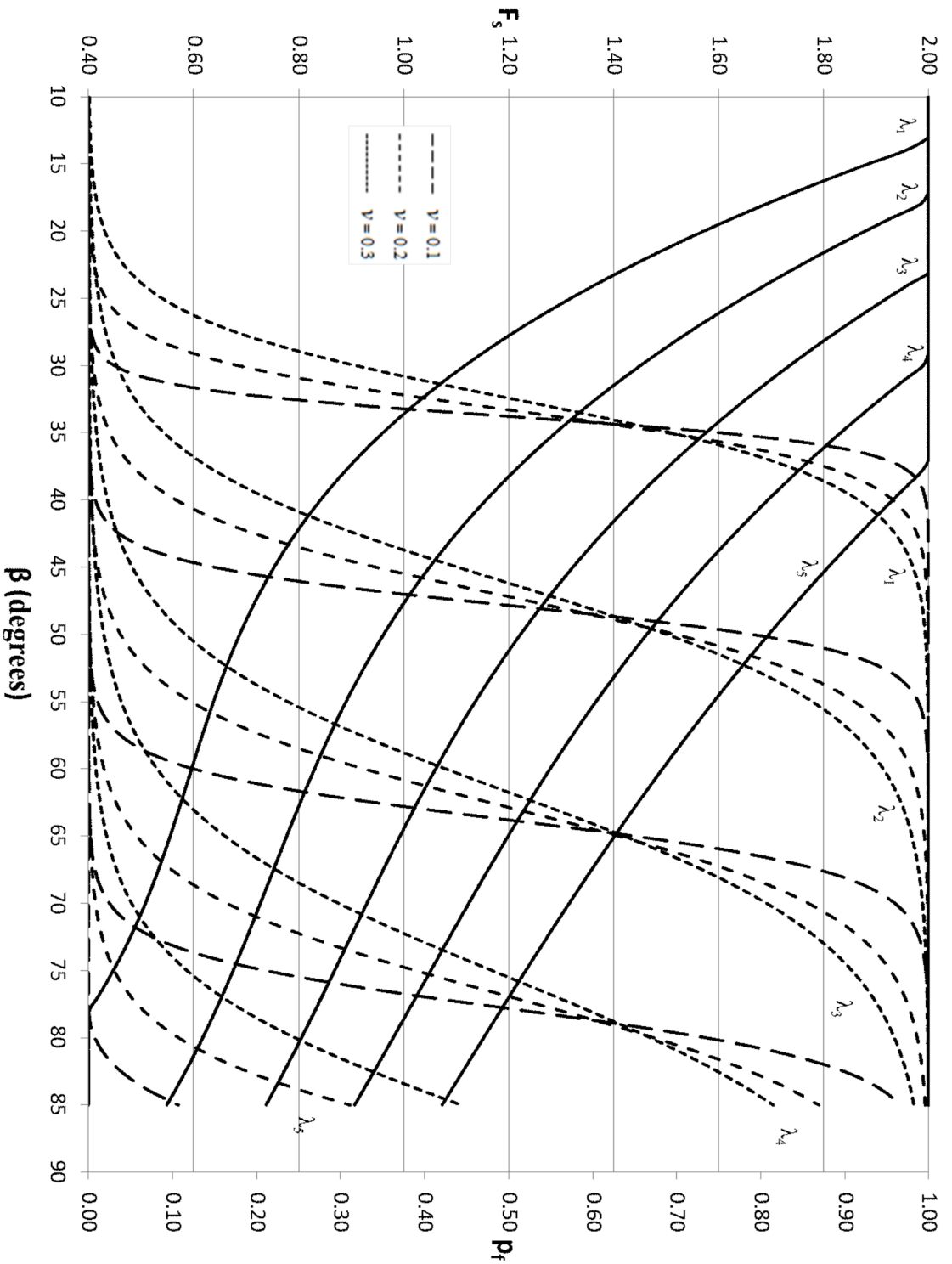

Figure C.21 Probabilistic pseudo-static slope stability design chart for $\mu_\phi = 20°$, $k = 0, \theta = H$. Solid lines plot F_s. $\lambda_i = i/10$

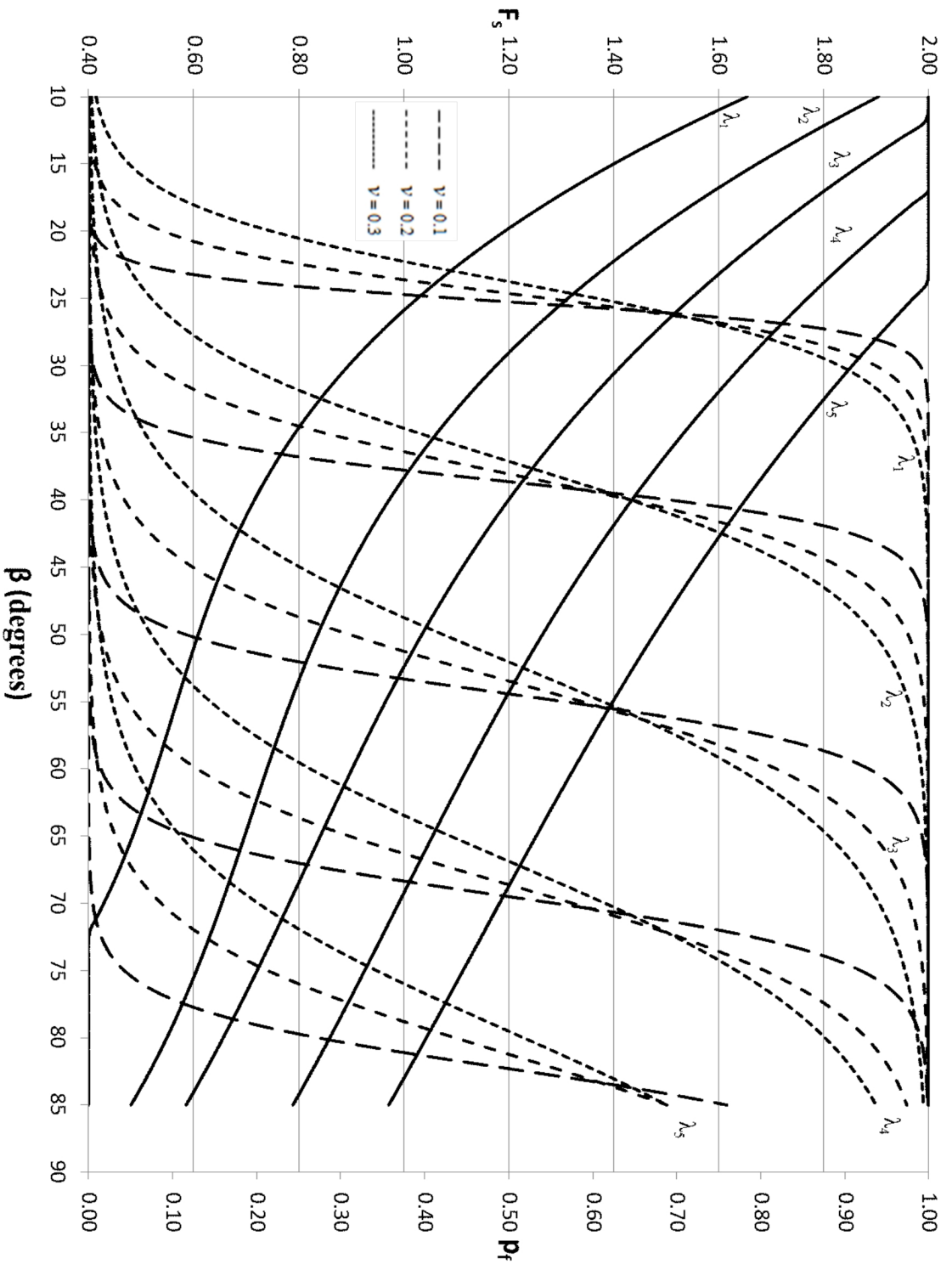

Figure C.22 Probabilistic pseudo-static slope stability design chart for $\mu_\phi = 20°$, $k = 0.1g$, $\theta = H$. Solid lines plot F_s. $\lambda_i = i/10$

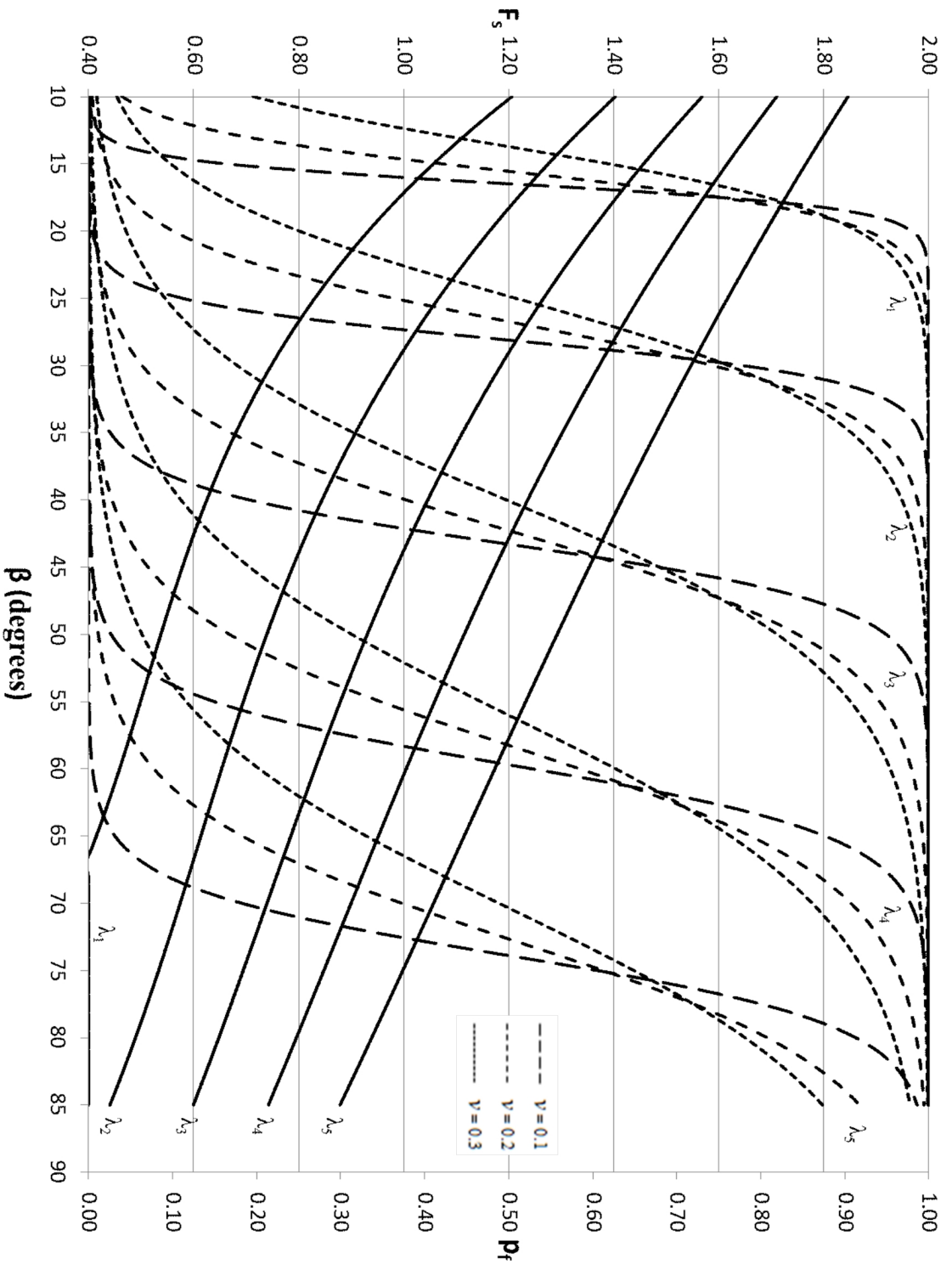

Figure C.23 Probabilistic pseudo-static slope stability design chart for $\mu_\phi = 20°$, $k = 0.2g$, $\theta = H$. Solid lines plot F_s. $\lambda_i = i/10$

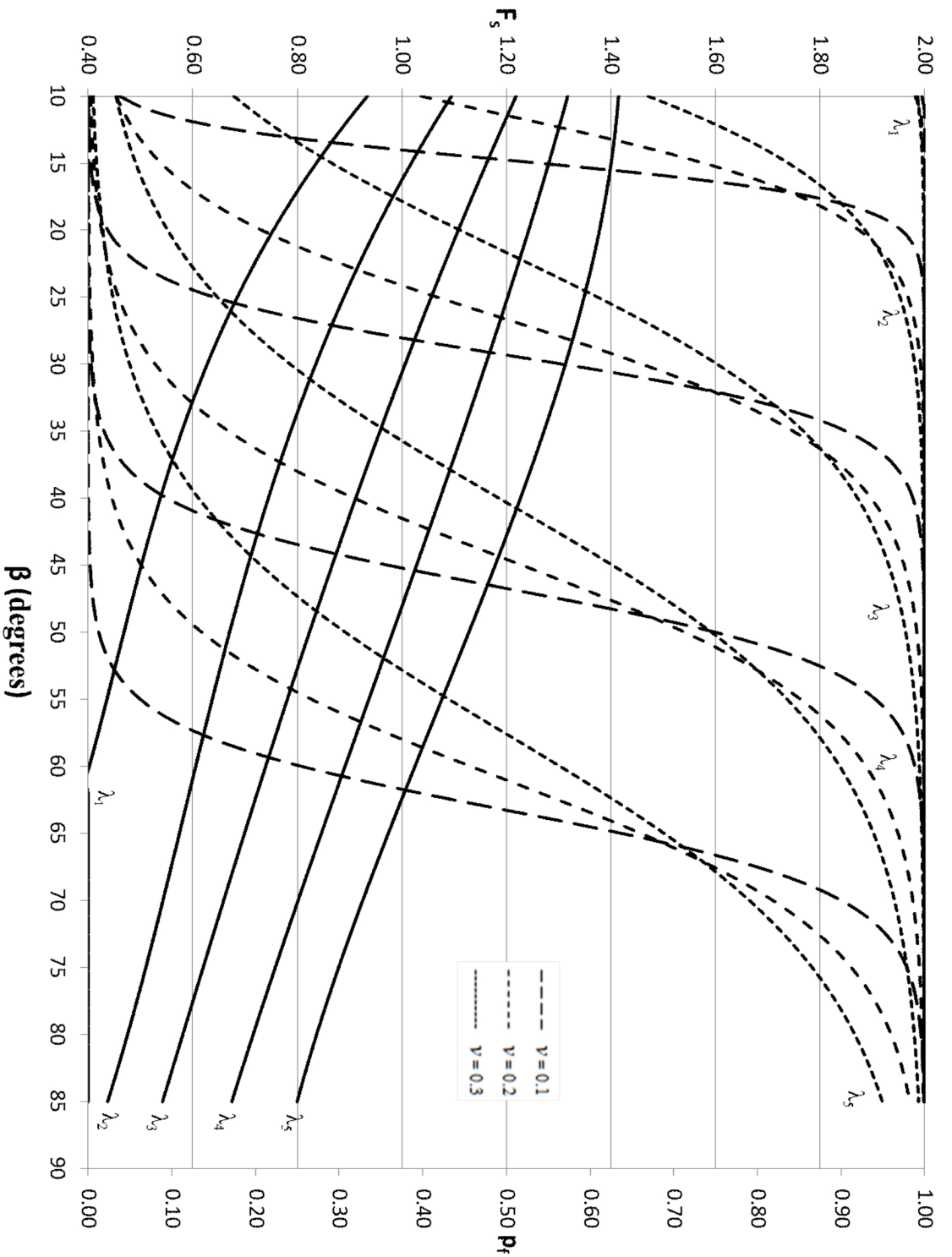

Figure C.24 Probabilistic pseudo-static slope stability design chart for $\mu_\phi = 20°$, $k = 0.3g$, $\theta = H$. Solid lines plot F_s. $\lambda_i = i/10$

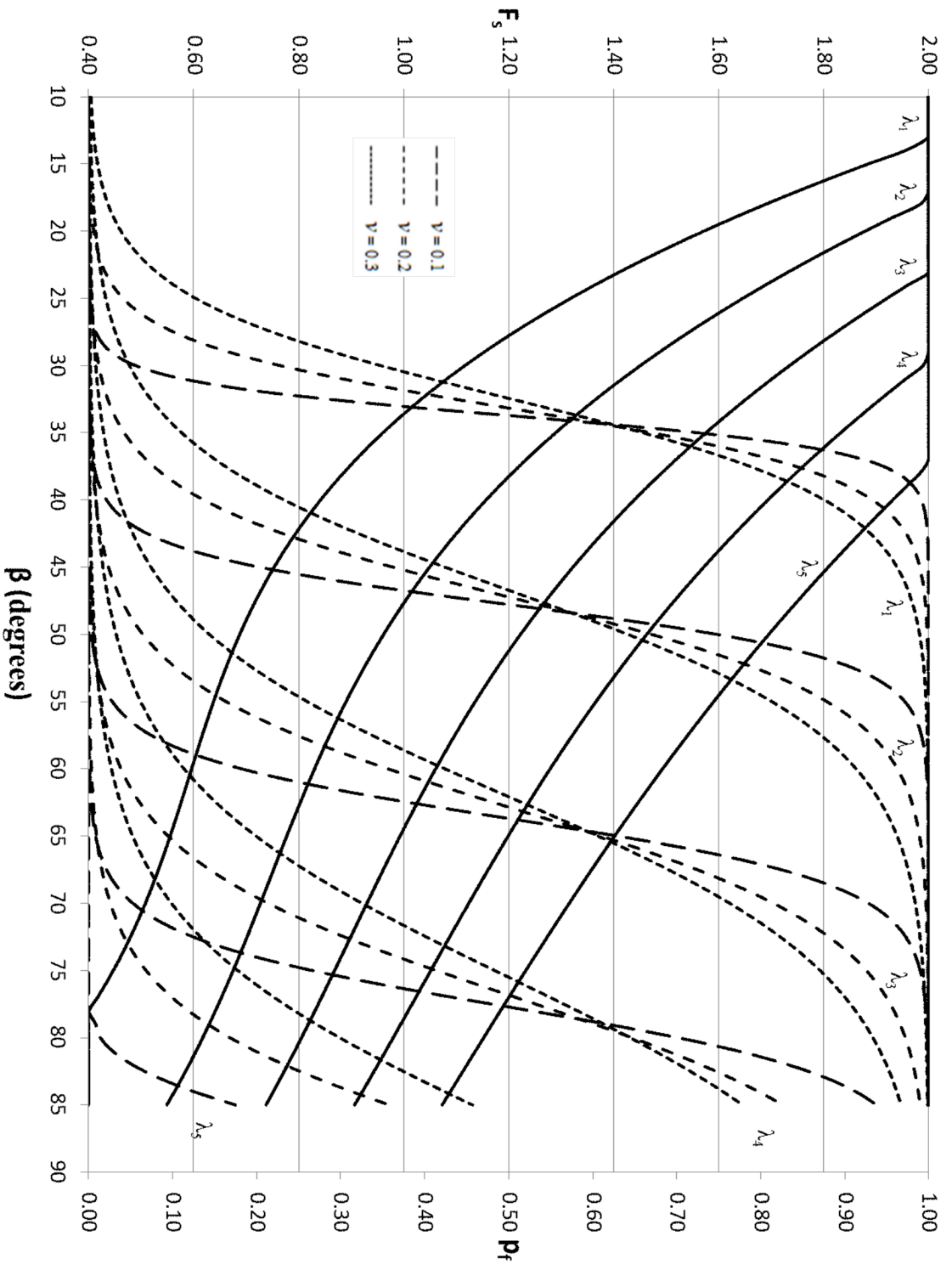

Figure C.25 Probabilistic pseudo-static slope stability design chart for $\mu_\phi = 20°$, $k = 0$, $\theta = 2H$. Solid lines plot F_s. $\lambda_i = i/10$

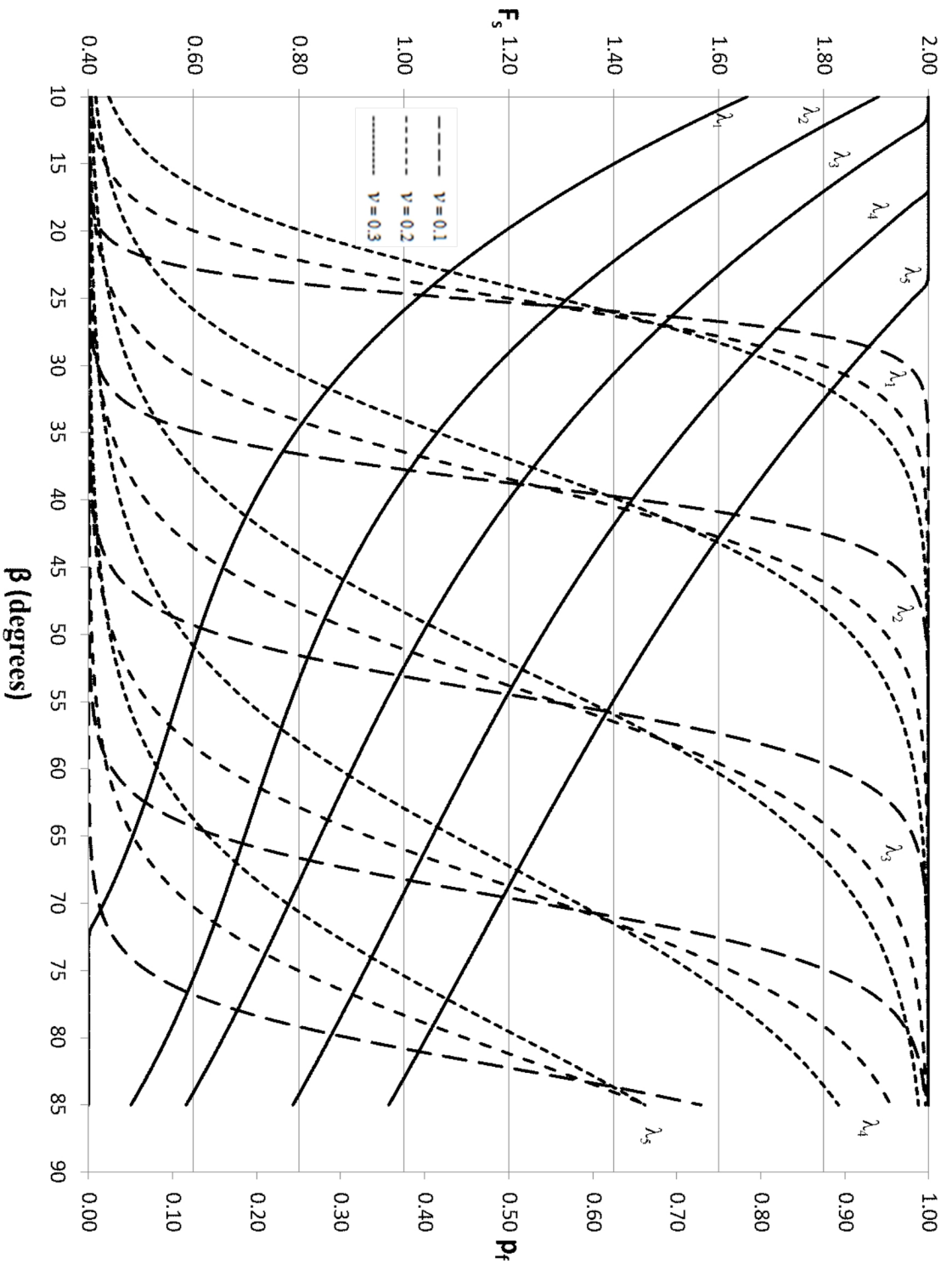

Figure C.26 Probabilistic pseudo-static slope stability design chart for $\mu_\phi = 20°$, $k = 0.1g$, $\theta = 2H$. Solid lines plot F_s. $\lambda_i = i/10$

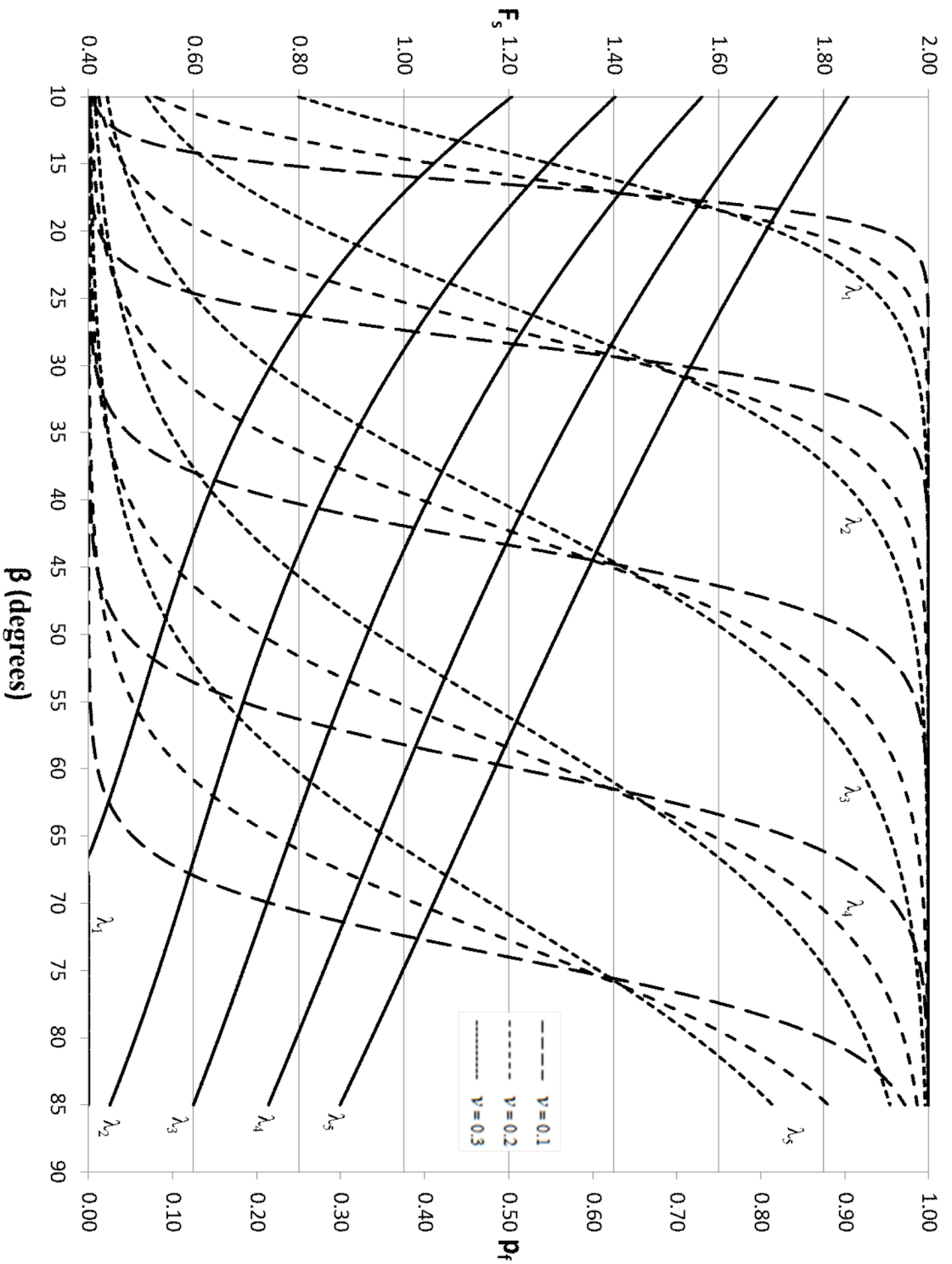

Figure C.27 Probabilistic pseudo-static slope stability design chart for $\mu_\phi = 20°$, $k = 0.2g$, $\theta = 2H$. Solid lines plot F_s. $\lambda_i = i/10$

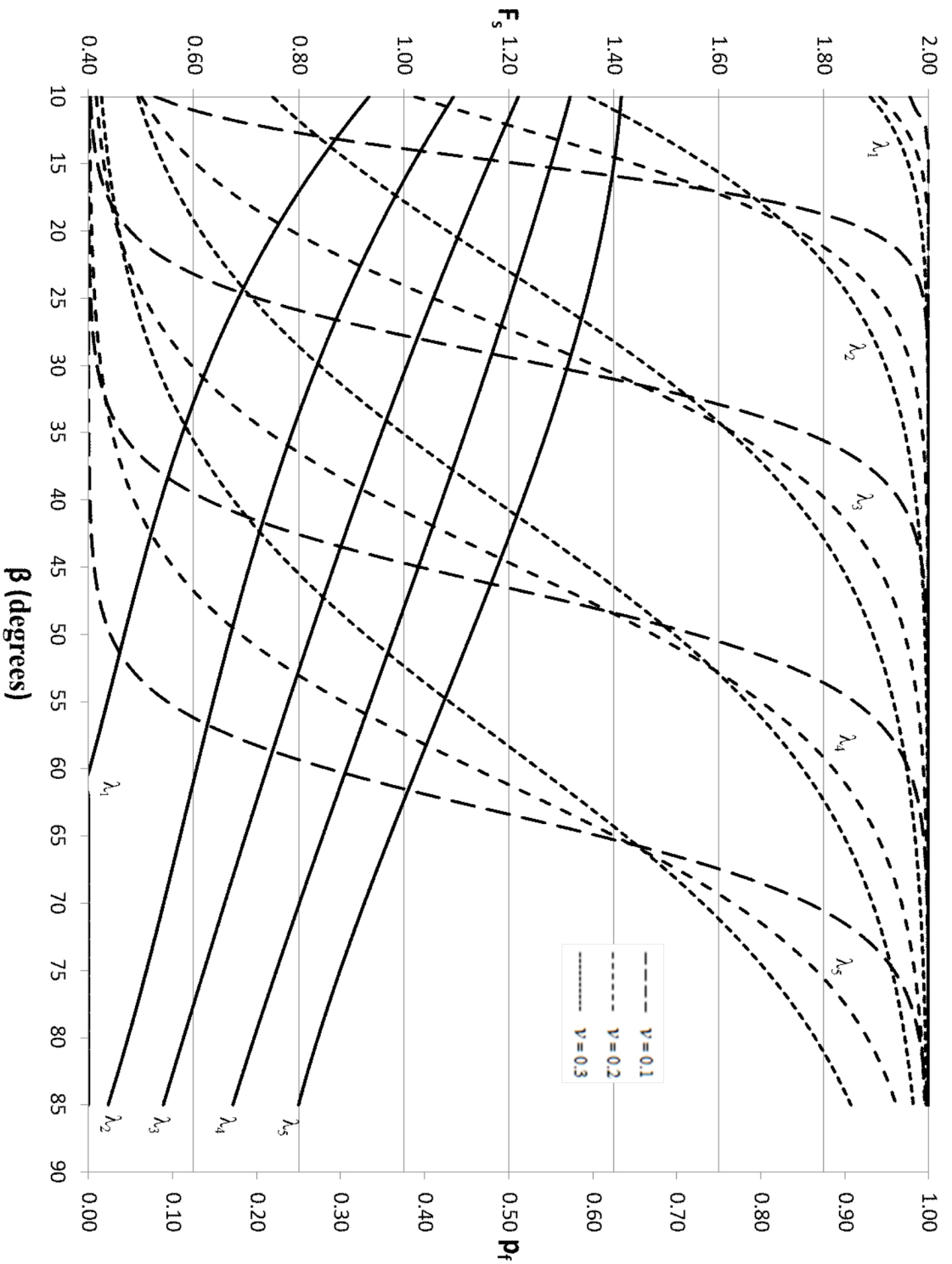

Figure C.28 Probabilistic pseudo-static slope stability design chart for $\mu_\phi = 20°$, $k = 0.3g$, $\theta = 2H$. Solid lines plot F_s. $\lambda_i = i/10$

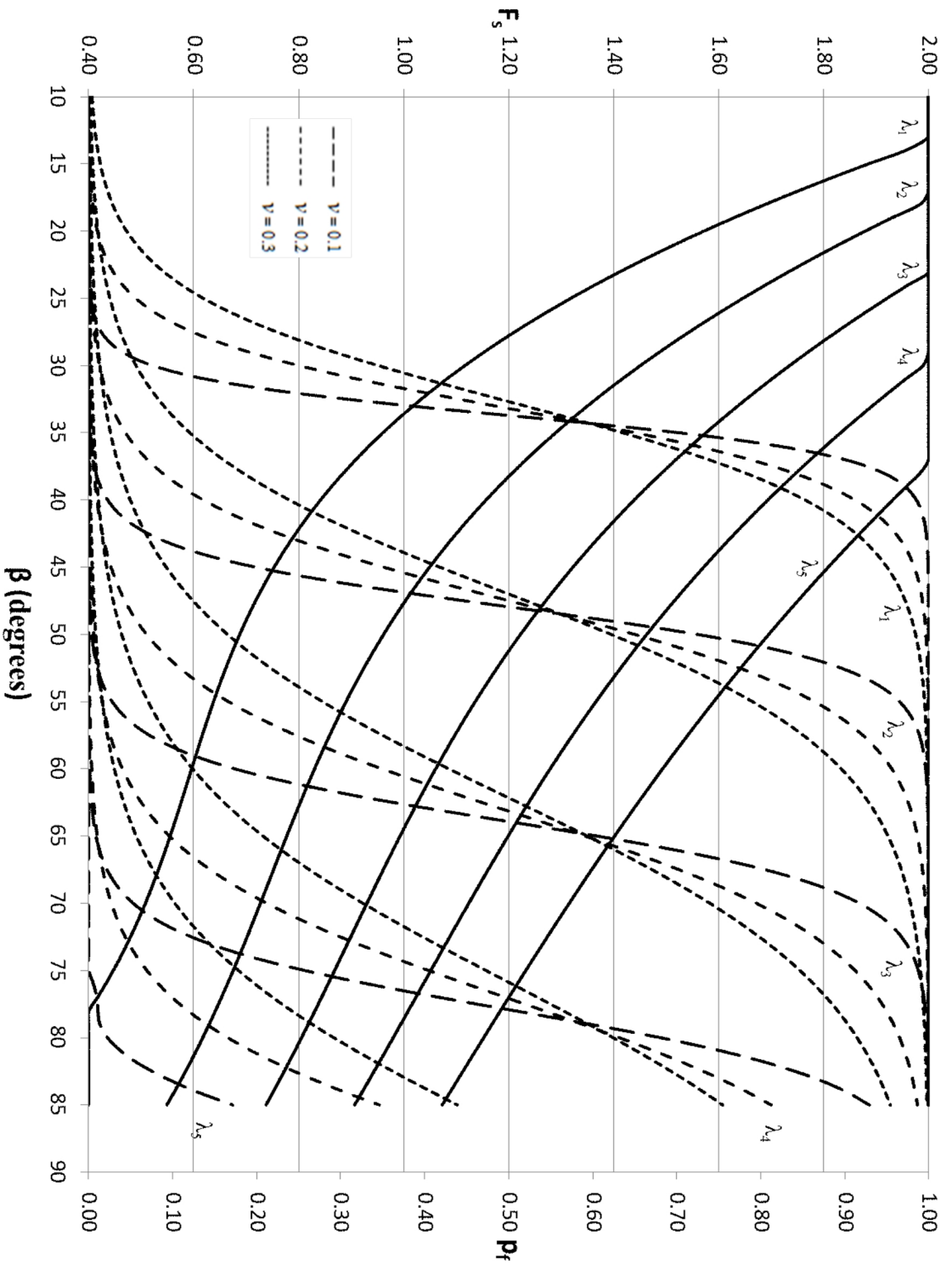

Figure C.29 Probabilistic pseudo-static slope stability design chart for $\mu_\phi = 20°$, $k = 0$, $\theta = 3H$. Solid lines plot F_s. $\lambda_i = i/10$

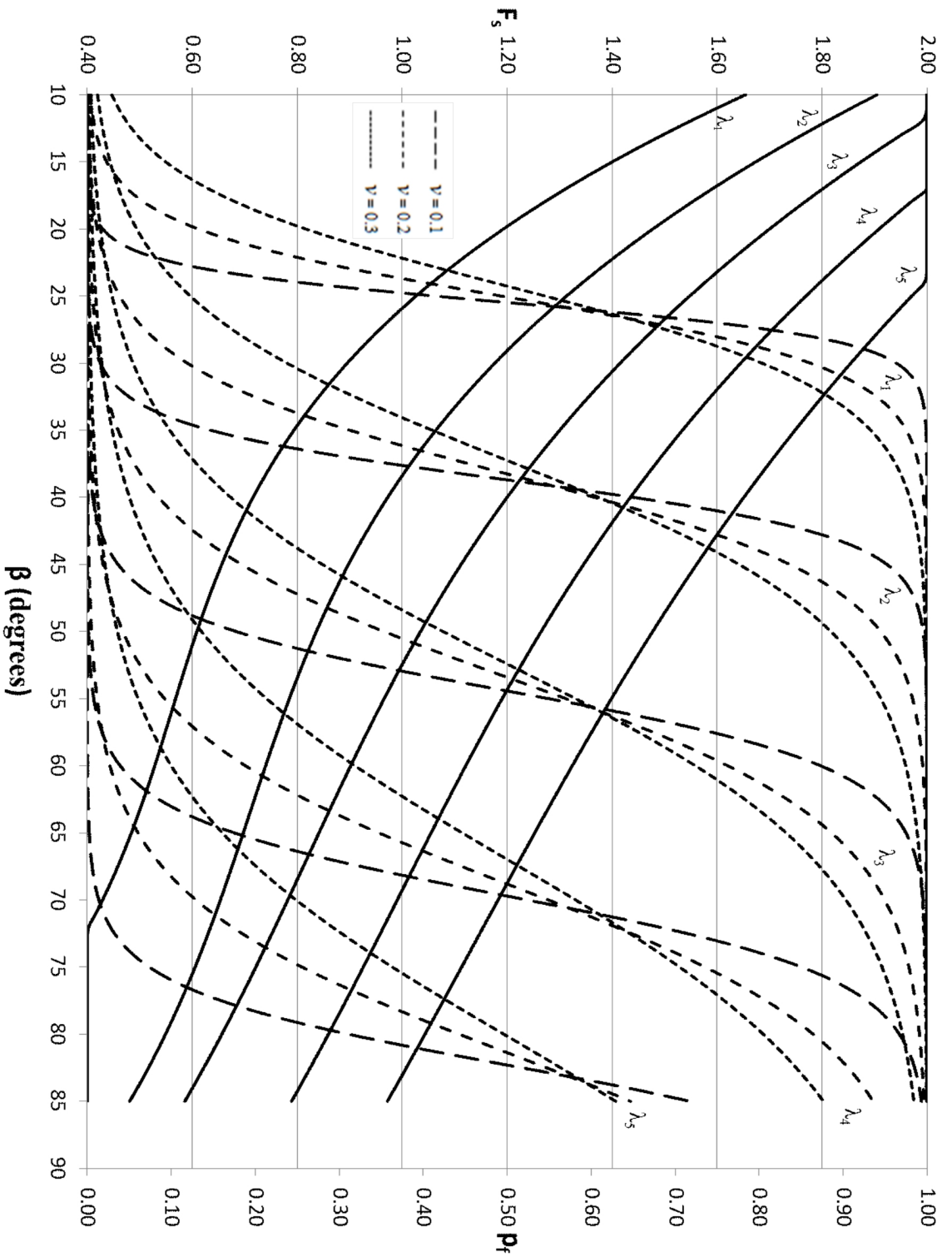

Figure C.30 Probabilistic pseudo-static slope stability design chart for $\mu_\phi = 20°$, $k = 0.1g$, $\theta = 3H$. Solid lines plot F_s. $\lambda_i = i/10$

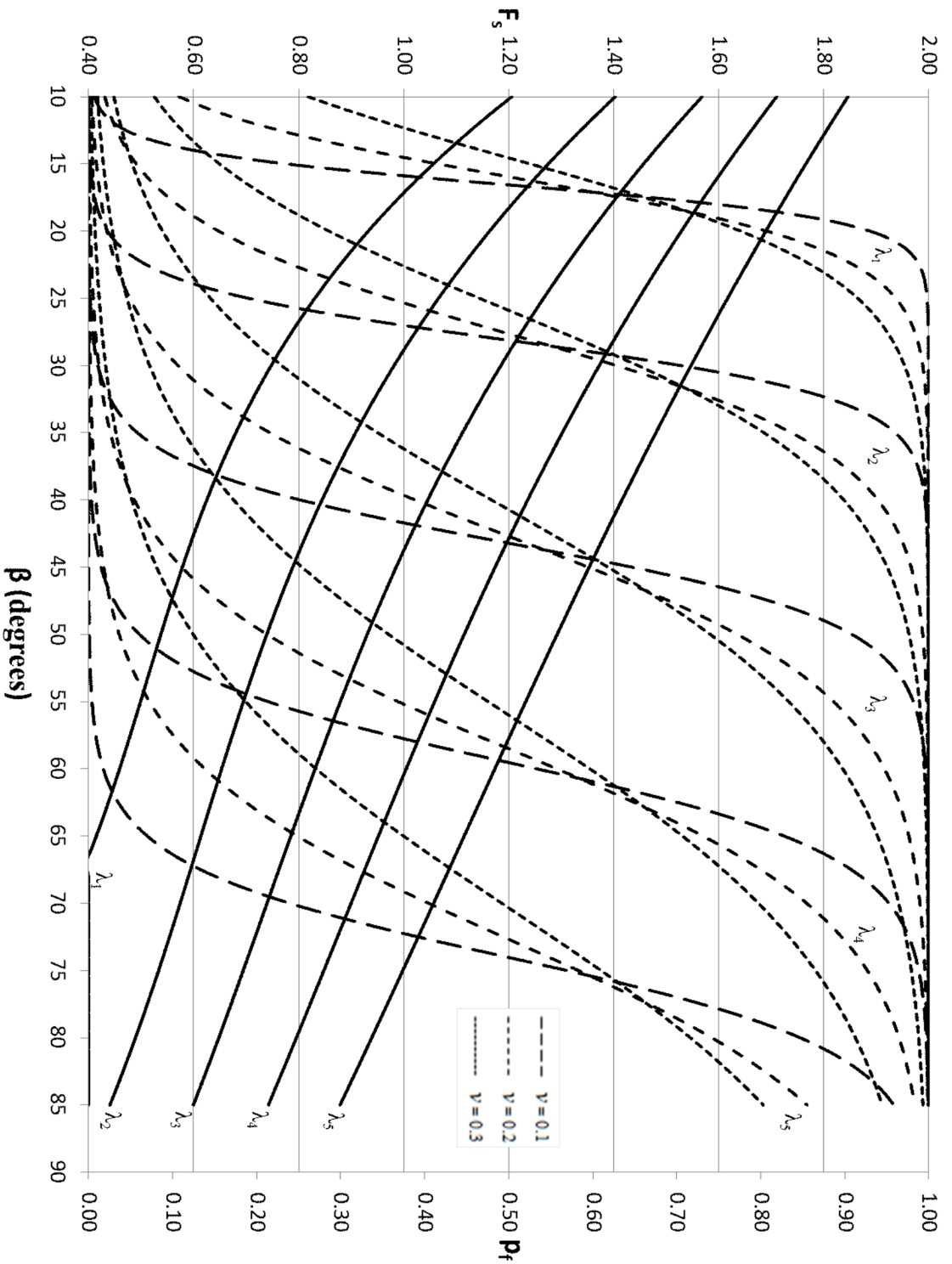

Figure C.31 Probabilistic pseudo-static slope stability design chart for $\mu_\phi = 20°$, $k = 0.2g$, $\theta = 3H$. Solid lines plot F_s. $\lambda_i = i/10$

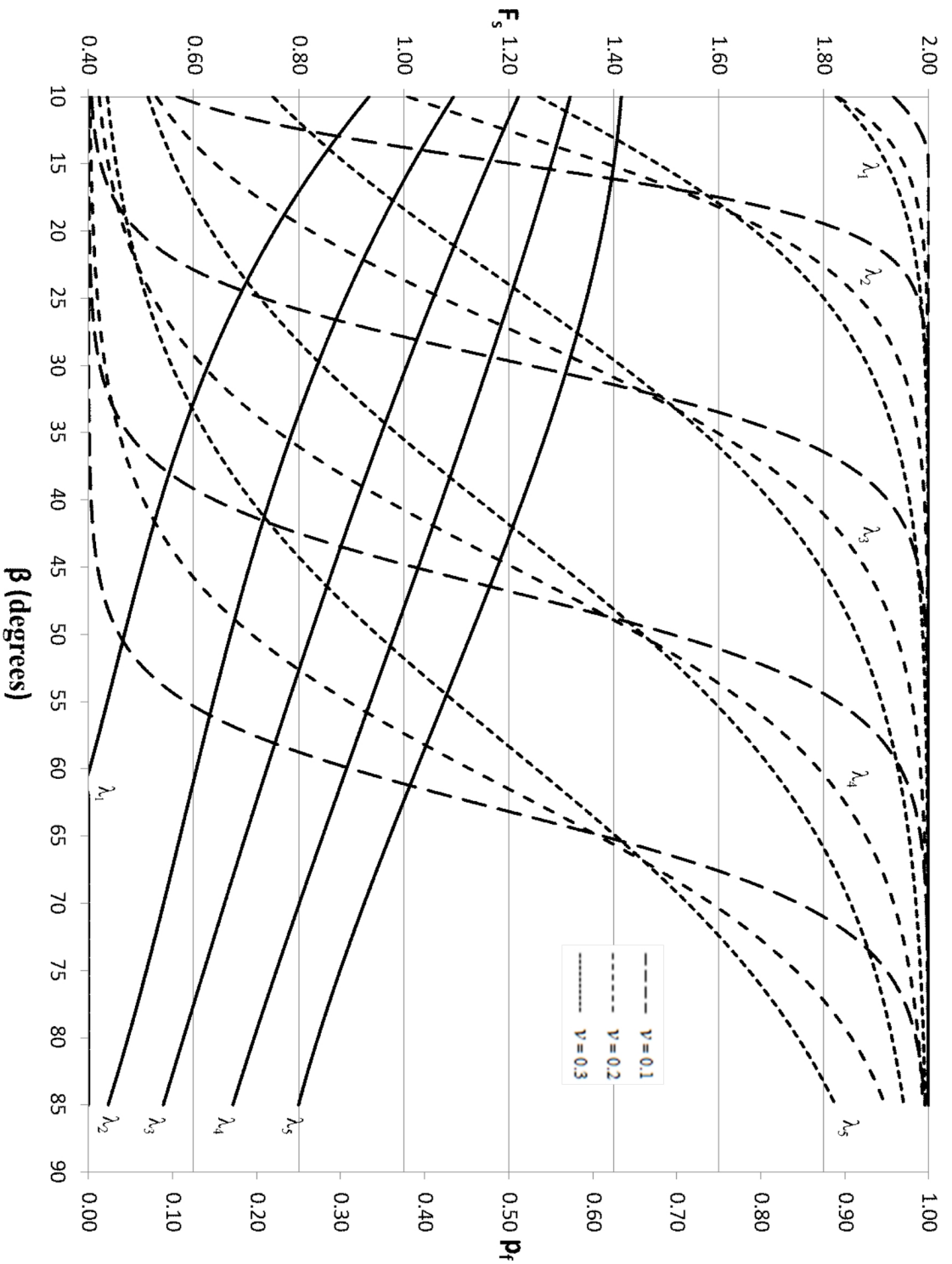

Figure C.32 Probabilistic pseudo-static slope stability design chart for $\mu_\phi = 20°$, $k = 0.3g$, $\theta = 3H$. Solid lines plot F_s. $\lambda_i = i/10$

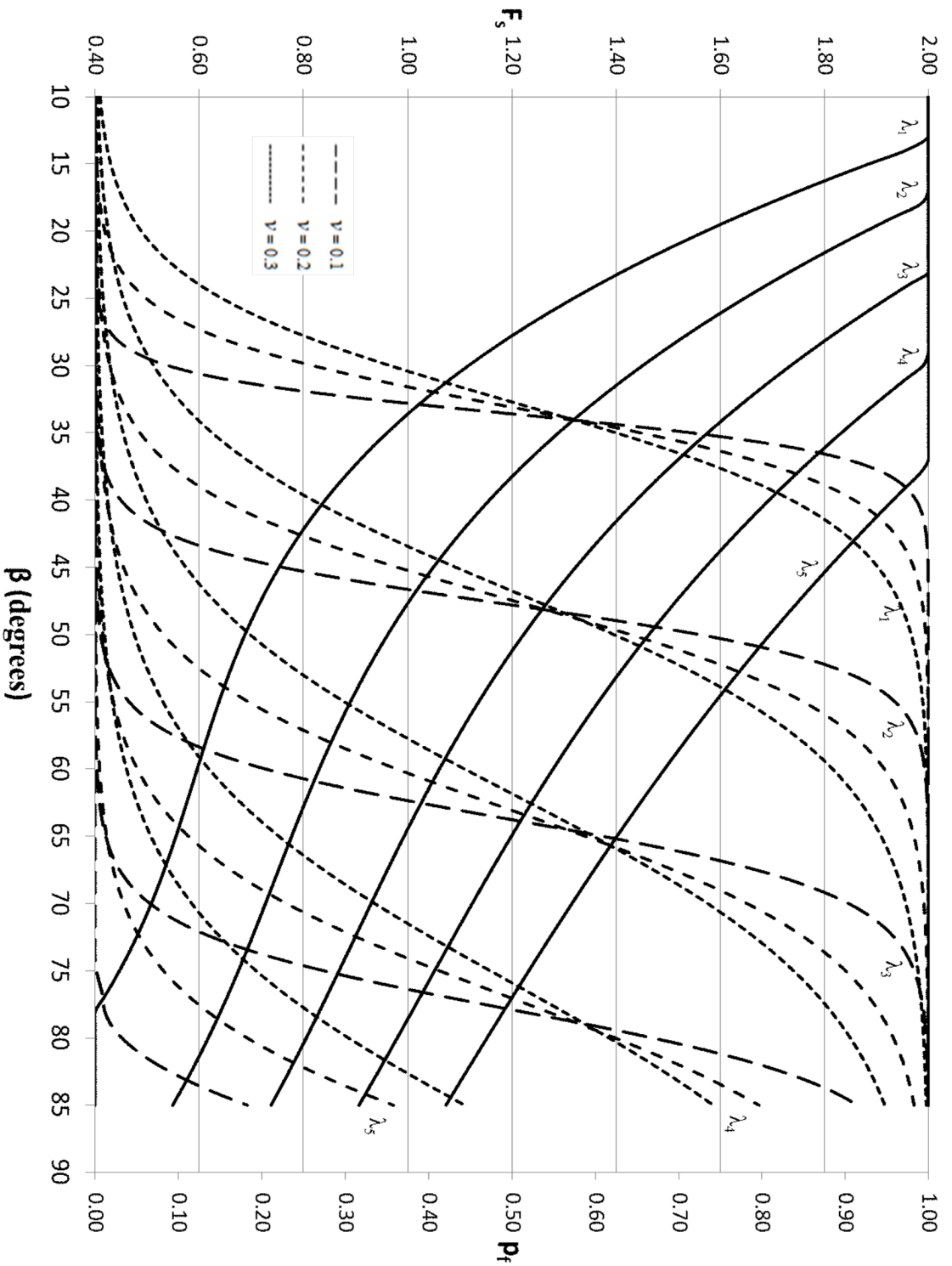

Figure C.33 Probabilistic pseudo-static slope stability design chart for $\mu_\phi = 20°$, $k = 0, \theta = 5H$. Solid lines plot F_s. $\lambda_i = i/10$

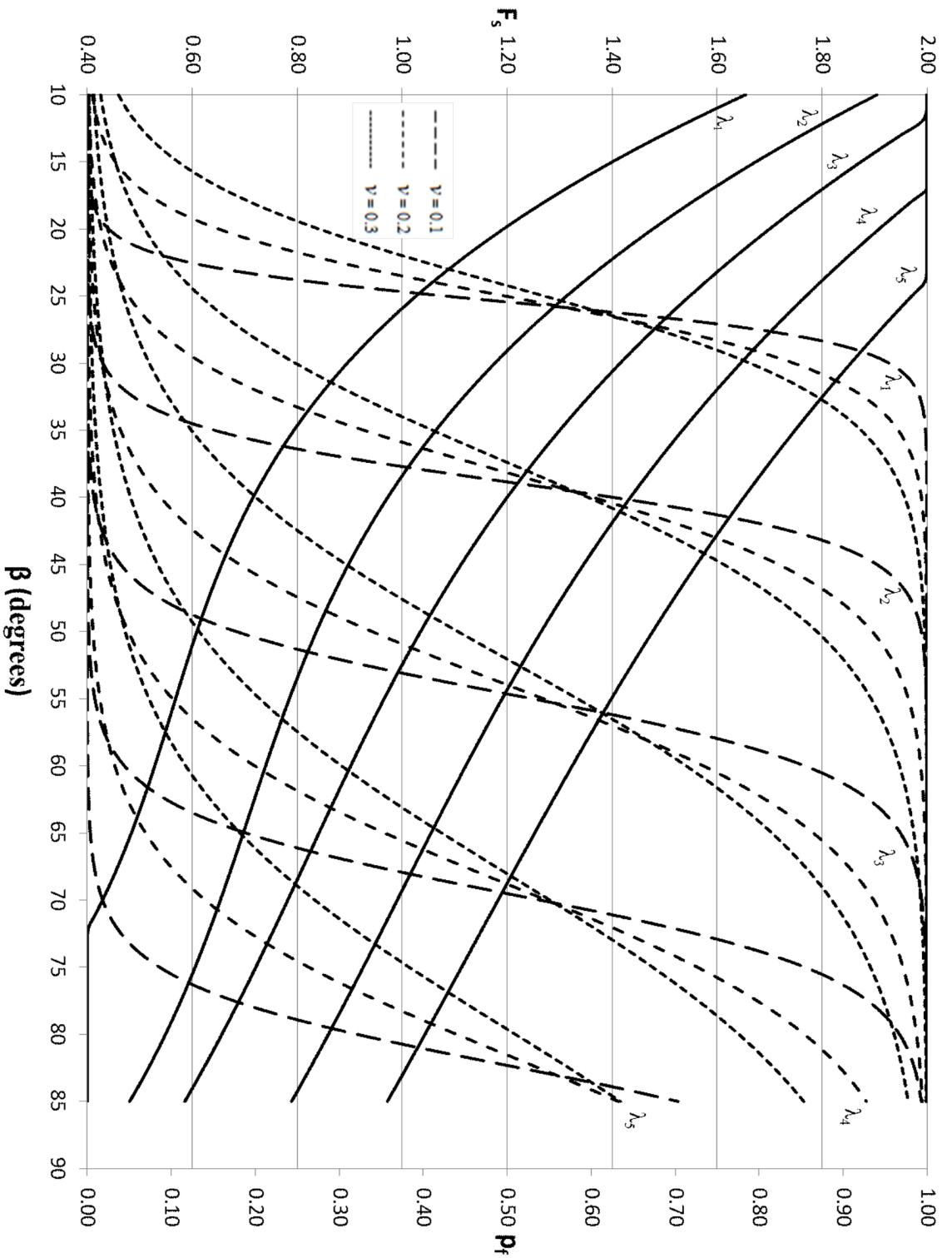

Figure C.34 Probabilistic pseudo-static slope stability design chart for $\mu_\phi = 20°$, $k = 0.1g$, $\theta = 5H$. Solid lines plot F_s. $\lambda_i = i/10$

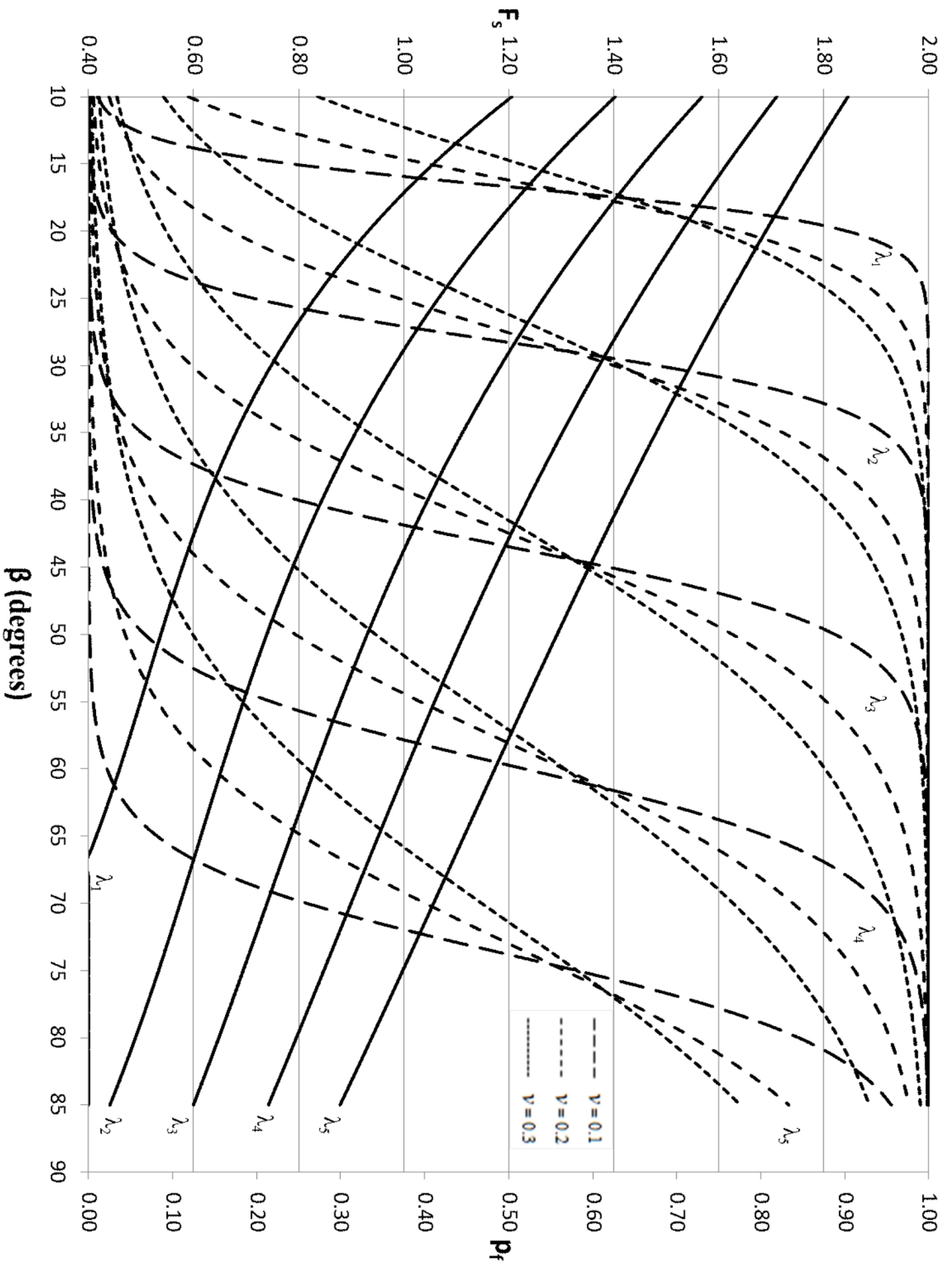

Figure C.35 Probabilistic pseudo-static slope stability design chart for $\mu_\phi = 20°$, $k = 0.2g$, $\theta = 5H$. Solid lines plot F_s. $\lambda_i = i/10$

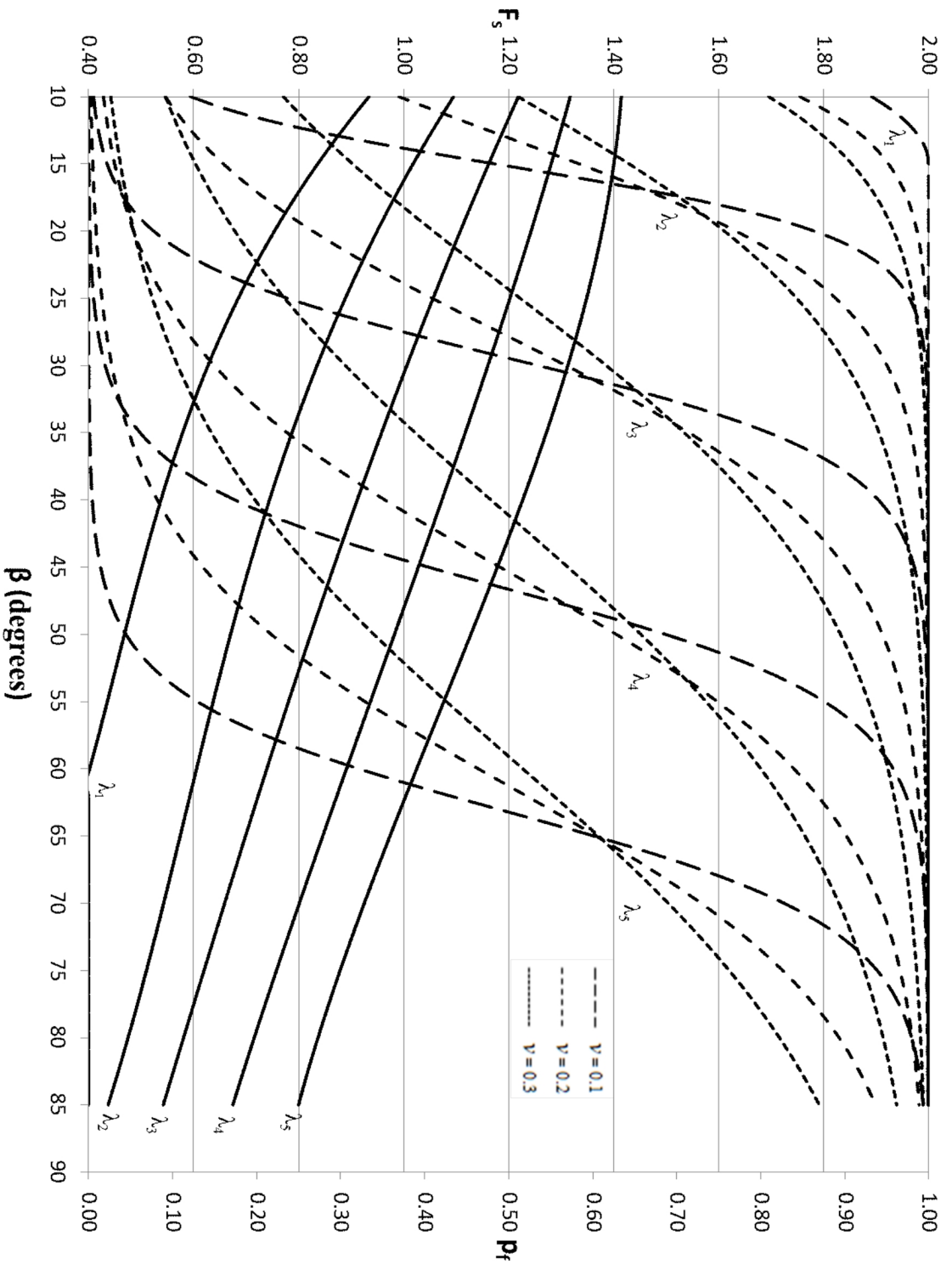

Figure C.36 Probabilistic pseudo-static slope stability design chart for $\mu_\phi = 20°$, $k = 0.3g$, $\theta = 5H$. Solid lines plot F_s. $\lambda_i = i/10$

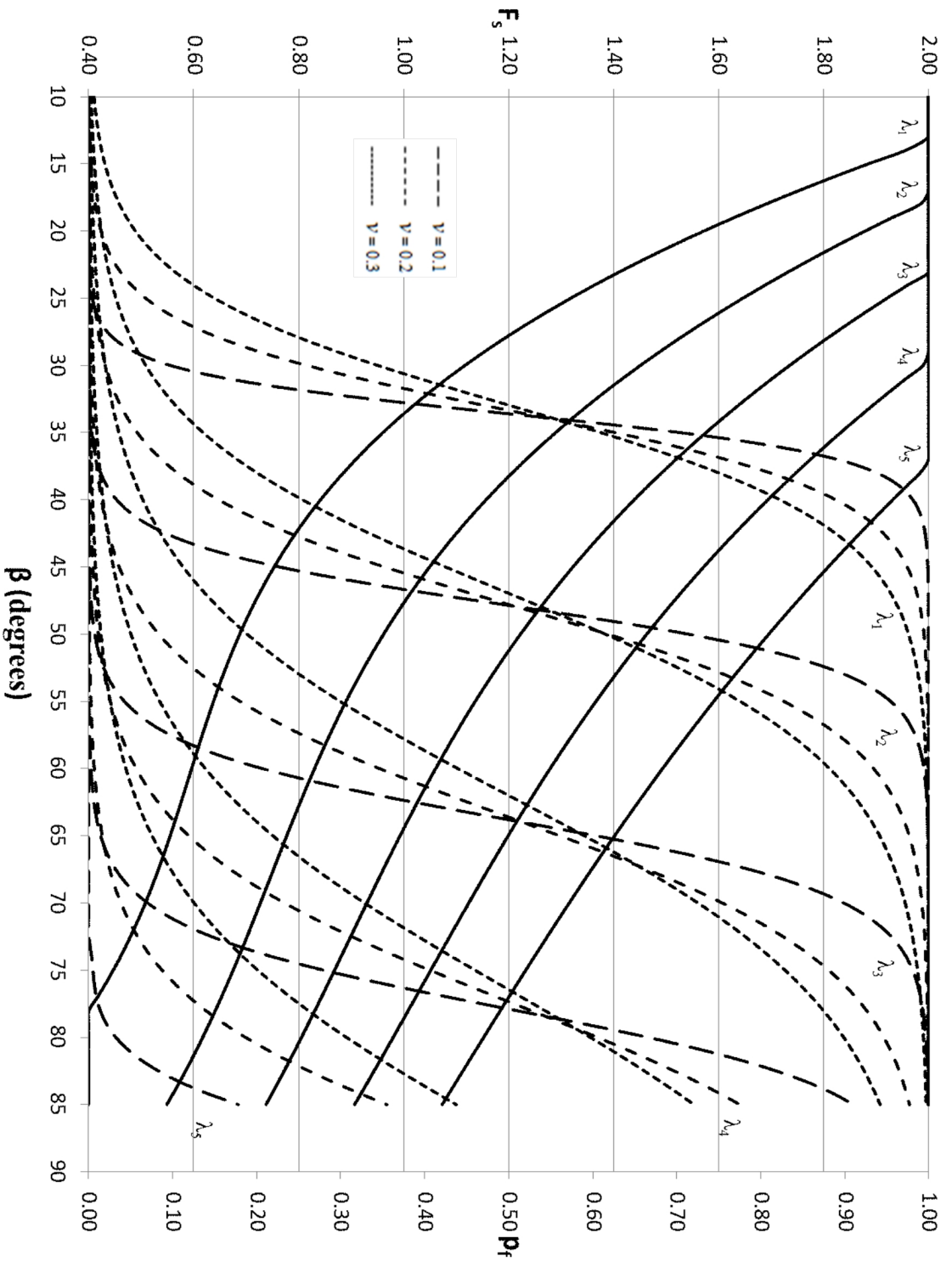

Figure C.37 Probabilistic pseudo-static slope stability design chart for $\mu_\phi = 20°$, $k = 0, \theta = 7H$. Solid lines plot F_s. $\lambda_i = i/10$

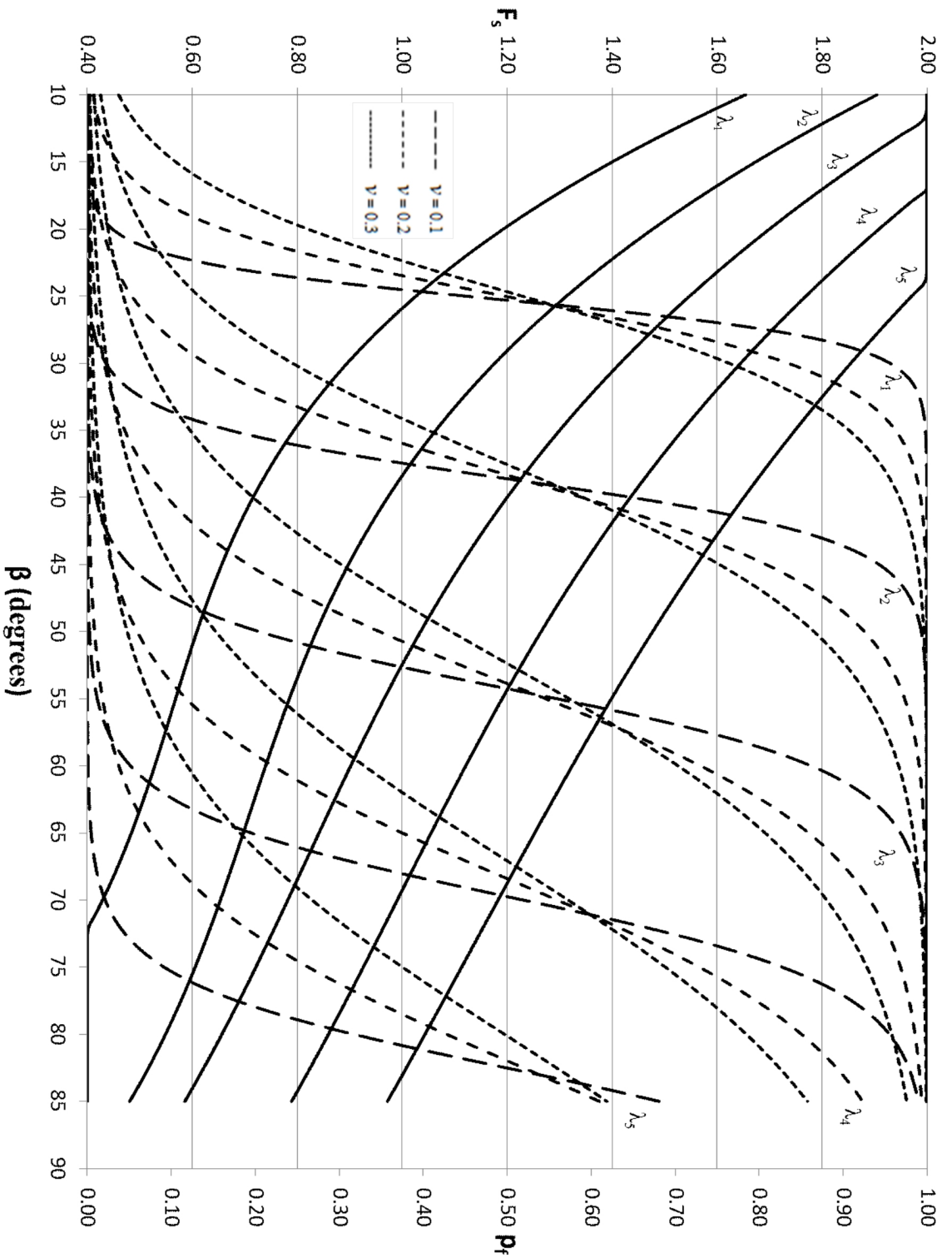

Figure C.38 Probabilistic pseudo-static slope stability design chart for $\mu_\phi = 20°$, $k = 0.1g$, $\theta = 7H$. Solid lines plot F_s. $\lambda_i = i/10$

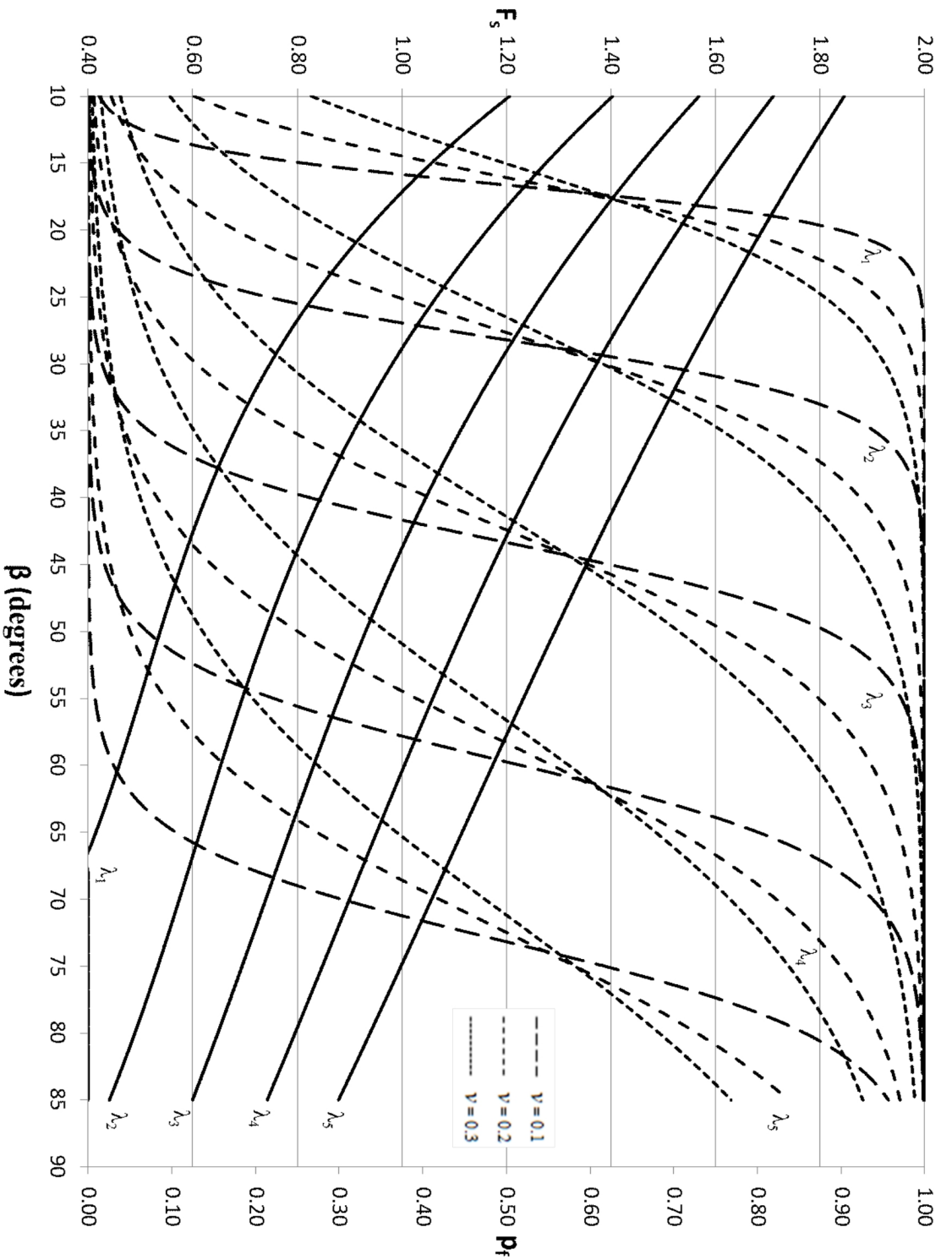

Figure C.39 Probabilistic pseudo-static slope stability design chart for $\mu_\phi = 20°$, $k = 0.2g$, $\theta = 7H$. Solid lines plot F_s. $\lambda_i = i/10$

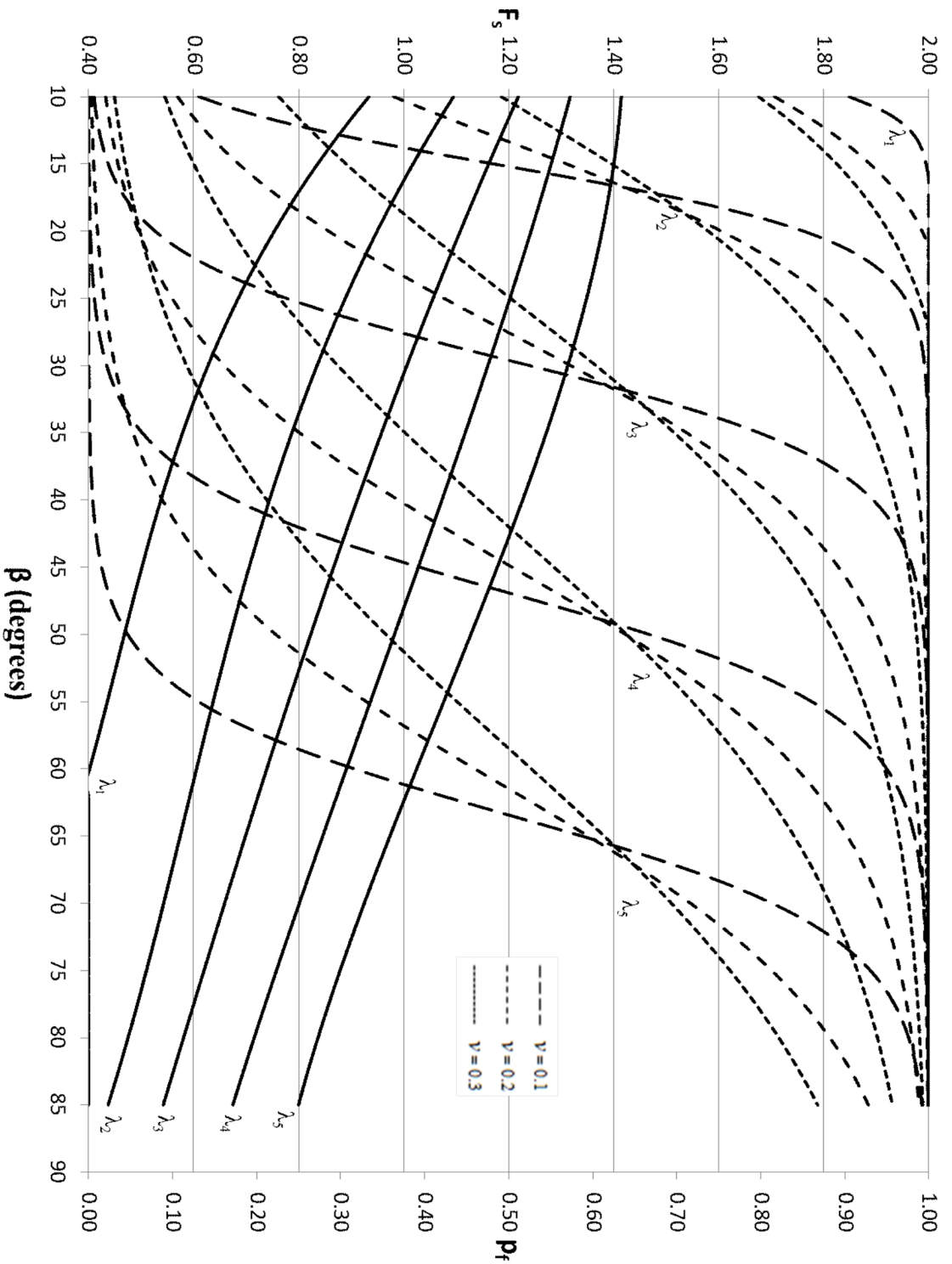

Figure C.40 Probabilistic pseudo-static slope stability design chart for $\mu_\phi = 20°$, $k = 0.3g$, $\theta = 7H$. Solid lines plot F_s. $\lambda_i = i/10$

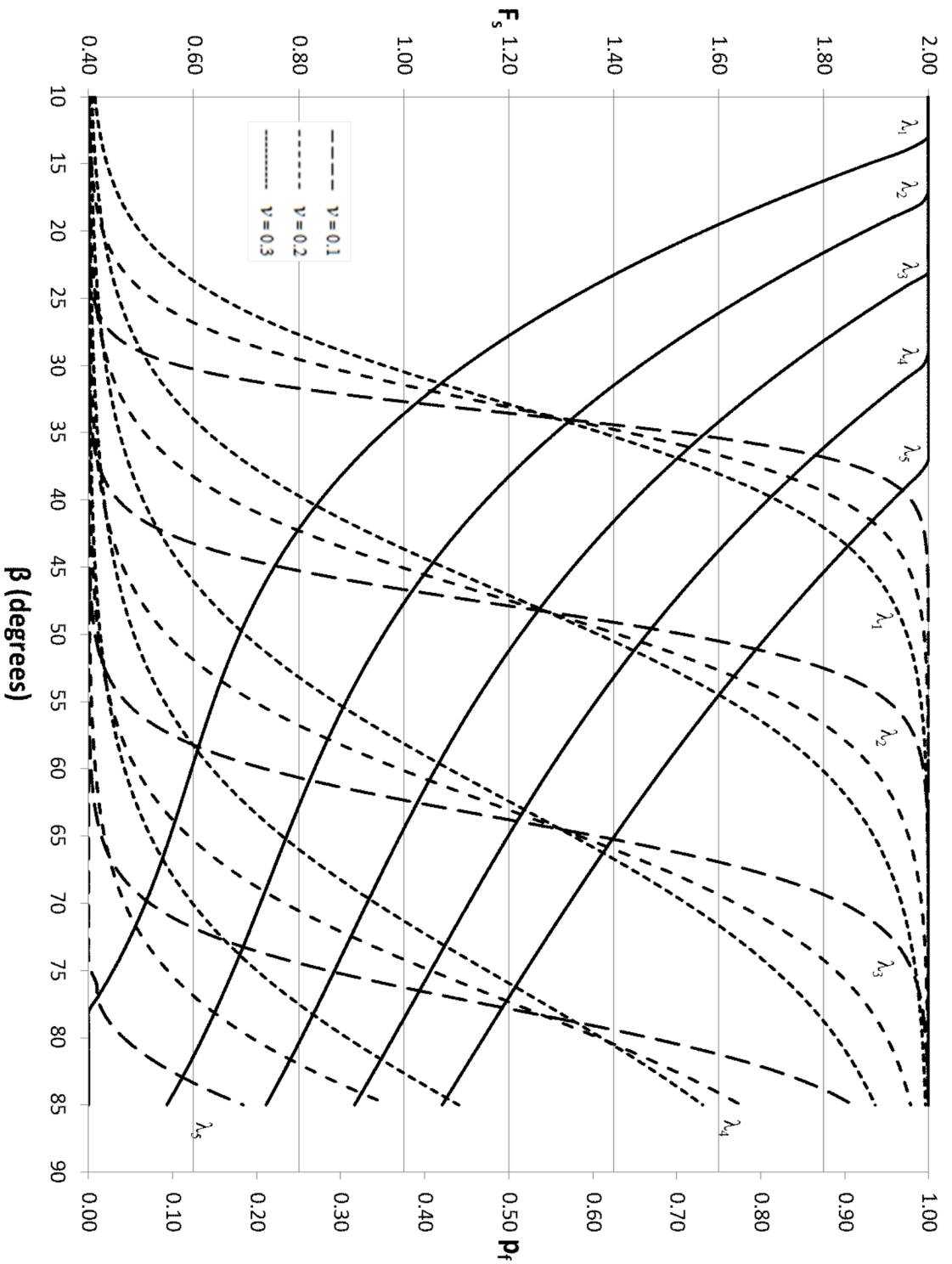

Figure C.41 Probabilistic pseudo-static slope stability design chart for $\mu_\phi = 20°$, $k = 0$, $\theta = 10H$. Solid lines plot F_s. $\lambda_i = i/10$

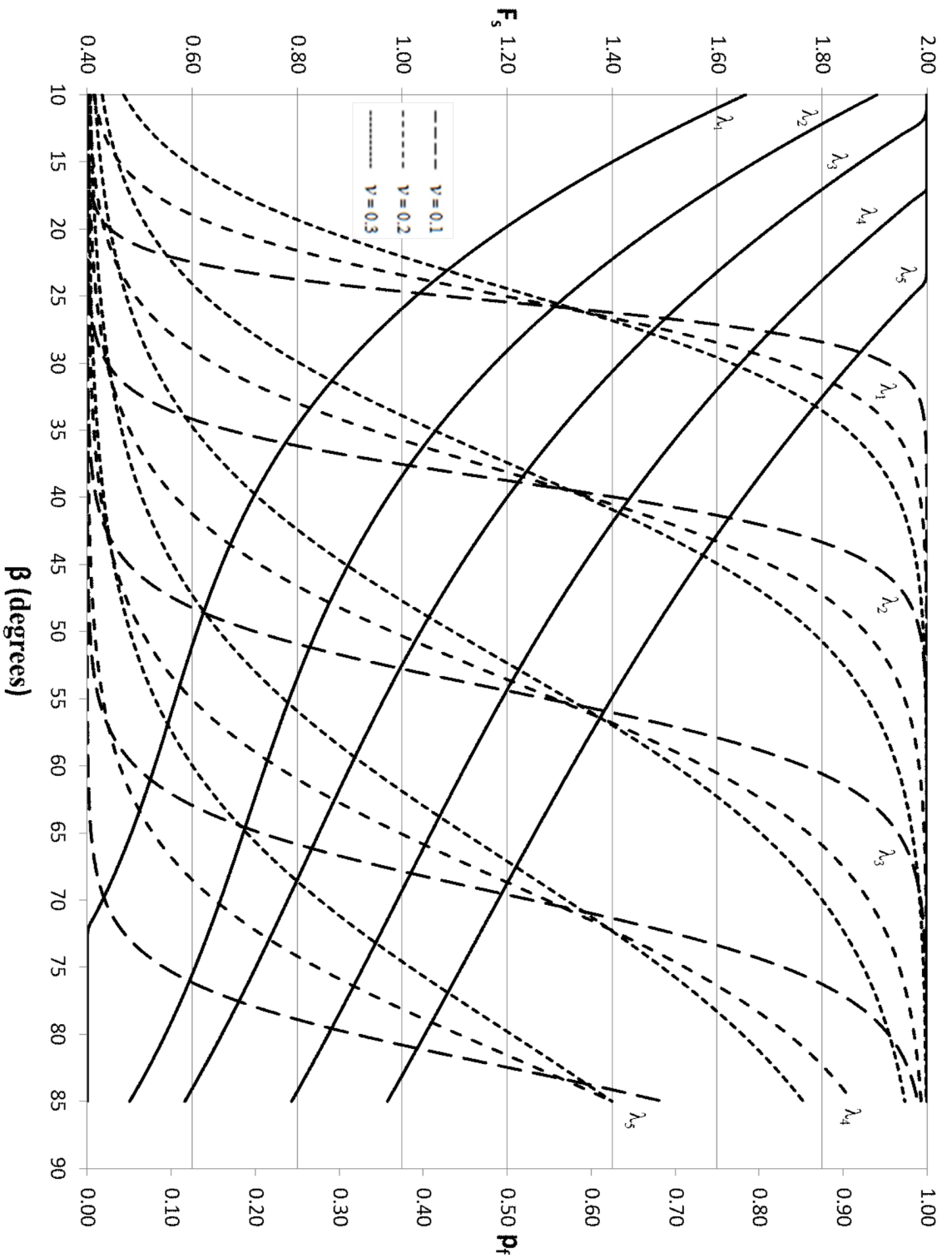

Figure C.42 Probabilistic pseudo-static slope stability design chart for $\mu_\phi = 20°$, $k = 0.1g$, $\theta = 10H$. Solid lines plot F_s. $\lambda_i = i/10$

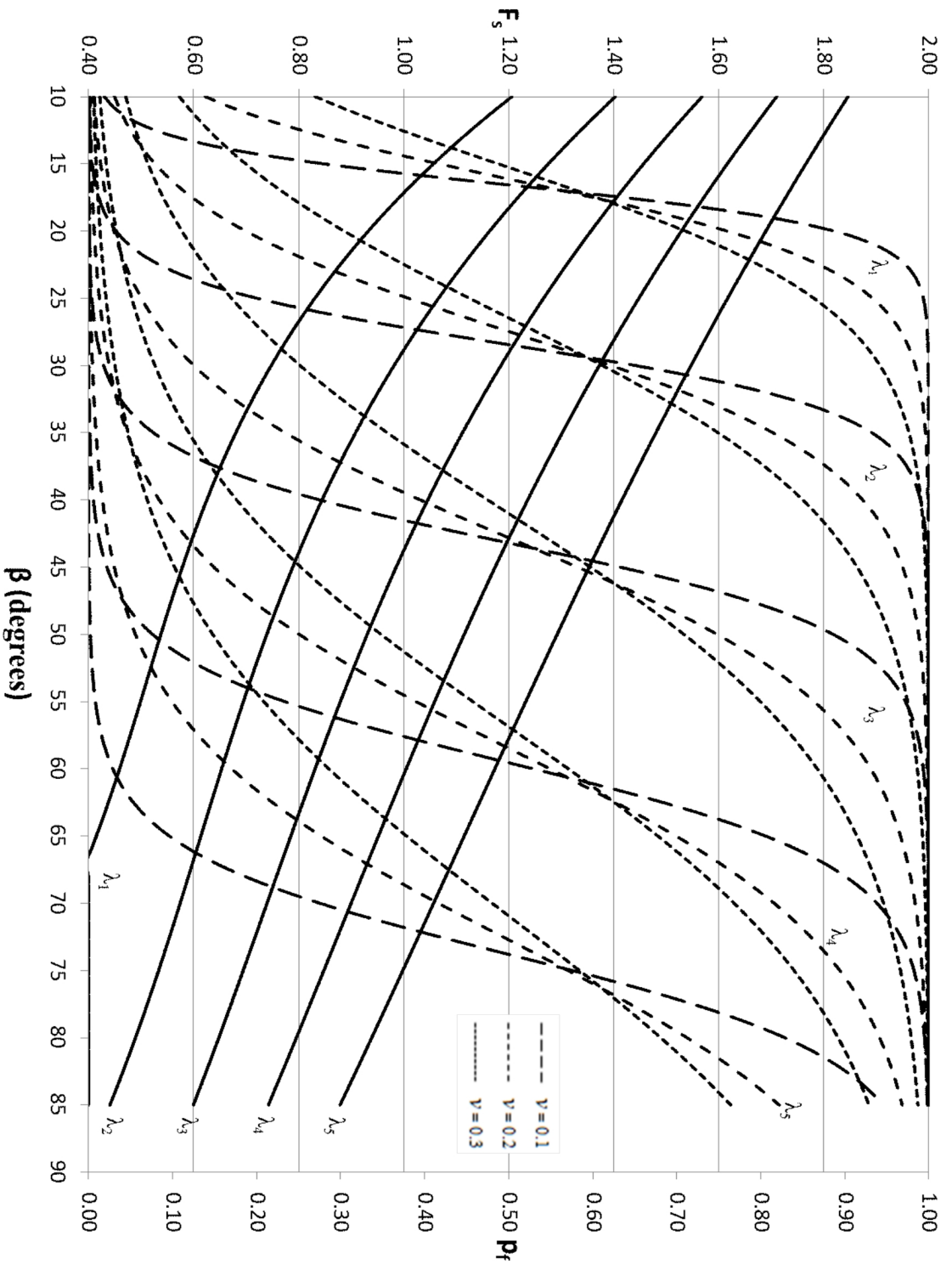

Figure C.43 Probabilistic pseudo-static slope stability design chart for $\mu_\phi = 20°$, $k = 0.2g$, $\theta = 10H$. Solid lines plot F_s. $\lambda_i = i/10$

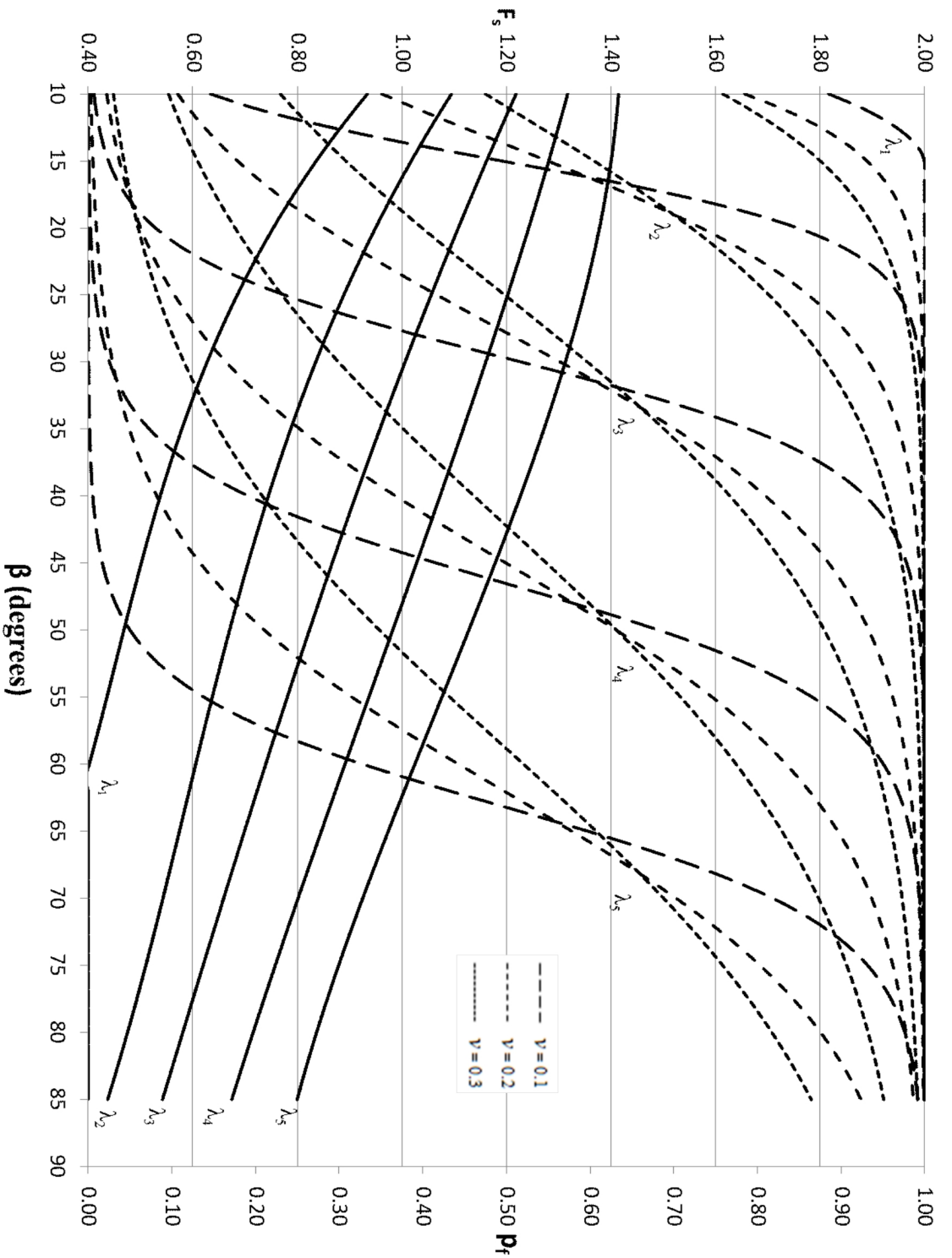

Figure C.44 Probabilistic pseudo-static slope stability design chart for $\mu_\phi = 20°$, $k = 0.3g$, $\theta = 10H$. Solid lines plot F_s. $\lambda_i = i/10$